DESI Observations of the Andromeda Galaxy: Revealing the Immigration History of our Nearest Neighbor

Arjun Dey,[1] Joan R. Najita,[1] Sergey E. Koposov,[2,3] J. Josephy-Zack,[4] Gabriel Maxemin,[4] Eric F. Bell,[5]
C. Poppett,[6,7,8] E. Patel,[9] L. Beraldo e Silva,[5] A. Raichoor,[10] D. Schlegel,[6] D. Lang,[11,12] A. Meisner,[1]
Adam D. Myers,[13] J. Aguilar,[6] S. Ahlen,[14] C. Allende Prieto,[15] D. Brooks,[16] A.P. Cooper,[17,18,19]
K. S. Dawson,[20] A. de la Macorra,[21] P. Doel,[16] A. Font-Ribera,[22] Juan García-Bellido,[23]
S. Gontcho A Gontcho,[24] J. Guy,[6] K. Honscheid,[25,26] R. Kehoe,[27] T. Kisner,[6] A. Kremin,[6] M. Landriau,[6]
L. Le Guillou,[28] Michael E. Levi,[6] T. S. Li,[29] Paul Martini,[25,30] R. Miquel,[31,22] J. Moustakas,[32] Jundan Nie,[33]
N. Palanque-Delabrouille,[34,6] F. Prada,[35] E. F. Schlafly,[36] Ray M. Sharples,[37] Gregory Tarlé,[38]
Yuan-Sen Ting (丁源森),[39,40] L. Tyas,[6] M. Valluri,[5] Risa H. Wechsler,[41,42,43] and H. Zou[33]

[1]NSF's NOIRLab, 950 N. Cherry Avenue, Tucson, AZ 85719, USA
[2]Institute for Astronomy, University of Edinburgh, Royal Observatory, Blackford Hill, Edinburgh EH9 3HJ, UK
[3]Institute of Astronomy, University of Cambridge, Madingley road, Cambridge, CB3 0HA, UK
[4]Harvard College, Cambridge, MA 02138, USA
[5]Department of Astronomy, University of Michigan, Ann Arbor, MI 48109, USA
[6]Lawrence Berkeley National Laboratory, 1 Cyclotron Road, Berkeley, CA 94720, USA
[7]Space Sciences Laboratory, University of California, Berkeley, 7 Gauss Way, Berkeley, CA 94720, USA
[8]University of California, Berkeley, 110 Sproul Hall #5800 Berkeley, CA 94720, USA
[9]Astronomy Dept., University of California at Berkeley, Berkeley, CA 94720, USA
[10]Lawrence Berkeley National Laboratory, Berkeley, CA 94720, USA
[11]Perimeter Institute for Theoretical Physics, 31 Caroline Street N, Waterloo, ON N25 2YL, Canada
[12]Department of Physics and Astronomy, University of Waterloo, Waterloo, ON N2L 3G1, Canada
[13]Department of Physics & Astronomy, University of Wyoming, 1000 E. University, Dept. 3905, Laramie, WY 82071, USA
[14]Physics Dept., Boston University, 590 Commonwealth Avenue, Boston, MA 02215, USA
[15]Instituto de Astrofísica de Canarias, C/ Vía Láctea, s/n, 38205 San Cristóbal de La Laguna, Santa Cruz de Tenerife, Spain
[16]Department of Physics & Astronomy, University College London, Gower Street, London, WC1E 6BT, UK
[17]Institute of Astronomy and Department of Physics, National Tsing Hua University, 101 Kuang-Fu Rd. Sec. 2, Hsinchu 30013, Taiwan
[18]Center for Informatics and Computation in Astronomy, NTHU, 101 Kuang-Fu Rd. Sec. 2, Hsinchu 30013, Taiwan
[19]Physics Division, National Center for Theoretical Sciences, Taipei 10617, Taiwan
[20]Department of Physics and Astronomy, The University of Utah, 115 South 1400 East, Salt Lake City, UT 84112, USA
[21]Instituto de Física, Universidad Nacional Autónoma de México, Cd. de México C.P. 04510, México
[22]Institut de Física d'Altes Energies (IFAE), The Barcelona Institute of Science and Technology, Campus UAB, 08193 Bellaterra
Barcelona, Spain
[23]Instituto de Física Teórica (IFT) UAM/CSIC, Universidad Autónoma de Madrid, Cantoblanco, E-28049, Madrid, Spain
[24]Lawrence Berkeley National Laboratory, One Cyclotron Road, Berkeley, CA 94720, USA
[25]Center for Cosmology and AstroParticle Physics, The Ohio State University, 191 West Woodruff Avenue, Columbus, OH 43210, USA
[26]Department of Physics, The Ohio State University, 191 West Woodruff Avenue, Columbus, OH 43210, USA
[27]Department of Physics, Southern Methodist University, 3215 Daniel Avenue, Dallas, TX 75275, USA
[28]Sorbonne Université, CNRS/IN2P3, Laboratoire de Physique Nucléaire et de Hautes Energies (LPNHE), FR-75005 Paris, France
[29]Department of Astronomy & Astrophysics, University of Toronto, Toronto, ON M5S 3H4, Canada
[30]Department of Astronomy, The Ohio State University, 4055 McPherson Laboratory, 140 W 18th Avenue, Columbus, OH 43210, USA
[31]Institució Catalana de Recerca i Estudis Avançats, Passeig de Lluís Companys, 23, 08010 Barcelona, Spain
[32]Department of Physics and Astronomy, Siena College, 515 Loudon Road, Loudonville, NY 12211, USA
[33]National Astronomical Observatories, Chinese Academy of Sciences, A20 Datun Rd., Chaoyang District, Beijing, 100012, P.R. China
[34]IRFU, CEA, Université Paris-Saclay, F-91191 Gif-sur-Yvette, France
[35]Instituto de Astrofísica de Andalucía (CSIC), Glorieta de la Astronomía, E-18080 Granada, Spain
[36]Space Telescope Science Institute, 3700 San Martin Dr, Baltimore MD 21218, USA
[37]Centre for Advanced Instrumentation, Department of Physics, Durham University, South Road, Durham DH1 3LE, UK
[38]Department of Physics, University of Michigan, Ann Arbor, MI 48109, USA
[39]Research School of Astronomy & Astrophysics, Australian National University, Cotter Road, Weston, ACT 2611, Australia
[40]School of Computing, Australian National University, Acton ACT 2601, Australia"
[41]Kavli Institute for Particle Astrophysics and Cosmology, Stanford University, 452 Lomita Mall, Stanford, CA 94305, USA
[42]Physics Department, Stanford University, Stanford, CA 93405, USA
[43]SLAC National Accelerator Laboratory, 2575 Sand Hill Road, Menlo Park, CA 94025, USA

Abstract

We present Dark Energy Spectroscopic Instrument (DESI) observations of the inner halo of M31, which reveal the kinematics of a recent merger—a galactic immigration event—in exquisite detail. Of the 11,416 sources studied in 3.75 hr of on-sky exposure time, 7,438 are M31 sources with well-measured radial velocities. The observations reveal intricate coherent kinematic structure in the positions and velocities of individual stars: streams, wedges, and chevrons. While hints of coherent structures have been previously detected in M31, this is the first time they have been seen with such detail and clarity in a galaxy beyond the Milky Way. We find clear kinematic evidence for shell structures in the Giant Stellar Stream, the Northeast Shelf and Western Shelf regions. The kinematics are remarkably similar to the predictions of dynamical models constructed to explain the spatial morphology of the inner halo. The results are consistent with the interpretation that much of the substructure in the inner halo of M31 is produced by a single galactic immigration event 1–2 Gyr ago. Significant numbers of metal-rich stars ([Fe/H] > -0.5) are present in all of the detected substructures, suggesting that the immigrating galaxy had an extended star formation history. We also investigate the ability of the shells and Giant Stellar Stream to constrain the gravitational potential of M31, and estimate the mass within a projected radius of 125 kpc to be $\log_{10} M_{\mathrm{NFW}}(< 125\,\mathrm{kpc})/M_\odot = 11.80^{+0.12}_{-0.10}$. The results herald a new era in our ability to study stars on a galactic scale and the immigration histories of galaxies.

1. INTRODUCTION

The histories of galaxies have much in common with that of the United States: in both cases, waves of immigration (of stars, people) have added to the existing inhabitants. In the process of galaxy assembly, smaller galaxies are expected to fall into larger galaxies and disperse their stars in a hierarchical merging process (Bullock et al. 2001; Bullock & Johnston 2005; Cooper et al. 2010). How do we know this? In the case of immigration to the US, numerous documents, such as government records, can be used to reconstruct the historical movements of individuals and therefore large-scale migration patterns. Although no such records are available for galaxies, we can nevertheless reconstruct their immigration histories from the motions of their individual stars. Migrating stars merge into galaxies on cosmic timescales and we can expect to observe stars on their migration paths today; the record of their immigration ancestry preserved in phase space even for migration events that began billions of years ago. Discerning migration events (i.e., to identify coherent structure in the positions and motions of stars on galactic scales) requires measurements of large stellar samples over large areas. Previously prohibitive, such studies are now straightforward with the advent of highly multiplexed multi-object spectroscopy on telescopes with wide fields of view.

M31, our closest large galactic neighbor, has a mass comparable to that of the Milky Way. Our location in the Milky Way offers a fortuitous vantage point from which to observe galactic migration in action in M31. While the Milky Way gives us an up-close ("on-stage") view of the dynamics of a large spiral galaxy, our position within the disk of the Milky Way obscures large portions of the Galaxy from our view. In contrast, with our external ("upper balcony") perspective on M31, it is straightforward to survey the entire galaxy for clues to its immigration history.

The expected observational signatures of galactic migration include debris streams, shells, rings, and plumes, the expected outcomes of merger interactions between large galaxies and their companions (e.g., Bullock et al. 2001; Bullock & Johnston 2005; McConnachie et al. 2009; Cooper et al. 2010; Martínez-Delgado et al. 2010; Pop et al. 2018). The detailed kinematic study of these features can help us reconstruct the assembly history of a galaxy as well as enable dynamical measurements of its mass distribution (e.g., Merrifield & Kuijken 1998; Ibata et al. 2004).

Both the Milky Way and M31 show signs of mergers. Photometric and kinematic studies of the Milky Way reveal complex substructure suggesting that the vast majority of the stars in the halo may have been accreted in past mergers (Bell et al. 2008; Schlaufman et al. 2012; Naidu et al. 2020) with the inner halo dominated by one or more massive satellite galaxies that happened more than 8 Gyr ago (Belokurov et al. 2018; Helmi et al. 2018; Gallart et al. 2019; Bonaca et al. 2020; Kruijssen et al. 2020; Xiang & Rix 2022). In addition, the Milky Way is currently in the process

of assimilating the Sagittarius Dwarf Galaxy, a merger that had its first passage through the Milky Way disk about 5.7 Gy ago (e.g., Ibata et al. 1994; Ruiz-Lara et al. 2020).

Similarly, photometric observations of the M31 stellar halo suggest that our large neighbor has had a complex merger history: its halo shows a high degree of asymmetry, with spatially and chemically coherent structures spread out over its entire extent (e.g., Ibata et al. 2004; Ferguson & Mackey 2016; McConnachie et al. 2018). In particular, the inner halo of M31 contains prominent tidal features, including the Giant Stellar Stream (GSS; Ibata et al. 2001, 2004), which extends 100 kpc to the southeast, and the Northeast and Western Shelves—diffuse but sharp-edged, fan-shaped extensions to the Northeast and West of the center of M31 respectively (e.g., Ferguson & Mackey 2016), structures that have been interpreted as tidal debris from a companion galaxy that merged with M31 relatively recently (e.g., Ibata et al. 2004; Font et al. 2006; Fardal et al. 2006, 2007, 2008, 2012, 2013; Mori & Rich 2008; Sadoun et al. 2014; Hammer et al. 2018; D'Souza & Bell 2018; Kirihara et al. 2017; Milošević et al. 2022).

Spectroscopy of individual stars can greatly enhance our ability to identify migration patterns through the measurement of line-of-sight radial velocities and metallicities. The disk and halo of M31 have been the focus of numerous spectroscopic studies, especially over the last two decades. Most studies of the M31 halo have used the DEIMOS instrument (Faber et al. 2003) on the Keck II Telescope for pencil-beam surveys in various regions, catching tantalizing glimpses of complex kinematic structure. These studies have determined that the GSS is a relatively metal rich ([Fe/H]$\approx$ −0.8; e.g., Gilbert et al. 2019, 2020; Escala et al. 2021), kinematically cold feature (velocity dispersion 11 ± 3 km/s; e.g., Ibata et al. 2004) within a larger metal poor halo, and have revealed an additional cold velocity structure in the region of the GSS (Kalirai et al. 2006a; Gilbert et al. 2009b). The kinematics of the GSS have been used to estimate an enclosed total galaxy mass of $7.5 \times 10^{11} M_\odot$ within 125 kpc (Ibata et al. 2004). The average metallicity of the M31 halo (often derived photometrically) appears to decrease with radius (Kalirai et al. 2006b; Ibata et al. 2014; Gilbert et al. 2014, 2020; Escala et al. 2021), suggesting that much of the inner stellar halo is a mixture of relatively more metal-rich accreted satellite galaxies into the underlying, more metal-poor halo. The kinematically cold substructures like the GSS are found to be more metal rich than the surrounding dynamically hot stellar population (Gilbert et al. 2019), which can be understood if they are produced by fairly massive (and therefore metal-rich) progenitors.

The Dark Energy Spectroscopic Instrument (DESI; DESI Collaboration et al. 2022) on the Mayall 4m telescope at KPNO provides a unique opportunity to advance our understanding of the M31 system. DESI's 3.2° diameter field of view and high multiplex capability ($\approx$5000 fibers) are well matched to the density on the sky of the brightest constituents of M31's inner halo: its asymptotic giant branch (AGB) stars, those at the tip of the red giant branch, and luminous blue stars, stellar clusters, HII regions, and planetary nebulae. Here we present new DESI observations of $\sim$11,000 stars towards M31 that clearly demonstrate that high-quality stellar kinematics can be acquired efficiently over the wide field of view needed to provide unique insights into the migration history of this galaxy.

This paper is organized as follows. In § 2 we describe the M31 observations and the pipeline reductions. In § 3 we present the position-velocity data for the observed sources, revealing complex kinematic structures. We also provide a brief description of the stellar spectroscopic metallicity measurements and their spatial distribution. In § 4, we compare our observations to results from cosmological simulations and explore a more tailored N-body model that demonstrates that much of the observed kinematic structure can result from a single encounter. In § 5, we use the observations to constrain the mass of the M31 system. In § 6 we compare our results to those of previous studies and model predictions, discuss the nature of the progenitor galaxy responsible for the observed kinematic substructure and the constraints we can place on the mass of M31 from these data. We present our conclusions in § 7. The Appendices present tables of the redshifts of non-M31 sources, i.e., higher-redshift galaxies and Milky Way stars, measured by our DESI observations. Throughout this paper we adopt the M31 line-of-sight velocity of −300 $\mathrm{km\,s^{-1}}$ (based on the value of −300$\pm$4 $\mathrm{km\,s^{-1}}$ reported by McConnachie 2012; see also the Third Reference Catalog of Bright Galaxies, de Vaucouleurs et al. 1991), and a distance to M31 of 785$\pm$25 kpc (McConnachie et al. 2005), which results in a scale of $\approx$ 13.7 kpc/deg. We assume that the galaxy disk is centered at (RA,Dec) = (10.6847°, 41.26875°) and viewed at an inclination of 77° to the line of sight and at a sky position angle of PA=38° (see, e.g., Walterbos & Kennicutt 1987; Mackey et al. 2019a). We define the ellipse containing the disk of M31 to have semi-major and semi-minor axes of 1.5° and 0.337° respectively. While heliocentric velocities are presented in the tables, in all figures and discussion we convert all velocities to the Galactic Standard of Rest (GSR; assumes a Solar velocity of [12.9, 245.6, 7.78] $\mathrm{km\,s^{-1}}$ in [x,y,z]) and also reference velocities to a M31-centric frame by adding 113.656 km s^{-1} (i.e., the equivalent of adding 300 $\mathrm{km\,s^{-1}}$ to their heliocentric velocities).

2. OBSERVATIONS AND DATA

2.1. *Target Selection*

The goal of this initial short M31 campaign with DESI, a fiber-fed spectrograph on a 4m diameter telescope, was to determine whether the instrument was capable of measuring stellar radial velocities and spectroscopic metallicities for M31 halo stars. Since the DESI Legacy Imaging Surveys (hereinafter LS; Dey et al. 2019) in the South Galactic Cap only extends south of Dec $\lesssim 33°$ and does not include the region around M31, our primary target selection was based on the source catalogs from the PAndAS survey (McConnachie et al. 2018), g- and i-band survey covering a > 400 deg^2 region around M31 and M33, which we cross matched with the *Gaia* DR2 (Gaia Collaboration et al. 2016a, 2018), and CatWISE2020 (Marocco et al. 2021) catalogs. While the PAndAS data contain $> 10\sigma$ photometry for stars to $g \approx 25, i \approx 24$, our target selection was restricted to stars brighter than $z = 21.5$ mag to ensure measurements of sufficient signal-to-noise ratio in about 90 min of effective exposure time with DESI. Since the PAndAS catalog does not include z-band measurements (which were needed for estimating exposure times and target selection), we constructed an estimate of the DESI Legacy Imaging Surveys z-band magnitude using the following relation:

$$(g-z) = 0.15 \max((g-i)-1.8,0) + 2.21 + 1.27((g-i)-1.8) \tag{1}$$

This relation was derived by cross-matching point sources in PAndAS and LS DR9 in the region where they overlap and fitting a broken linear function to $(g-z)$ vs $(g-i)$. The [16,84] percentiles of the residuals in $(g-z)$ are $[-0.05, 0.11]$ mag for sources with $i \leq 21$ mag.

As M31 is centered at a Galactic latitude of $b = -21.6°$ and this work targets relatively bright stars with $z < 21$, the main contamination to stellar target samples is from Milky Way disk and halo stars. Prior spectroscopic surveys have primarily selected targets using colors in the region spanned by the red giant branch (RGB) isochrones at the distance of M31, and using photometry in the DDO51 intermediate band filter to separate M31 red giants from Milky Way dwarf stars (e.g., Guhathakurta et al. 2006). The resulting samples tend to have $(V-I) \lesssim 2$, which is generally appropriate given the location of the metal poor ([Fe/H] $\lesssim -0.5$) isochrones that define the bulk of the M31 halo.

Our target selection for M31 stars took a different approach, where we primarily focused on maximizing the number of targeted M31 stars with the help of machine-learning-driven classification. We constructed separate selections based on Random Forest classifications optimized for:

- a bright ($z < 19$ mag) M31 disk selection (M31 Disk Bright);

- a faint ($19 \leq z \lesssim 21.5$ mag) M31 disk selection (M31 Disk Faint); and

- a faint ($z \lesssim 21.5$ mag) halo selection, tuned to select targets in the Giant Stellar Stream (M31 Stream Faint).

The Random Forest classification (Breiman 2001) approach uses an ensemble of decision trees constructed from training data. Our classification relies on the following inputs: g and i photometry from the PAndAS catalog; the proper motion (PMRA, PMDEC, PMRA_ERROR, PMDEC_ERROR), parallax (PARALLAX, PARALLAX_ERROR), and photometric (PHOT_G_MEAN_MAG, PHOT_BP_MEAN_MAG, PHOT_RP_MEAN_MAG) data from *Gaia* DR2; along with the *WISE* W1 and W2 photometry (W1MPRO, W2MPRO) from the CatWISE2020 catalogs. When these quantities were unavailable (i.e., for sources too faint for *Gaia* or *WISE*), placeholder values were used (i.e., 99.99). We did not use the PAndAS morphology flags in the Random Forest selection.

Each classifier is trained on a set of stars labeled as either an M31 member or a background/foreground star. Since we do not have an unambiguous classification for every star (as an M31 member or non-member) we use a statistical decontamination approach. Specifically we consider two areas around M31, one centered on an object of interest (i.e., the disk or the GSS), and another far enough away that it would not have many M31 stars. We then remove the (likely) MW contaminants from the first field by picking a nearest neighbor in data-space for each star in the background field (with appropriate scaling to the areas of the field). We are left with a list of objects that are quite likely M31 members in the first field, and background stars in the second field. This provides us with the training set for the random forest. We use a standard cross-validation technique to choose the best tuning parameters of the random forest classifier (such as the tree depth and minimum leaf sizes) and obtain the probabilities for each star that it belongs to M31, P_{M31}. We then select targets with $P_{M31} > P_{cut}$, where the minimum probability P_{cut} is chosen to ensure a high enough target density to match the DESI fiber density.

While the Random Forest results in a fairly complex selection, most of the faint ($z > 19$ mag) targets are approximately bounded by the polygon defined by the points $((g-i), i) =$ ([2.0, 2.4, 3.05, 4.0, 4.0, 2.0], [22.0, 21.67, 21.67, 20.8, 22.9, 22.0]).

The resulting samples for the halo and disk are shown by the filled circles in Figure 1. Our selection is biased to redder regions in $(g-i)$ relative to the selections used by the previous Keck/DEIMOS campaigns. We therefore sample primarily the metal-rich and older RGB and redder AGB stars and do not sample the metal-poor regions well. Despite this bias, the Random Forest approach is "optimal" in the sense of minimizing the contamination by Milky Way stars and background galaxies. Figure 2 shows the density of the selected sources on the sky as well as color-magnitude distributions for the three selections (M31 Disk Faint, M31 Disk Bright, and M31 Stream Faint).
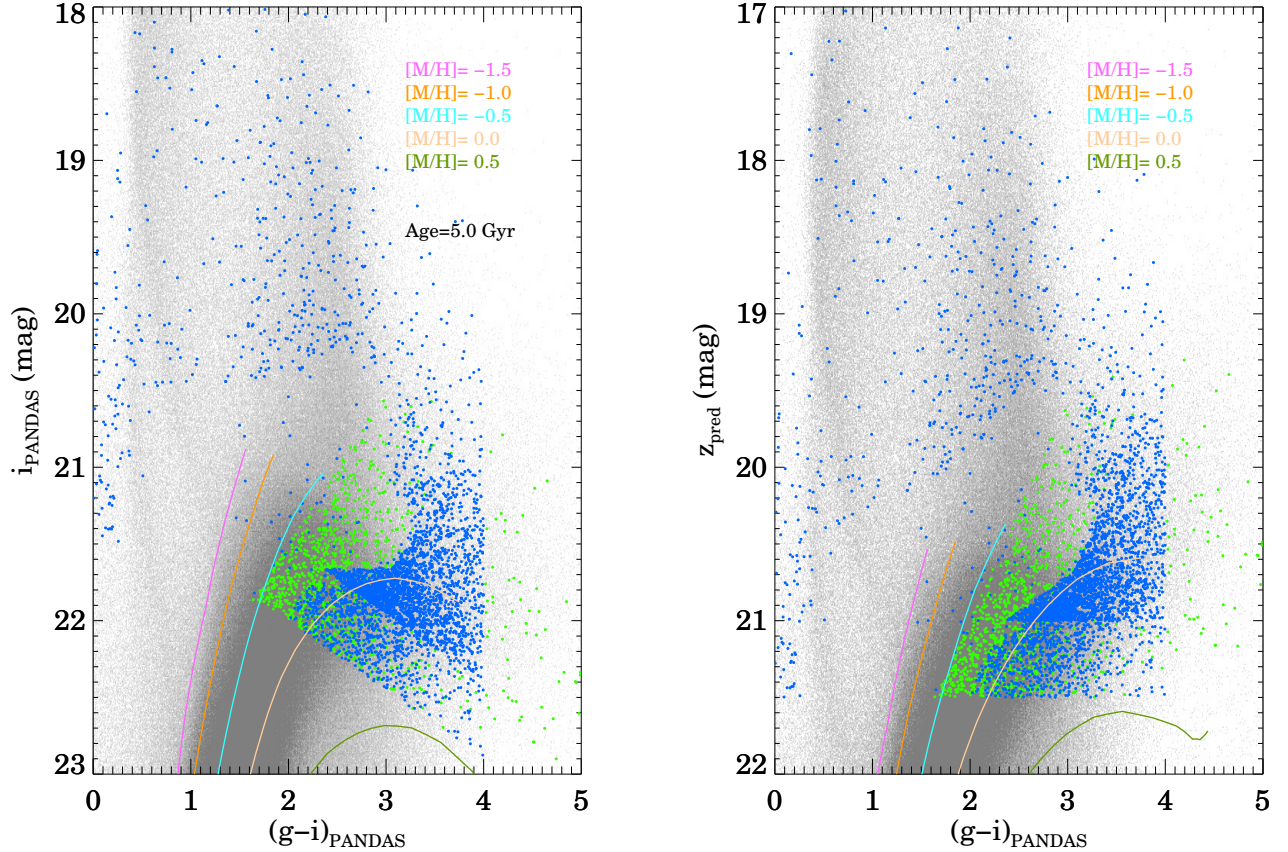
Figure 1. Color-magnitude diagrams for the targets chosen for spectroscopy. The background greyscale in both panels is all stars from the PAndAS catalog within 5° of M31. Representative targets derived from the random forest selection are shown by blue dots and ones chosen by the backup selection are the green dots. The colored lines denote the positions of the PARSEC isochrones (Bressan et al. 2012; Marigo et al. 2013) for an age of 5 Gyr and for metallicities [M/H]=[−1.5, −1, −0.5, 0, +0.5] at the distance of M31.

In the outer regions of the M31 halo, the Random Forest selection results in a target density that underfills the DESI fibers. Hence, we supplemented the Random Forest selection with a simple selection to define backup, or filler targets:

$$z \leq 21.5 \quad \text{and} \quad 20.5 \leq i \leq 24.5$$

$$[23.5 - (g-i)] \leq i \leq [14.5 + 5(g-i)]$$

$$(g-i) \leq 5.0$$

In the disk field (which was originally selected for DESI first light observations), the filler targets included known bright targets—HII regions, planetary nebulae (PNe), globular clusters, luminous blue variables (LBVs)—many of
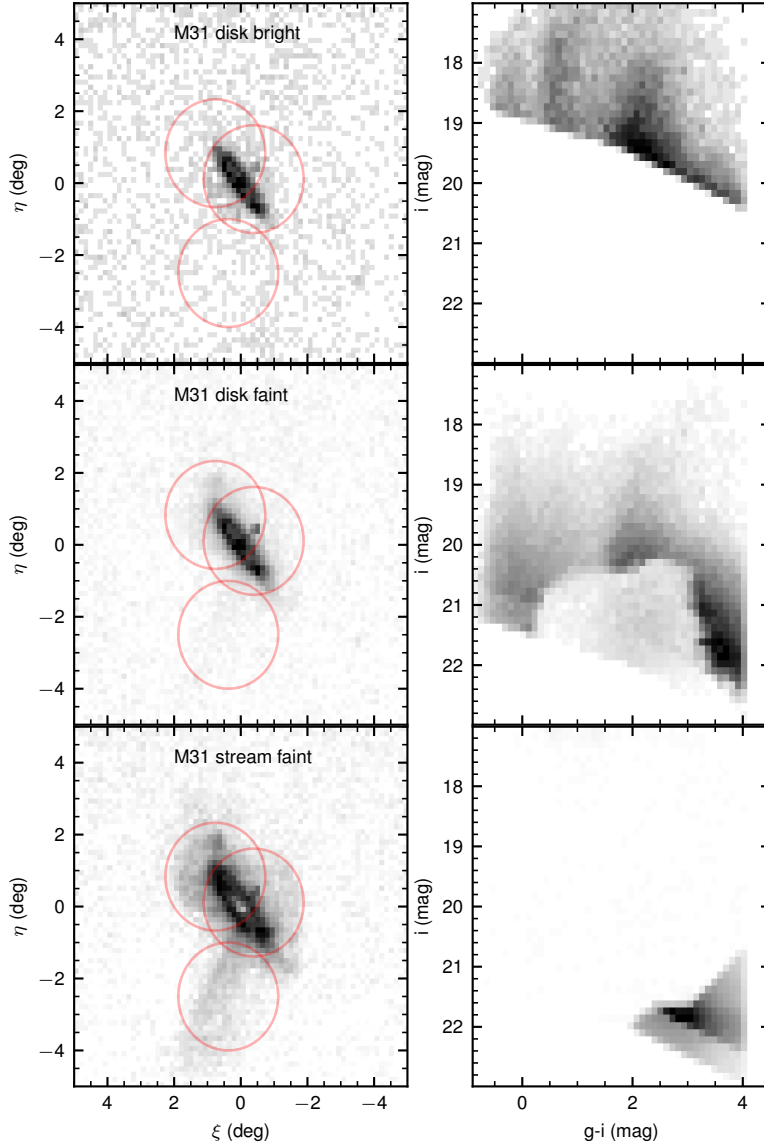
Figure 2. The selection of the M31 targets in our 3 main groups (M31 Bright, M31 Faint and M31 Stream Faint). The left panels show the density of selected targets on the sky. The red circles show the field locations. The right panels show the colour-magnitude distribution of the targets in the form of a Hess diagram.

which have spectroscopic information from past studies and can be used as a check on the DESI radial velocities. HII region and PNe sources were selected from the compilation of Sanders et al. (2012). Globular cluster candidate sources were selected from the compilation of Mackey et al. (2019a) and from Version 5 of the Revised Bologna Catalog (RBCv5; Galleti et al. 2007, 2014). A small number of bright variable sources identified in the Zwicky Transient Survey Catalogs using the ANTARES time-domain event broker (Matheson et al. 2021) were also included, as were bright sources from the SPLASH survey (Guhathakurta et al. 2006; Dorman et al. 2012, 2015). In the M31 halo, the existing spectroscopy at magnitudes DESI can reach ($z \lesssim 21.5$ mag) is more limited, but we included all known cluster and variable sources as potential targets.

Finally, we complemented the list of M31 targets with background QSO candidates selected using data from the *WISE* and *Gaia* satellites. Background QSOs are invaluable probes of the interstellar and circumgalactic medium around galaxies, and all prior studies have only yielded confirmed redshifts for ~ 100 QSOs. We used a simple *WISE* selection (described in Appendix A) to select bright ($G \leq 20.5$ mag) QSOs (with a sky surface density of ≈ 1.8 deg^{-2})

around M31. We vetted this selection using spectroscopically confirmed QSOs from the study of Massey et al. (2019) and the LAMOST surveys (Huo et al. 2010, 2013, 2015).

All these targets were prepared were assigned unique TARGETIDs and prepared for inclusion in the DESI Secondary Target Program. The technical details of DESI target selection, such as the unique TARGETID associated with a target, the different phases of DESI targeting, and how targeting bits can be used to isolate targets from different DESI programs are described in Myers et al. (2022).

2.2. *Observations*

DESI is a wide-field, fiber-fed multi-object spectroscopic instrument mounted on the Mayall 4m Telescope of the Kitt Peak National Observatory. With a $3.2°$ diameter field of view populated by 5020 robotically positioned fibers, DESI offers an unprecedented (and currently unmatched) capability for wide-field astrophysical surveys. Details of the DESI instrument, operational plan, and science mission are presented in DESI Collaboration et al. (2016a,b) and DESI Collaboration et al. (2022). Briefly, the $\approx$1.5 arcsec diameter DESI fibers feed ten three-arm spectrographs which provide continuous coverage over the wide wavelength range 3600Å to 9800Å with a resolving power $R \equiv \lambda/\Delta\lambda$ varying from $\approx$2000 in the blue to 5500 in the red. The three spectrograph arms span the wavelength ranges 3600–5930Å (blue or B), 5600–7720Å (red or R), and 7470–9800 (near-IR, hereafter NIR or Z). DESI is very efficient: its total system throughput varies from 20% at 3800Å to nearly 50% at 8500Å (not including fiber aperture losses or atmospheric extinction) and has an overhead of less than 2 minutes between exposures (for details see DESI Collaboration et al. 2022). Technical details of DESI operations, such as the unique TILEID associated with a tile (i.e., a specific fiber assignment configuration centered at a given sky location), and how DESI observations are planned and proceed, are detailed in Schlafly et al. (2022).

DESI "tiles" were constructed, each incorporating targets from all three selections described above. DESI observations of M31 were obtained in 2021 January (TILEIDs 80713 and 80715, covering the optical disk of the galaxy) and 2022 January (TILEID 82634, positioned on the Giant Stellar Stream; and 82635, targeting the Northeast Shelf; see Table 1). The 2021 January data (on M31's disk) were taken during the early Survey Validation phase of DESI observations, when the instrument was not fully operational and observing procedures were being tested. Tile 80713 was observed on the night of 2021 January 10 in mediocre observing conditions for an effective exposure time[1] of $t_{\rm eff}$ = 758 sec, but the bulk of the fibers were not positioned correctly due to a bug, and the observation resulted in usable spectra for only 730 targets. The tile was redesigned (with all the same targets) as TILEID 80715, and successfully observed on the night of 2021 January 15 for $t_{\rm eff}$ = 1906 sec. During these observations, Petal # 3 (i.e., the $36°$ pie-shaped focal-plane wedge containing 500 fibers spanning the position angle range $270° < PA < 306°$) was non-functional. As a result, no data were obtained on a portion of the Western Shelf region of the M31 inner halo during these observations.

DESI observed the tile centered on the Giant Stellar Stream (TILEID=82634) on the night of 2022 January 3. These observations were obtained under excellent conditions: dark, clear skies with seeing of $1''$, and an effective exposure time of 1.5 hr was reached in 63 minutes. The tile centered on the Northeast Shelf (TILEID=82635) was observed on the nights of 2022 January 21 and 2022 January 27, under somewhat poorer conditions.

In summary, DESI observed a total of three tiles with a total effective exposure time of $\approx$ 3.75 hr. The tiles 82634 and 82635 were each observed for an effective time of $\approx$1.5 hr.

2.3. *Data Reduction*

The data were processed using the standard initial data reduction pipeline corresponding to the internal data release "Fuji" (Guy et al. 2022). There were however several modifications required to process the M31 data. Initially the targeting for tile 80713 did not have correctly identified flux calibration standards as it was located outside the LS footprint. As a result, it could not be processed with the default DESI pipeline parameters, and we therefore manually identified a set of stars as flux standards through color-magnitude selection in *Gaia* G/BP/RP bands and provided the TARGETIDs of these new flux standards to the spectroscopic pipeline. Subsequent to the first observations of the 80713 tile, DESI targeting is now able to correctly deal with fields outside the LS footprint and the standards are selected purely through *Gaia* photometry, with no custom flux calibration standards needed.

---

[1] The DESI effective exposure time corresponds to the time required to reach the observed signal-to-noise ratio under the "standard" observing conditions of a dark sky with ideal transparency and median seeing of $1.1''$ at an airmass of 1.0 (i.e., at zenith). See Guy et al. (2022) for details.

Table 1. DESI Observations of M31[a]

Obs Date	Tile ID	RA_{cen}	DEC_{cen}	Exposure Time	t_{eff}	N_{targ}	Comments
2021-01-10	80713	10.170	+41.380	2700	758	730[b]	Petal 3 non-functional; limited fiber reach
2021-01-15	80715[c]	10.170	+41.380	2700	1906	3130	Petal 3 non-functional; limited fiber reach
2022-01-03	82634	11.185	+38.768	3809	5400	4215	
2022-01-21	82635	11.700	+42.100	2960	1800	4263	
2022-01-27	82635	11.700	+42.100	5003	3600	4263	

[a] Columns are: (1) Local date (at Kitt Peak) for the observation (in yyyy-mm-dd format); (2) DESI Tile Identification Number; (3,4) RA and Dec in J2000 for the center of the tile; (5) the on-sky actual exposure time; (6) the effective exposure time; (7) the number of sources successfully targeted during the observation; (8) comments on the observation.

[b] The bulk of fibers in these observations did not reach their targets because of an error in the fiber assignment file.

[c] Tile ID 80715 is a duplicate of 80713 (i.e., identical targets), with the errors in the 80713 assignment file corrected.

We visually inspected the spectra using the "Prospect" tool[2] created by E. Armengaud (for further details please see Alexander et al. 2022; Lan et al. 2022). An initial visual inspection (VI) revealed that spectra with low quality flags (i.e., $0 \leq$ VI_QUALITY ≤ 2) are located near the disk of the galaxy where the sky subtraction is poor due to the sky fibers being contaminated by emission lines and continuum light from the M31 disk. While DESI observations typically reserve 50-100 fibers for sky observations ("sky fibers"), the pipeline can successfully subtract the sky with minimal additional noise or systematic issues using as few as 10 sky fibers. We therefore examined each of the sky fibers, identified ones with the lowest median flux[3], and then reran the pipeline reductions using this subset. This re-reduction corrected the bulk of the problems with the sky subtraction.

After the initial pipeline data reduction, the data were then processed through the redshift and stellar radial velocity/parameters pipelines. The initial catalog of redshifts was obtained with the Redrock package[4] (Bailey 2012, 2022) which estimates redshifts by fitting a set of eigenspectra to the DESI spectra. The eigenspectra are constructed from star, galaxy, and QSO templates and are optimized for determining the velocities of galaxies over a wide range in redshift (from $-1100 \, \mathrm{km \, s^{-1}}$ to $z = 6$). To determine the radial velocities and stellar parameters, we also used the Radial Velocity pipeline (RVS) that is built on the RVSpecFit code[5] (Koposov et al. 2011; Koposov 2019) and is used by the DESI Milky Way Survey (MWS). Details about the RVS pipeline and its outputs are provided in the MWS overview paper (Cooper et al. 2022), while here we provide a brief summary. The stellar models for the fitting are built using the interpolated PHOENIX stellar atmosphere models (spanning effective temperatures $2300 \leq T_{eff} \leq 15000 \mathrm{K}$) from Husser et al. (2013) convolved to DESI resolution. These models are fit simultaneously to all three arms of the DESI spectra by optimizing the combined χ^2. The spectra are not continuum normalized; instead we fit the spectra directly with functions of the form $T(\lambda)P(\lambda)$ where $T(\lambda)$ is the interpolated stellar template from the PHOENIX models and $P(\lambda)$ is a polynomial that takes care of potential flux calibration and/or normalization differences between the data and the model. The model fit provides estimates of the stellar atmospheric parameters $\log g$, T_{eff}, [Fe/H] and [α/Fe] together with heliocentric radial velocities in the range $|V_{los}| \leq 1500 \, \mathrm{km \, s^{-1}}$.

For each DESI target, we therefore have two velocity estimates, one from Redrock and the other from the RVS pipeline. For stars, the two pipelines agree extremely well: the median radial velocity difference is $0.05 \, \mathrm{km \, s^{-1}}$ and the RMS scatter is $3 \, \mathrm{km \, s^{-1}}$. The accuracy of the stellar parameter determination by the RVS pipeline is discussed in the MWS overview paper, although the M31 data, especially the observation of the outer halo, represent a very different regime than most of the main MWS, as the majority of the M31 targets are very faint cool giants, where the dominant spectral information comes from the molecular absorption bands (the stellar atmosphere grid used by the RVS pipeline extends to effective temperatures of $2300 \, \mathrm{K}$ and works well for these sources; Cooper et al. (2022)). We

[2] https://github.com/desihub/prospect

[3] We selected sky fibers which satisfied $(\bar{s}_i - \bar{s}_{<70})/\bar{s}_{<70} \leq 0.2$, where $\bar{s}_i$ is the median value of the sky in sky fiber i measured in the wavelength region $\lambda\lambda 6000-7000$Å, and $\bar{s}_{<70}$ is the similarly measured median sky value measured across all the sky fibers after rejecting the 30% of the fibers with the highest skies. This procedure resulted in ≥ 10 sky fibers per petal which could be used for sky subtraction.

[4] https://github.com/desihub/redrock

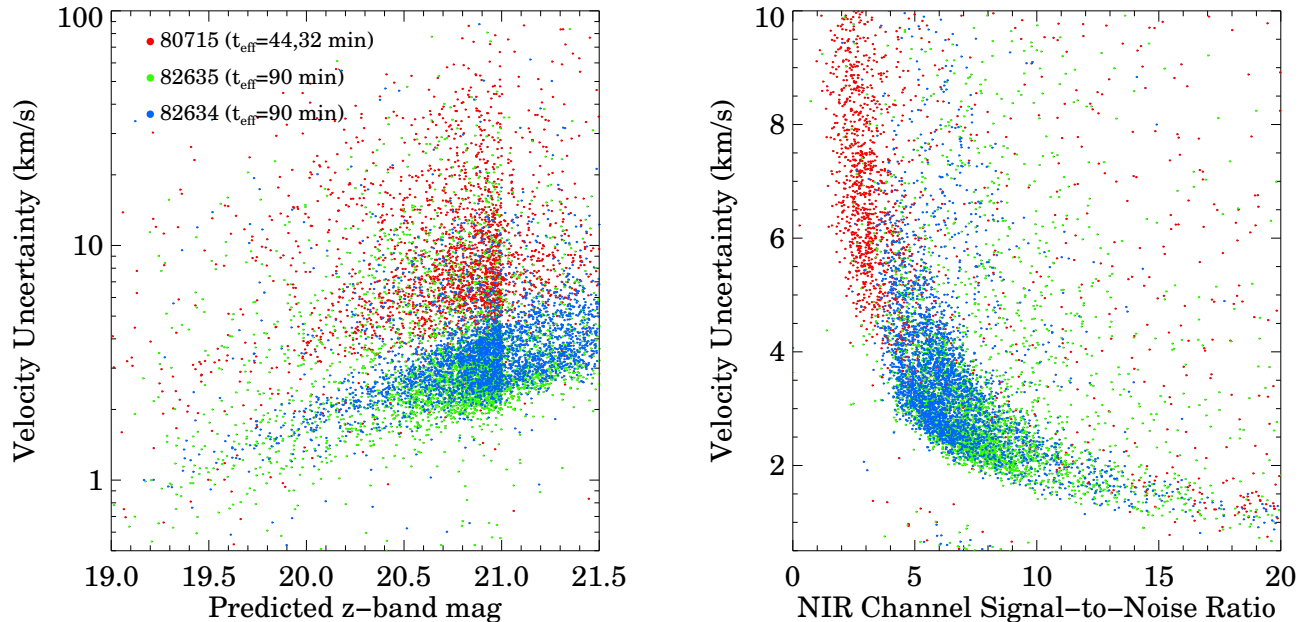[5] https://github.com/segasai/rvspecfit

Figure 3. The distribution of measured radial velocity uncertainty in the DESI spectra as a function of predicted z-band magnitude (left panel) and the mean signal-to-noise ratio per pixel in the NIR channel of the DESI spectrographs (right panel) in the fields centered on the disk (red points), GSS (blue points) and Northeast shelf (green points). For the nominal effective exposure time of 90 min (achieved for the halo tiles 82634 and 82635), the majority of the $z < 21.5$ mag stars have velocity uncertainties $\sigma(V_{\rm los}) < 5$ km s^{-1}.

found that the surface gravity estimates are particularly useful to identify M31 members and separate them from the Milky Way contaminants. For the nominal effective exposure time of 90 min (achieved for tiles 82634 and 82635), the majority of the $z < 21.5$ mag stars have velocity uncertainties $\sigma_V < 5$ km s^{-1} (Figure 3). We expect that the estimates of [Fe/H] should be accurate to ~ 0.2 dex except for the faintest objects (Cooper et al. 2022). The estimates of [α/Fe] are more uncertain and require better calibration datasets for comparison; the discussion of the [α/Fe] measurements is therefore postponed to a future study.

Four of the authors (GM, JJZ, JN, AD) visually inspected 3,150 of the spectra using the "Prospect" spectral inspection (VI) tool. We inspected all spectra for which Redrock returned a SPECTYPE of GALAXY or QSO, found a redshift of $z > 0.001$, or where the target was selected to be a QSO. In addition, we visually inspected the spectra of all targets selected from previous catalogs (i.e., the globular cluster, planetary nebulae, and variable star candidates). Further, we also visually inspected all the well-measured (i.e., RVS_WARN=0; see Cooper et al. 2022, for details) sources for which the Redrock- and RV-measured velocities differed by more than 50 km s^{-1}. Spectra were visually classified according to three broad types (STAR, GALAXY, and QSO) and assigned a quality flag (varying from 0 = 'No useful data' to 4 = 'robust redshift and spectral type') based on the reliability of the redshift estimate.

To create a final catalog, we retained only sources for which a velocity could be determined, i.e., sources with quality flags of 3 or 4 (which only excludes 6.3% of the VI-ed sources). The catalog reports a "best" velocity, selected from among the velocity measured by VI and those reported by the analysis pipelines. If the VI velocity was within 100 km s^{-1} of either the corresponding RVS or Redrock values, both of which were determined with greater precision than the VI value, we selected the value closer to the VI value. Conversely, if the VI velocity was > 100 km s^{-1} away from the RVS and Redrock values, we selected the VI velocity.

3. SPECTROSCOPIC RESULTS

3.1. *Measurements*

The DESI observations resulted in spectra of 11,554 unique astronomical targets. Of these, 683 are confirmed as galaxies and 184 as QSOs (see Appendix A). 10,414 of these are sources within M31 or foreground stars in the Milky
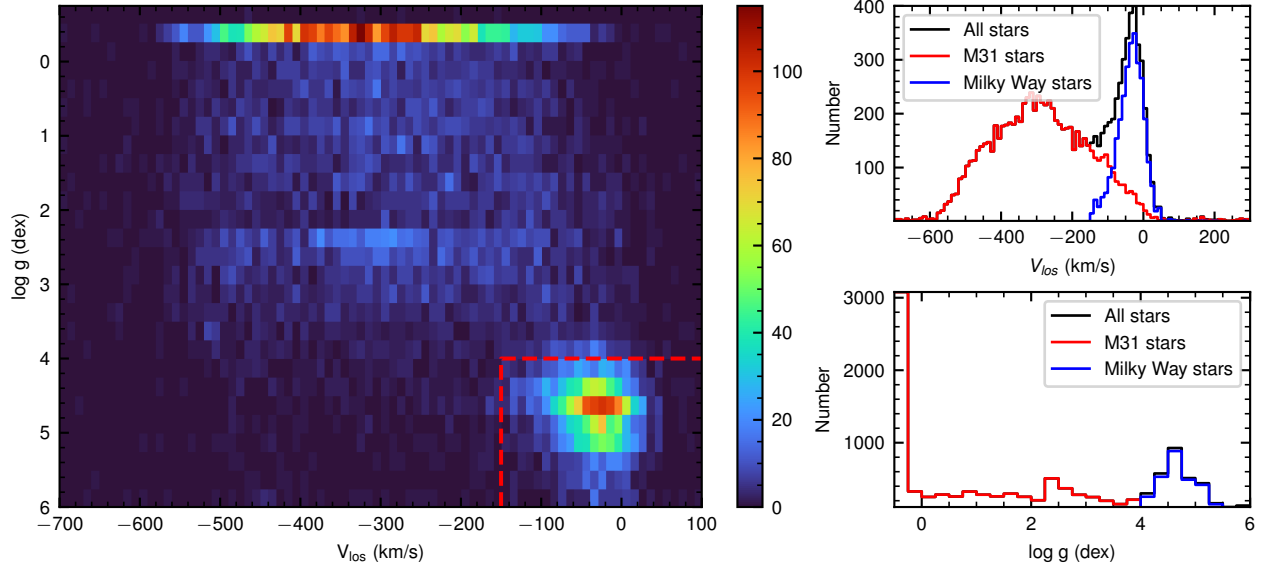
Figure 4. Isolating a robust sample of M31 sources. *Left panel:* distribution of stars with RVS_WARN=0 in the space of radial velocity and surface gravity. The color-bar indicates the number of stars per bin. Milky Way stars are mostly nearby disk dwarfs with $V_{\rm los} \approx -50$ km s^{-1} and high surface gravities (log (g)), and are seen as the clump shown in the lower right. Because the M31 stars are giants with low log(g), we can exclude Milky Way stars by requiring log(g)≤ 4 or heliocentric line-of-sight velocity $V_{\rm los} \leq -150$ km s^{-1} (red dashed line). The log(g) estimates for stars in M31 are not evenly distributed, but exhibit "gridding"; i.e., they tend to values that form the grid of PHOENIX spectral models (see Cooper et al. 2022, for details). *Right panels:* resulting radial velocity (top) and surface gravity (bottom) selection histograms of M31 stars (red) and Milky Way stars (blue).

Way. As shown in Figure 4 we can effectively isolate a robust sample of the M31 sources using the following combined criteria:

$$\text{RVS\_WARN} = 0$$

$$\sigma(V_{\rm los}) \leq 20 \text{ km s}^{-1}$$

$$\log g \leq 4 \quad \text{or} \quad V_{\rm los} \leq -150 \text{ km s}^{-1}$$

For the subset of sources that were visually inspected, we excluded those sources with VI_SPECTYPE = GALAXY or QSO or $0 \leq$ VI_QUALITY ≤ 2. We note that this is not a 100% complete selection, as there a few objects (~ 100) that seem to belong to M31 based on the radial velocity but have a measured $\log g > 4$.

These criteria result in a final sample of 7,438 stars, 43 HII regions or planetary nebulae, and 136 open or globular clusters. Of the 9266 targets selected using the Random Forest algorithm, 8416 have reliable radial velocity measurements (i.e., no processing errors and $\sigma(V_{\rm los}) \leq 10$ km s^{-1}), and of these 6768 (73% of all targeted) are M31 stars. This high success fraction demonstrates the efficiency of the Random Forest selection. For the backup selection, 213 of the 562 targets (38%) are M31 stars.

In this paper, we present results based on the stars in the M31 halo, i.e., the region outside the ellipse encompassing the disk (e.g., see Figure 5). The spectra of M31 disk sources will be discussed in a separate publication. The measured velocities and positions of the 6,436 confirmed M31 stellar sources are presented in Table 2. The list of spectroscopically confirmed cluster, HII region and planetary nebula candidates is presented in Table 3. We also publish a FITS data table containing the measurements resulting from the analysis of the DESI spectra (see Appendix C). Digital versions of all these tables are available online at https://doi.org/10.5281/zenodo.6977494.

Note—Table 3 is published in its entirety in the machine-readable format. A portion is shown here for guidance regarding its form and content.

Table 2. M31 Stars[a]

ID	RA (°)	Dec (°)	$V_{\rm los}$	$\sigma(V_{\rm los})$	[Fe/H]	σ([Fe/H])	$T_{\rm eff}$	$\sigma(T_{\rm eff})$	log(g)	σ(log(g))	$G_{\rm DR2}$	$g_{\rm PAndAS}$	$i_{\rm PAndAS}$	Alternate Name
1	9.7371301	40.2178233	−472.5	6.7	−1.85	0.06	3643.0	5.0	2.46	0.28	NaN	24.90	21.89	PANDAS 170264
2	9.9989009	40.3012761	−520.7	5.5	0.44	0.19	4389.0	84.4	2.99	0.02	NaN	25.48	22.20	PANDAS 96604
3	10.1620093	40.4871788	−479.8	10.2	−0.05	0.05	4162.9	20.9	3.04	0.02	NaN	22.42	19.74	PANDAS 5541
4	10.2713676	40.3688261	−521.1	4.4	0.42	0.06	3870.8	7.2	2.12	0.01	NaN	25.53	21.77	PANDAS 176484
5	9.9539718	40.3950344	−509.8	5.0	−0.70	0.05	4058.6	15.9	1.94	0.01	NaN	25.85	22.20	PANDAS 96676
6	9.7809551	40.2289816	−489.6	4.6	0.21	0.12	4055.0	69.2	3.21	0.01	NaN	25.40	22.09	PANDAS 54369
7	9.8708426	40.2325316	−413.9	6.0	0.16	0.09	4067.7	39.8	2.82	0.28	NaN	25.86	21.92	PANDAS 171130
8	10.1081926	40.4273066	−503.8	4.6	−0.62	0.04	4130.8	19.5	2.47	0.19	NaN	24.74	21.76	PANDAS 176049
9	10.0735259	40.3537205	−454.4	4.9	−1.08	0.07	3779.1	5.8	0.74	0.00	NaN	25.24	21.78	PANDAS 96643
10	9.964951	40.4045608	−524.8	11.5	0.50	0.07	9800.0	6.2	1.51	0.00	19.92	NaN	NaN	Gaia DR2 381200004684395520
11	9.9106488	40.2671799	−158.2	1.8	−1.12	0.07	4576.7	11.9	4.24	0.01	20.34	NaN	NaN	Gaia DR2 369107977589805824
12	9.7966509	40.2791149	−395.6	11.1	0.88	0.00	4139.0	45.8	4.00	0.01	NaN	25.03	21.69	PANDAS 96533
13	10.0611343	40.2721011	−452.8	5.2	−0.88	0.07	3788.7	5.9	0.21	0.00	NaN	24.92	21.91	PANDAS 174999
14	10.2674759	40.5024538	−461.4	9.7	−0.44	0.04	4067.8	15.3	1.84	0.01	NaN	24.69	21.85	PANDAS 179680
15	10.2065926	40.4144844	−501.4	5.7	−2.12	0.04	3371.2	3.7	0.51	0.00	NaN	24.90	21.82	PANDAS 176513
16	9.7446926	40.3032594	−485.0	4.2	0.07	0.11	5758.0	103.1	3.00	0.01	NaN	23.08	21.59	PANDAS 54401
17	9.8513801	40.3184038	−493.3	4.0	−0.82	0.05	3945.2	7.2	1.69	0.01	NaN	24.29	21.72	PANDAS 174596
18	10.1946551	40.3319622	−482.1	3.9	0.46	0.06	3759.3	5.8	0.97	0.01	NaN	25.71	22.13	PANDAS 176249
19	10.0397343	40.4225761	−499.6	4.7	0.09	0.03	4230.9	18.6	2.60	0.13	NaN	25.76	21.83	PANDAS 96749
20	9.9798933	40.4267977	−506.4	0.4	−0.39	0.02	3851.9	3.2	−0.50	0.00	20.08	21.62	19.35	PANDAS 5270
21	10.0378426	40.3165594	−493.0	5.7	0.41	0.07	4143.4	35.1	2.78	0.22	NaN	24.67	21.81	PANDAS 175068
22	10.1195551	40.3864344	−436.8	9.9	−0.37	0.09	4044.9	32.2	2.84	0.26	NaN	25.02	21.90	PANDAS 175857
23	9.9955093	40.3262261	−478.3	3.5	0.36	0.07	4153.6	32.8	2.54	0.20	NaN	24.80	21.87	PANDAS 175062
24	9.9753384	40.2584122	−482.7	6.0	0.07	0.09	4270.8	48.8	3.67	0.01	NaN	25.13	21.93	PANDAS 174942

[a]See Online Version for complete Table. The columns are: (1) a running index; (2,3) RA and Dec in J2000; (4,5) $V_{\rm los}$, the line-of-sight heliocentric velocity and its formal uncertainty; (6,7) the spectroscopic estimate of [Fe/H] and its formal uncertainty; (8,9) $T_{\rm eff}$, the effective temperature and its formal uncertainty; (10,11) the surface gravity (log g) and its formal uncertainty; (12) the $Gaia$ DR2 G-band flux (NaN if not available); (13,14) the PAndAS g and i magnitude (NaN if not available); (15) an alternate name for the target (i.e., from $Gaia$ DR2 or PAndAS).

Note—Table 4 is published in its entirety in the machine-readable format. A portion is shown here for guidance regarding its form and content.

Table 3. M31 HII, PNe, and GC Targets[a]

ID	RA (°)	Dec (°)	V_{los}	$\sigma(V_{los})$	Target Class	G_{DR2}	g_{PAndAS}	i_{PAndAS}	Alternate Name
35	10.5797000	40.9525000	-442.1	5.1	H2PN	NaN	NaN	NaN	PN168
36	10.6240000	41.0584000	-438.9	7.0	H2PN	NaN	20.94	22.10	PN184
37	10.3057000	41.1931000	-400.6	11.5	H2PN	NaN	22.73	25.33	PN080
38	10.4541000	41.0738000	-513.6	1.4	H2PN	NaN	NaN	NaN	PN129
39	10.4348000	41.0364000	-489.7	3.3	H2PN	NaN	21.42	22.63	PN118
40	10.6293000	40.8846000	-408.9	0.2	H2PN	NaN	NaN	NaN	PN185
41	10.5604000	40.8729000	-471.8	0.1	H2PN	NaN	NaN	NaN	PN165
42	10.4922000	41.1361000	-470.6	2.9	H2PN	NaN	21.47	26.18	PN144
43	10.3843000	41.0033000	-486.6	3.8	H2PN	NaN	21.80	22.02	PN102
44	10.1449766	40.4436903	-496.4	15.2	cluster	20.46	NaN	NaN	GC2196,B196D,B196D-SH08
45	9.8293724	40.3661097	-553.9	0.1	cluster	NaN	NaN	NaN	GC3106,SH06,SH06
46	9.9358057	40.2355292	-475.7	1.0	cluster	NaN	NaN	NaN	GC308,B314,B314-G037
47	9.8905182	40.5207430	-507.2	0.2	cluster	18.17	NaN	NaN	GC305,B311,B311-G033
48	10.1869141	40.8855375	-536.7	2.0	cluster	21.15	NaN	NaN	GC3710,BH10,BH10
49	10.2529516	39.9317236	-235.2	0.3	cluster	19.74	NaN	NaN	GC332,B339,B339-G077
50	10.2205474	40.5888014	-552.0	1.1	cluster	NaN	NaN	NaN	GC9074,KHM31-74,KHM31-74

[a]See Online Version for complete Table. The columns are: (1) a running index; (2,3) RA and Dec in J2000; (4,5) V_{los}, the line-of-sight heliocentric velocity and its formal uncertainty; (6) the reason the source was targeted, i.e., whether it was a potential emission line ("H2PN") or star cluster ("cluster") candidate; (7) the *Gaia* DR2 G-band flux (NaN if not available); (8,9) the PAndAS *g* and *i* magnitude (NaN if not available); and (10) alternate name(s) for the target from Sanders et al. (2012); Galleti et al. (2007, 2014). Note: 'GC' stands for "Galactic Cluster" candidate and does not distinguish between young and old clusters.

3.1.1. *Comparison to Previous Work*

M31 has been the target of several spectroscopic campaigns over many decades. A search of the SIMBAD database (Wenger et al. 2000) resulted in a total of 139,078 entries (for 35,374 sources with unique names) within 5° of M31, of which 73,090 (representing 14,617 unique sources) have reported radial velocities. In addition, the CFA Optical/Infrared Science Archive (Sanders et al. 2012; Caldwell & Romanowsky 2016; Bhattacharya et al. 2019, and references therein) consolidates the many years of MMT/Hectospec and Hectochelle campaigns in M31. Of the 10,322 sources in the Archive that are within 5° of M31, 5064 have measured radial velocities and 2,099 are also included in the SIMBAD list. In summary, there are 17,582 sources with published radial velocities in this region.

The bulk of the literature radial velocities are foreground (Milky Way) stars, and only 6,939 sources have radial velocities typical of M31 (< -100 km s^{-1}). The bulk of these stars lie within the projected area of the M31 main disk and, unlike the DESI data, do not sample the M31 inner halo well.

Thus, the new DESI radial velocities presented here only have a small overlap with the published radial velocity measurements. Only 145 DESI targets have matches (within $1''$) to sources with radial velocities in the literature. Where there is overlap, the DESI radial velocities agree well: they have a median offset of ≈ 2.8 km s^{-1} and an rms scatter of ≈ 14 km s^{-1}. For the matched sources, the median velocity uncertainty of the measurement quoted in the literature is ~ 15 km s^{-1}. The DESI data provide more precise radial velocities, with $\approx 88\%$ of the sources having velocity uncertainties ≤ 10 km s^{-1}.

While most of the spectroscopy to date of individual stars in M31 has been carried out with 6.5-m to 10-m class telescopes (e.g., Ibata et al. 2004; Bhattacharya et al. 2019; Caldwell & Romanowsky 2016; Guhathakurta et al. 2006;
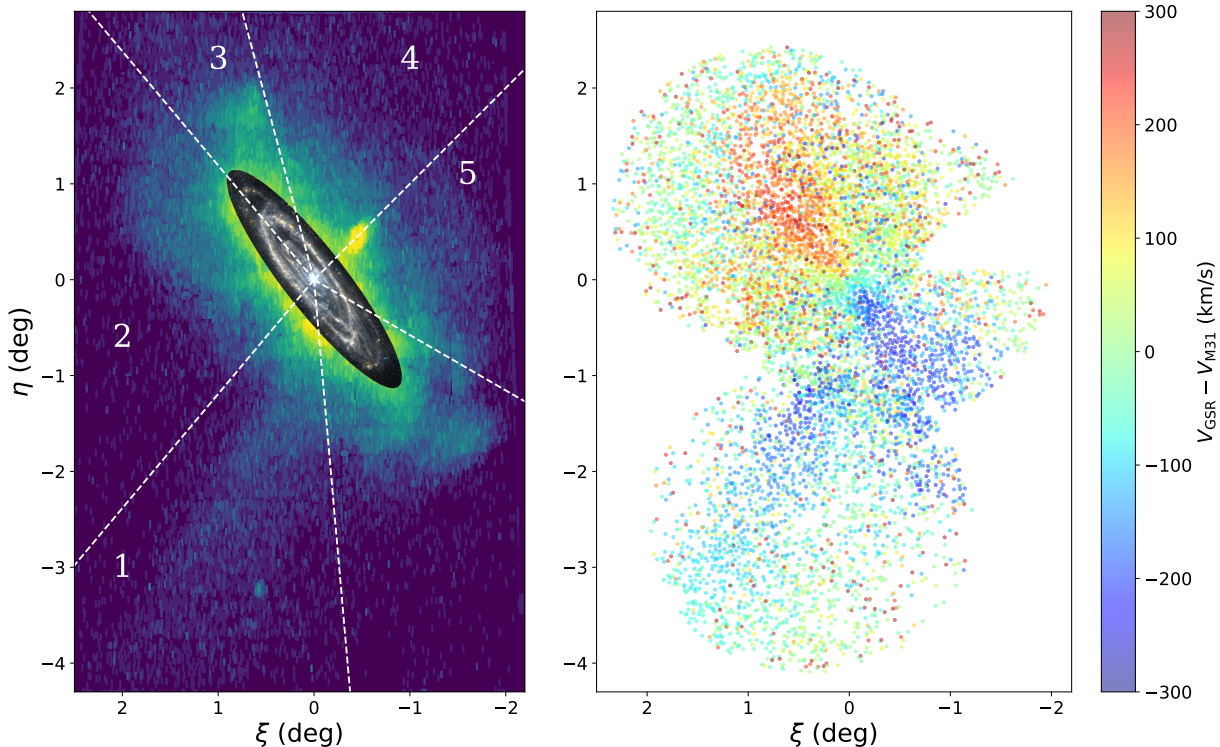
Figure 5. *Left:* Spatial density distribution of sources in the inner halo of M31 from the PAndAS catalog (green-purple color scale; see the text for details) with the unWISE coadded W3/W4 color image superposed for the central galaxy (greyscale; Lang 2014). Dashed lines indicate the five azimuthal zones in which the observed position-velocity structure is analyzed. *Right:* Spatial distribution of the subset of DESI targets selected according to the criteria described in § 3.1. The points are color-coded by radial velocity relative to M31's recession velocity (all in the GSR frame). Highly redshifted and blueshifted stars extend far from the disk. The GSS appears as a stream of blueshifted stars approaching the disk from the south.

Kalirai et al. 2006a,b; Gilbert et al. 2007, 2009a; Dorman et al. 2012; Gilbert et al. 2020; Escala et al. 2019, 2020a,b, 2021, and references therein), the present results illustrate the science potential of highly multiplexed spectrometers on smaller aperture telescopes. A caveat here is that although several campaigns by different groups have targeted the fainter M31 halo populations, the data have not been published along with the papers reporting the results. These campaigns (primarily with Keck/DEIMOS) have targeted primarily giants and horizontal branch stars in M31 in a number of pencil beams scattered across the region. These prior studies typically reach targets fainter than our DESI observations, and include more metal poor RGB targets (e.g., Ibata et al. 2004; Kalirai et al. 2006a; Gilbert et al. 2020; Kirby et al. 2020; Escala et al. 2020a,b, 2022). However, the advantage DESI offers is the ability to (approximately) uniformly sample large spatial regions of the M31 halo both quickly and efficiently: a total DESI on-sky exposure time of ≈ 3.75 hr yielded 11,416 velocities, 7,527 of which are M31 sources with well-measured line-of-sight velocities with uncertainties $\sigma_V \leq 10$ km s^{-1}.

3.2. *Position-Velocity Diagrams*

The left panel of Figure 5 shows the density distribution of sources in the inner halo of M31 selected from the PAndAS catalog (McConnachie et al. 2018) in the region covered by the DESI spectroscopy, with the unWISE coadded W3/W4 image superposed on the central galaxy (Lang 2014). The distribution of inner halo sources shows the previously identified morphological features: the GSS to the SSE; the Southeast and Northeast Shelves; and the Western Shelf (see Ferguson & Mackey 2016, for details). To create the image of the inner halo, we selected catalog sources from the i vs $(g-i)$ color-magnitude diagram that lie within the polygon defined by $[(g-i),i]=[[0.9, 1.8, 5.0, 5.0, 2.2, 2.0], [23, 21, 22, 22.5, 22.5, 23]]$ and used a Gaussian kernel density estimator to adaptively smooth the spatial point distribution of sources. The ellipse separating the inner halo and central galaxy (with semi-major axis $a_e = 1.5°$, semi-minor axis $b_e = 0.337°$, and PA=38° and centered at (RA, DEC)=(10.6847°, +41.26875°)) denotes the disk of M31 and roughly

traces the ring of star formation so clearly visible in young stars and mid-infrared observations of the galaxy (e.g., Barmby et al. 2006; Lewis et al. 2015).

In the left panel, radial dashed lines demarcate the zones in which we explore the position-velocity distributions of the observed sources. The zonal boundaries (see Table 4 for details) are chosen to overlap known overdensities and to distinguish these from each other and the M31 disk. Zone 1 is dominated by the GSS; Zone 2 contains the Southeast Shelf (a portion of which begins in Zone 1) and more than half of the Northeast Shelf; Zone 3 includes the Northeast Shelf and the blobby feature located at $(\xi, \eta) \approx (0.8, 1.8)$; Zone 4 contains the inner halo region just north of the M31 disk; and Zone 5 is dominated by the Western Shelf. The remaining range of azimuth does not contain much DESI spectroscopy beyond the boundary of the disk. Several of these zones include Andromeda dwarf galaxies: Andromeda 1 and M32 lie in Zone 1; Andromeda 9 lies in Zone 2; and NGC205 straddles the boundary between Zones 4 and 5. We neither explicitly targeted nor excluded stars that may be associated with these companions.

The right panel of Figure 5 shows the positions of the measured M31 sources color coded by line-of-sight velocity. There is a clear red-blue asymmetry along the major axis of the galaxy, with an apparent strong flaring and/or a warp near $[\xi, \eta] \approx [+0.7°, +1.8°]$, also observed in the stellar density distribution. We can examine the kinematics of each zone by plotting the line-of-sight radial velocity in the Galactic Standard of Rest relative to M31 (ΔV_{GSR}) as a function of projected distance from the center of M31 (R_{proj}) for the sources in each sector, as shown in Figures 6 and 7. In each panel, stars at velocities $\sim 300\,\mathrm{km\,s^{-1}}$ relative to M31 are primarily foreground Milky Way stars. Figure 8 shows the line-of-sight positions and velocities for stars in all zones and summarizes the linear features in position-velocity space detected in each zone.

The kinematic features are also tabulated in Table 4 and identified by the following convention: a number for the zone, a letter index to distinguish multiple features in the same zone, and a "b" or "r" based on whether the feature is blue- or redshifted relative to the M31 systemic velocity. For example, the GSS feature is labelled as "1ab", meaning that it is feature "a" in Zone 1, and is blue-shifted relative to the M31 systemic velocity. We refer to the GSS and other linear features in Figures 6 and 7 as "streams" based on the previous use of the term in naming the GSS. These "streams" are only-redshifted or only-blueshifted, mostly linear features, in contrast to the features we refer to as "shells", which have the morphology of chevrons or wedges and typically have both red- and blue-shifted components in Figures 6 and 7. In contrast to true narrow Galactic streams such as GD1 (e.g., Koposov et al. 2010), the structures we call "streams" may be more accurately described as "one-sided shells", with their member stars possibly spanning a range of total energies.

The position-velocity diagram for **Zone 1** reveals at least three main features. Most prominent is the GSS (labeled '1ab' in Figure 6), which appears as a tight band of blueshifted stars whose average velocity varies smoothly with distance from $\sim -300\,\mathrm{km\,s^{-1}}$ at $0.5°$ to $\sim -50\,\mathrm{km\,s^{-1}}$ at $4°$ separation from M31. These stars are also highlighted in blue in Figure 9. Our data cover most, but not all, of the entire visible extent of the GSS. Extrapolating linearly, we expect the kinematic structure to cross the zero velocity line at a projected distance of $\approx 5.0°$ from M31.

To determine the velocity dispersion of the GSS, we fit the observations with a two-component model:

$$P(V|R) = f N(V|V_{\mathrm{str}}(R), \sigma) + (1-f) S_{\mathrm{bg}}(V - V_{\mathrm{str}}(R)),$$

where $N(V)$ is a Gaussian density in projected radial velocity that represents the GSS and $S_{\mathrm{bg}}(x)$, which represents the foreground component, is an appropriately normalized piece-wise linear function of the form $\mathsf{min}(\mathsf{max}(x, 0), 1)$. The quantity f is the mixing fraction between the stream and the more smoothly distributed M31 halo stars, $V_{\mathrm{str}}(R)$ is the radial velocity of the stream as a function of distance parameterized by a cubic spline with nine knots, and σ is the velocity dispersion of the GSS. The model has 14 parameters in total and was fitted to the sample of stars between the grey lines shown in the left panel of Figure 10. We use in the fit only stars at projected distances between $1°$ and $3.8°$ from M31 and at position angles between $147°$ and $175°$. The posterior of the parameters is sampled using the dynesty nested sampling code (Koposov et al. 2022; Speagle 2020), and the fitted velocity dispersion is determined to be $10.80 \pm 0.75\,\mathrm{km\,s^{-1}}$. This velocity dispersion is lower than most of the measurements by Gilbert et al. (2009b) of the primary GSS component in the GSS core and envelope region, but is more consistent with their measurement in the "m4" field of $11.4^{+5.2}_{-4.1}\,\mathrm{km\,s^{-1}}$ centered on Stream C. This may be due to the better velocity resolution and better spatial sampling of the DESI study, which results in the ability to cleanly isolate the primary GSS kinematic structure (1ab) from the other components. Given the multiple structures that make up this region of the halo, measuring a single velocity dispersion for all the components together is not physically meaningful. The fitted position-velocity locus of the GSS is provided in Table 7 and used in the mass estimate analysis presented in Section 5.2.
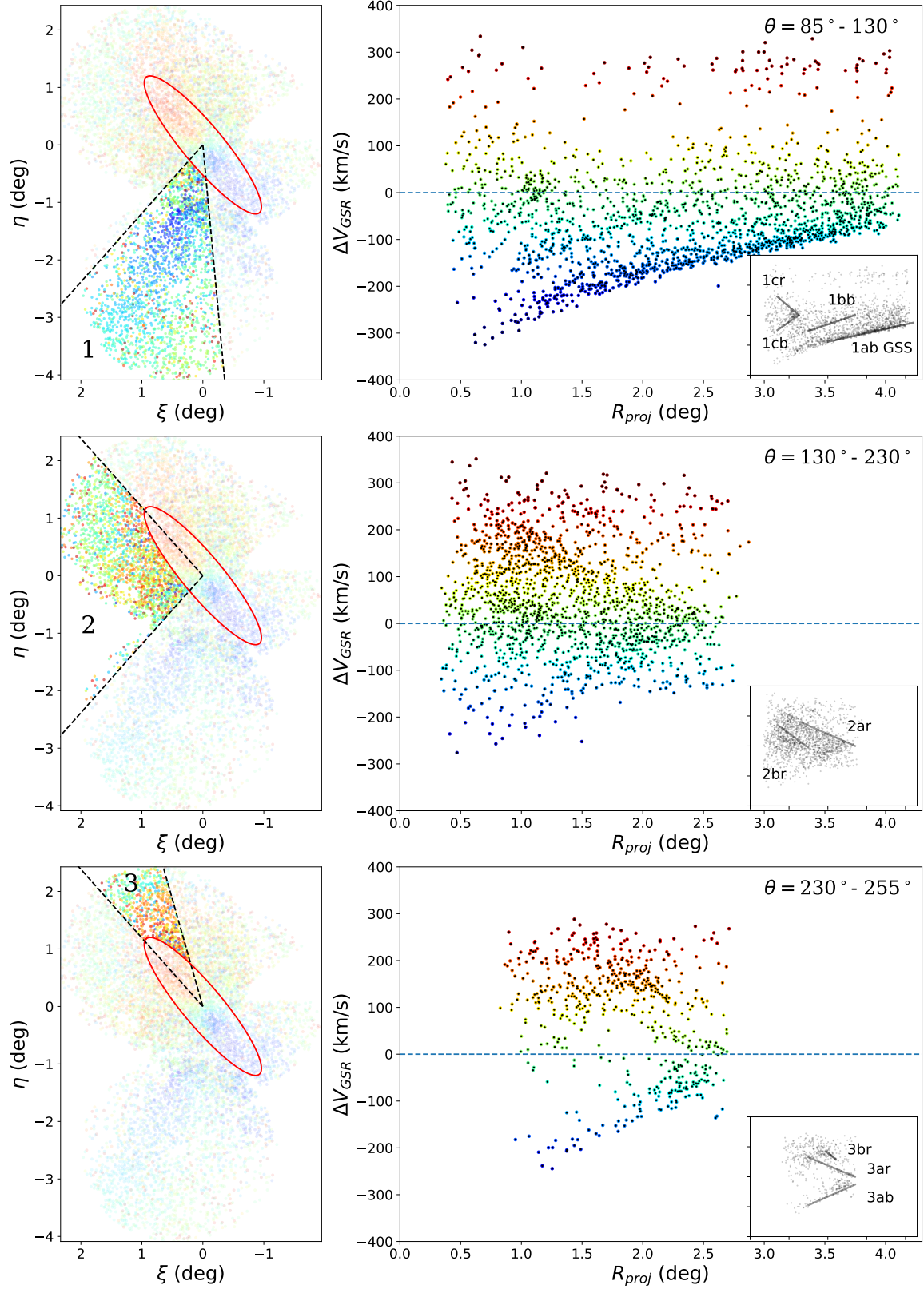
Figure 6. Line-of-sight position-velocity diagrams (right hand panels) for angular zones of interest (left panels). Stars lying within the ellipse centered on M31 (red line) are excluded from the position-velocity diagram. Velocities are relative to the M31 central velocity of V_{los}(M31) = -300 km s^{-1} (i.e., V_{GSR}(M31) = 113.6 km s^{-1}). Insets highlight linear features apparent in each region, which are shown as grey lines. Zone 1 contains the Giant Stellar Stream. Zones 2 and 3 are part of the Eastern Shelf.
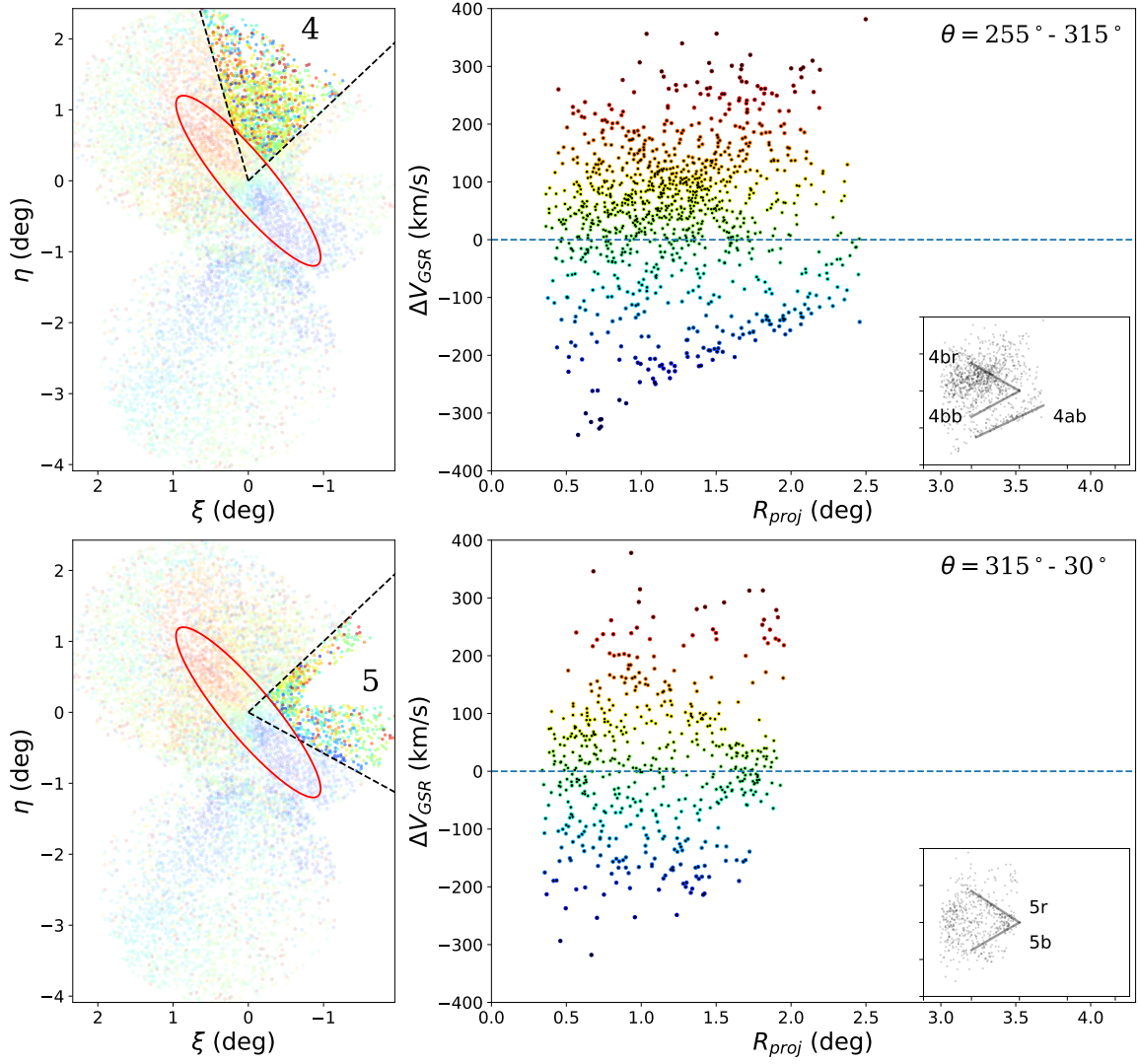
Figure 7. As in the previous figure, for two additional zones. Zone 5 includes the Western Shelf.
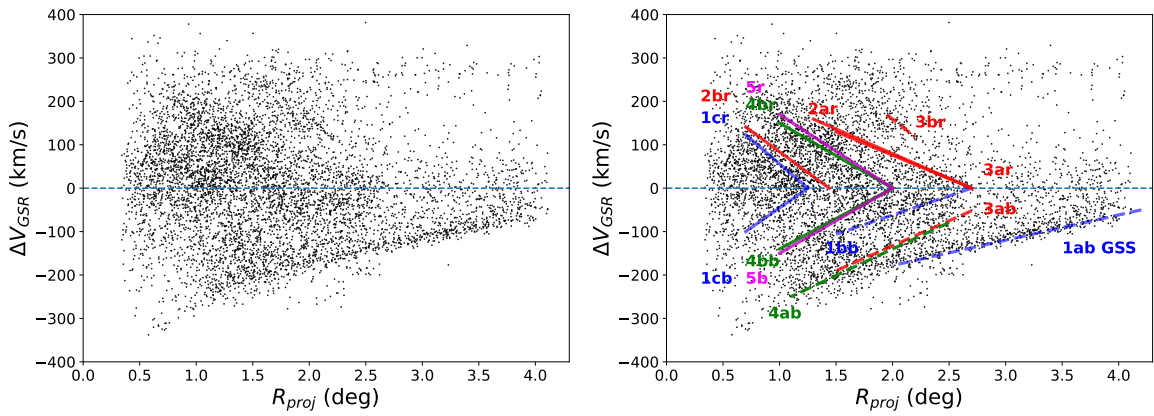
Figure 8. Combined line-of-sight positions and velocities for stars in all zones (black dots, left and right panels). The right panel also shows the linear features highlighted in the insets from Figures 6 and 7 and described in Table 4.
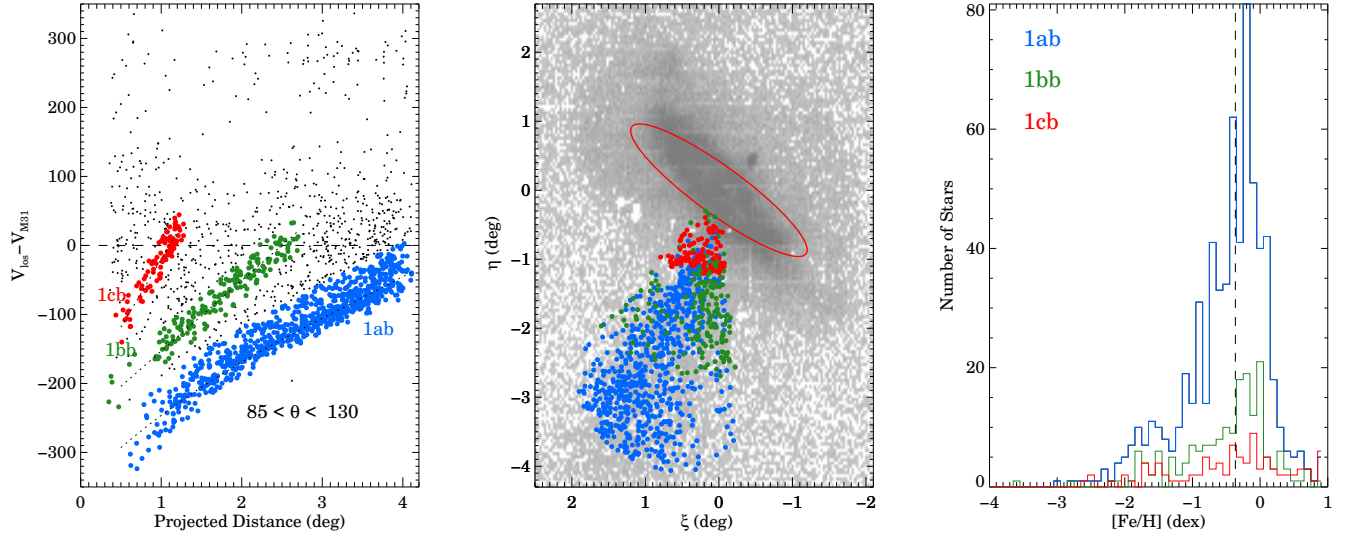
Figure 9. The left panel shows the line-of-sight position-velocity diagram for Zone 1 with the selection of stars in the three main kinematic features as described in the text. The center panel shows the spatial distribution of all observed stars lying within these selection windows. The right panel shows the spectroscopic metallicity distribution of these points and demonstrates that the features 1ab (GSS) and 1bb have similar broad distributions with median [Fe/H]≈ -0.37 dex (vertical dashed line). The metallicity distribution of 1cb is flatter and broader.

Zone 1 also includes another band of blueshifted stars that runs parallel to the GSS in the position-velocity diagram. Less blueshifted by ~ 100 km s^{-1} than the GSS, this kinematically cold component (labeled '1bb' in Figure 6) has a velocity dispersion similar to that of the GSS (see also green points in Figure 9), and is more limited in length, extending to $\sim 2.7°$ from the center of M31. As shown in Figure 9, feature '1bb' is also spatially offset from the GSS, extending outward from the center of M31 at a different mean angle than the GSS stars. Feature 1bb was previously identified in spectroscopy carried out in pencil-beam surveys of discrete portions of the M31 halo (Kalirai et al. 2006a; Gilbert et al. 2009b). Our results are consistent with the velocities previously reported and illustrate, for the first time, the spatially continuous nature of the structure and its spatial offset from the GSS.

We also see in Zone 1 a hint of a more compact feature: a **chevron** pattern, i.e., a concentration of stars along a triangular-shaped edge (its blue- and redshifted edges labeled '1cb' and '1cr' in Figure 6), similar to the general shape expected for radial shells (Merrifield & Kuijken 1998). The chevron extends to $\sim 1.3°$ in projected distance and reaches an apex at a velocity within ~ 30 km s^{-1} of M31 (Figure 6; red points in Figure 9). Higher density sampling is needed to confirm this feature and define its kinematic structure.

Zones 2, 3, and 4 include the Northeast Shelf, which extends out to $\sim 2.5°$ from M31 (Figure 5) and has a shell-like morphology. The position-velocity diagram for Zone 2, which samples the portion of the Northeast Shelf south of the M31 disk, shows a large, prominent triangular **"wedge" shape (a filled chevron)**, with an apex at ~ 0 km s^{-1} relative to M31 at a distance of $\sim 2.5°$ and extending to ± 300 km s^{-1} at $\sim 0.5°$. The redshifted edge of the wedge (labeled '2ar' in Figure 6) is better defined than the blueshifted edge, and the interior of the wedge is more populated at redshifted velocities. Within this feature, a smaller wedge-shaped feature also appears to be present, with an apex at $\sim 1.5°$ distance and extending to ~ 150 km s^{-1} at 0.5° distance (feature '2br' in Figure 6). This feature (2br) may be the continuation of the wedge defined by 1cb and 1cr seen in Zone 1. Escala et al. (2022) also recently reported a wedge-shaped distribution in Zone 2 based on five pencil-beams at distances between $1-2°$ from M31.

The position-velocity plots for Zones 3 and 4, which are radially opposite from Zone 1, show a narrow blueshifted feature with kinematics similar to that of the GSS in Zone 1 (feature '3ab' in Figure 6 and '4ab' in Figure 7. The stars comprising the feature are widely distributed spatially across both zones. Perhaps these are stars that were once in the GSS and have passed back through M31 to the northern side of the galaxy. Such features do appear in merger simulations (e.g., that discussed in Section 4.1). Zone 3 also includes a hint of a narrow redshifted feature (feature '3ar' in Figure 6), which is likely related to feature 2ar in Zone 2. Unlike the wedge associated with 2ar, the wedge associated with 3ar is mostly empty. A striking feature of Zone 3 is the presence of a group of about 40 stars that
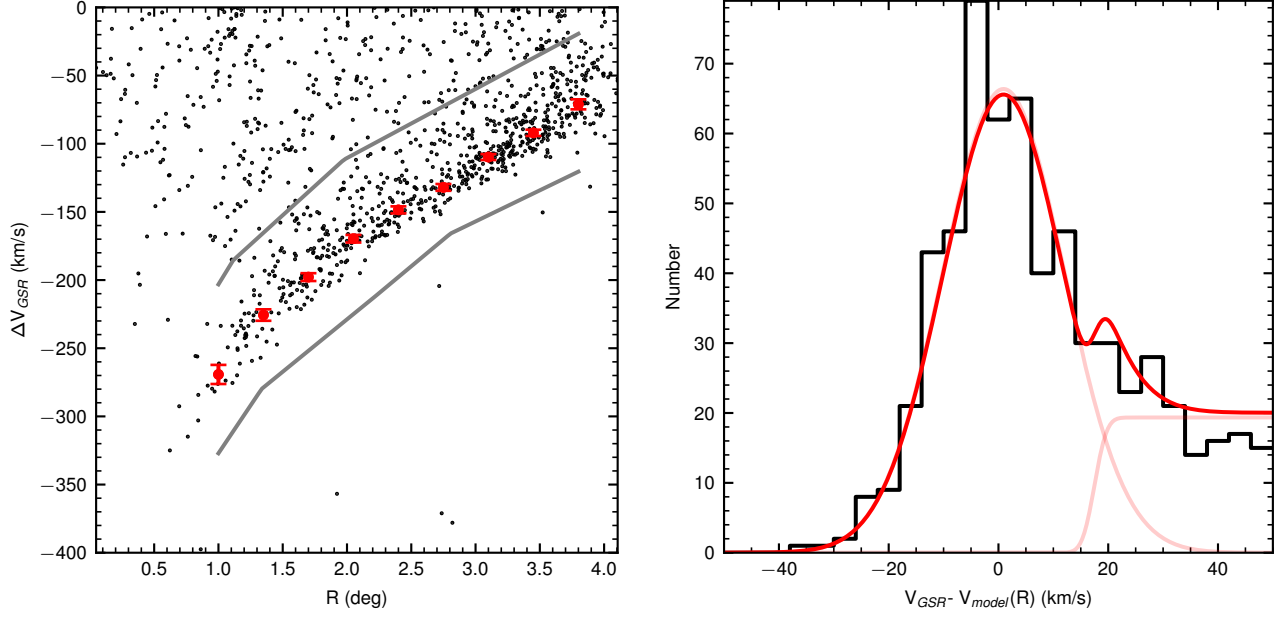
Figure 10. *Left:* Extracted projected radial velocities as a function of projected distance used to define the locus of the GSS. Black points show individual stars in the direction of the GSS. Grey lines bracket the sample of stars used in the fit. Red points with error bars show the extracted locus of the GSS in distance bins. *Right:* Histogram of radial velocity residuals relative to the best-fit locus for the GSS. The model for the radial velocity distribution is overplotted in red. See the text for details.

Table 4. Approximate Parameters of Kinematic Features

Zone	Angular Range[a]	Feature	$R_{\max}$ (deg)	dV_{los}/dR (km s^{-1}/deg)	M_{enc}[c] ($10^{11} M_\odot$)	Type
1	$85° - 130°$	1ab (GSS)	5.057^b	58		Stream
		1bb	2.70	88		Stream?
		1cb	1.25	182	2.0	Shell
		1cr	1.25	-224	3.1	Shell
2	$130° - 230°$	2ar	2.70	-114	8.0	Shell
		2br	1.44	-191	3.4	Shell, related to 1cr
3	$230° - 255°$	3ar	2.70	-108	7.3	Shell, related to 2ar
		3br	–	-202		Short linear feature
		3ab	3.15^b	115		Stream?
4	$255° - 315°$	4ab	3.15^b	122		Stream? related to 3ab
		4bb	2.00	140	5.0	Shell
		4br	2.00	-150	5.7	Shell
5	$315° - 30°$	5b	2.00	150	5.7	Shell, related to 4bb
		5r	2.00	-170	7.3	Shell, related to 4br

[a] Angle is measured clockwise from the $\eta = 0$ axis; i.e., $\theta = 270° - $PA

[b] $R_{\max}$ for features 1ab (GSS), 3ab, and 4ab are determined from the linear extrapolation to $V_{\mathrm{los}} = 0$.

[c] Enclosed masses M_{enc} for shells estimated from Merrifield & Kuijken (1998).

define a short "stub" in the position-velocity diagram, defined as 3br in Figure 6. These stars appear to be at the northeastern and southwestern edges, respectively, of the overdensities defined as the Northern Spur and the Northeast Clump by Mackey et al. (2019a). The 3br feature is notable for its small velocity dispersion of 4.6 ± 1.5 km s^{-1} despite its stars covering the width of the zone. Apart from features 3ab, 3ar and 3br, the rest of the stars in Zones 3 are

preferentially redshifted, as in Zone 2, and scattered across position velocity space. Zone 4 also shows a preference for redshifted stars. The major feature in Zone 4 is a more completely filled wedge bordered by 4br and 4bb.

Finally, the position-velocity plot for **Zone 5** shows a chevron pattern (i.e., the outline of a wedge-like shape; labeled 5b and 5r), similar to the shape expected for radial shells (Merrifield & Kuijken 1998). A similar feature was reported for the Western Shelf region by Fardal et al. (2012, see their Figure 8) based on spectroscopy of stars in a narrow strip along the minor axis of the M31. Here, the stars that make up the chevron pattern are broadly distributed across the Western Shelf feature in Zone 5. The stars that make up the red- and blue-shifted edges (5b and 5r) spatially overlap each other as expected for an umbrella-like fan viewed tangentially (Merrifield & Kuijken 1998). The 5b/5r chevron pattern overlaps the edge of the filled wedge bordered by 4bb/4br (Figure 8).

3.3. *Comparison to Planetary Nebulae from the Literature*

Figure 11 compares the spatial and velocity distributions of M31 stars with those of planetary nebulae (PNe) reported in the literature. The angular zones shown are the same as those shown in Figures 6 and 7, with the exception that Zones 3 and 4 are combined. The PNe shown were identified using SIMBAD and the MMT/Hectospec archive, and are the result of a large body of work by many authors (see Merrett et al. 2006; Yuan et al. 2010; Sanders et al. 2012; Bhattacharya et al. 2019, and references therein). The comparison shows that the known PNe that lie beyond the main disk of the galaxy trace the same kinematic structures visible in the DESI data. The similarity is apparent in all spatial regions of M31, but most strikingly in the regions shown in the bottom two panels. In the angular range $230° < \theta \leq 315°$ (zones 3+4 in Figures 6 and 7 covering the northern portion of the Northeast shelf), the PNe are preferentially redshifted, echoing the distribution of the stars, and roughly demarcate the two wedges visible in the stellar data. At $315° < \theta \leq 30°$ in the Western Shelf (bottom panel, zone 5 in Figure 7), the PNe trace the red- and blue-shifted edges of the chevron. Fardal et al. (2007) previously pointed out how the PNe in the Western Shelf preferentially fall near the boundary of a triangular region in position-velocity space. The present comparison shows how the PNe distribution echoes the more densely sampled stellar distribution over much of the inner halo, as expected. We compare to the distribution of star clusters and dwarf galaxies in § 6.2.

3.4. *Metallicities*

Photometric studies have demonstrated that the M31 halo shows a wide range of stellar metallicities with much of the substructure being metal rich (Ibata et al. 2001; Brown et al. 2006; Ibata et al. 2007; Gilbert et al. 2009a,b; Ibata et al. 2014; Conn et al. 2016). Spectroscopy from Keck/DEIMOS has not only found evidence for a low-metallicity halo component that is detectable both in the inner regions and at large distances, but also confirmed that the stars associated with some of the kinematic substructure are metal rich (e.g., Guhathakurta et al. 2006; Kalirai et al. 2006a,b; Gilbert et al. 2020; Escala et al. 2020a,b, 2021). The metallicity of the Western Shelf (measured photometrically) is the same as that of the GSS (Fardal et al. 2012; Tanaka et al. 2010), with a typical metallicity of $[Fe/H] = –0.7$ for the satellite debris and –1.2 for the spheroid component of M31. Since the selection of targets for the DESI observations presented here is biased toward redder colors (and thus higher-metallicity populations) and does not sample the metal-poor RGB populations, we cannot use the DESI data to infer directly the metallicity distributions in the different kinematic components. However, we do find significant numbers of metal-rich stars across all regions surveyed. For the stars in the region of the GSS, Figure 9 shows that we measure similar median metallicities in the three different kinematic components (the median metallicities in 1ab, 1bb, and 1cb are −0.33, −0.26 and −0.32, respectively, with all the observed stars in this zone – represented by the dashed line – showing a median metallicity of −0.37).

The overall distribution of metallicities is remarkably similar to that presented by Fardal et al. (2012, see their Figure 11), showing a skewed distribution with a tail to lower metallicities. This similarity is surprising given that our target selection is biased toward the high-metallicity regions of the color-magnitude diagram. The presence of lower-metallicity stars in our sample may result from photometric scatter in the PAndAS data (i.e., with the more metal-poor stars scattering into our selection region). Nevertheless, assuming that the DESI data only sample the high-metallicity tail of the distribution, the measurements suggest $[Fe/H] \lesssim −0.4$ is a strong upper limit to the median metallicity in these regions. There is weak evidence that the metallicity distribution in the compact wedge component in Zone 1 (1cb; shown by the red points in Figure 9) is flatter (i.e., stretching to higher metallicities) than the main 1ab (GSS) and 1bb components. However, this component may also be contaminated by stars from the M31 disk and bulge.

We see no significant variation in the metallicities in the region of the GSS (Figure 12) either along the radial direction (left panel) or with azimuthal angle (right panel). Previous photometric studies have reported spatial variations of the
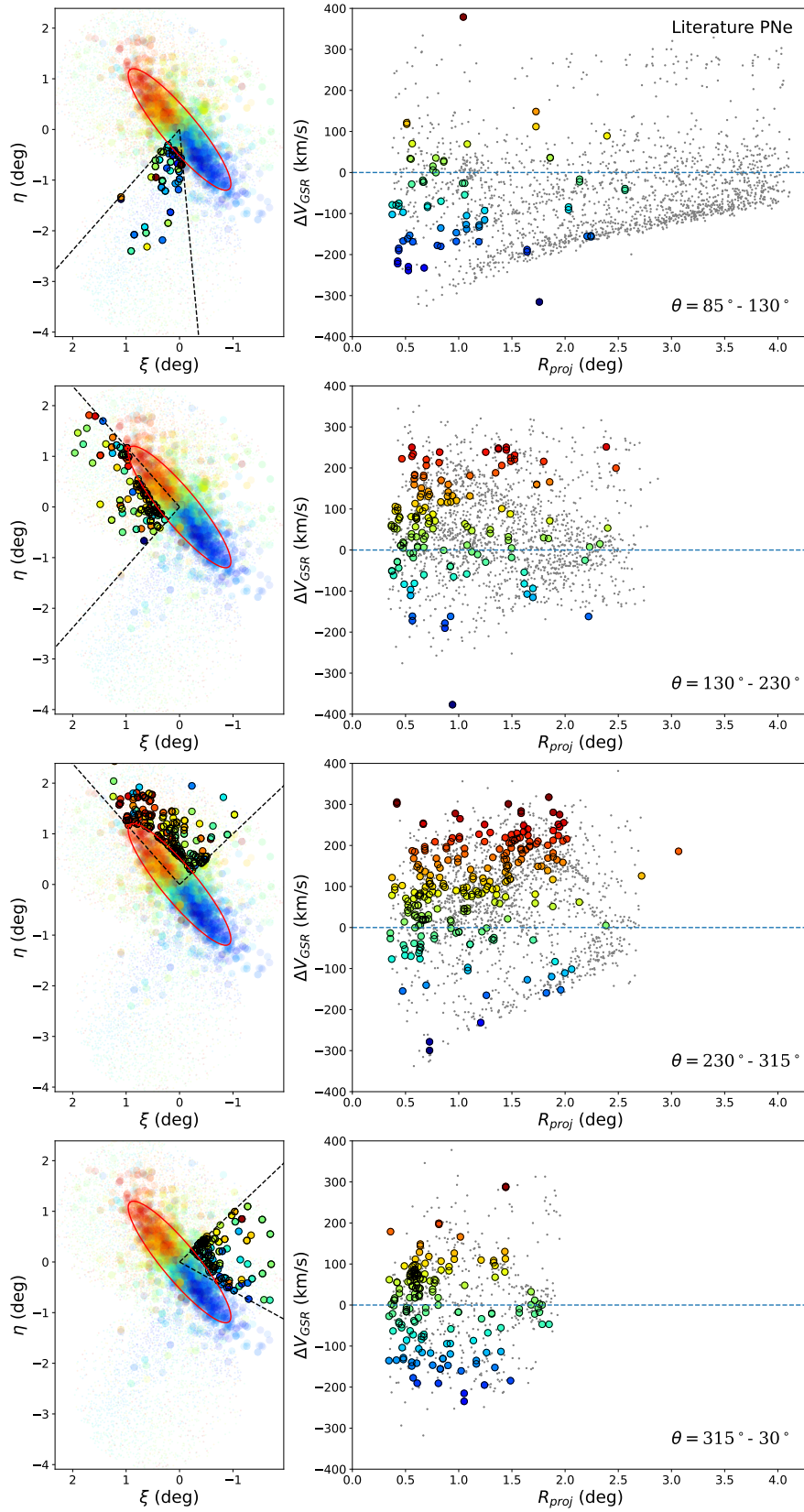
Figure 11. The distribution of known PNe from the literature (large colored circles; see the text) overlaid on M31 stars (smaller points).
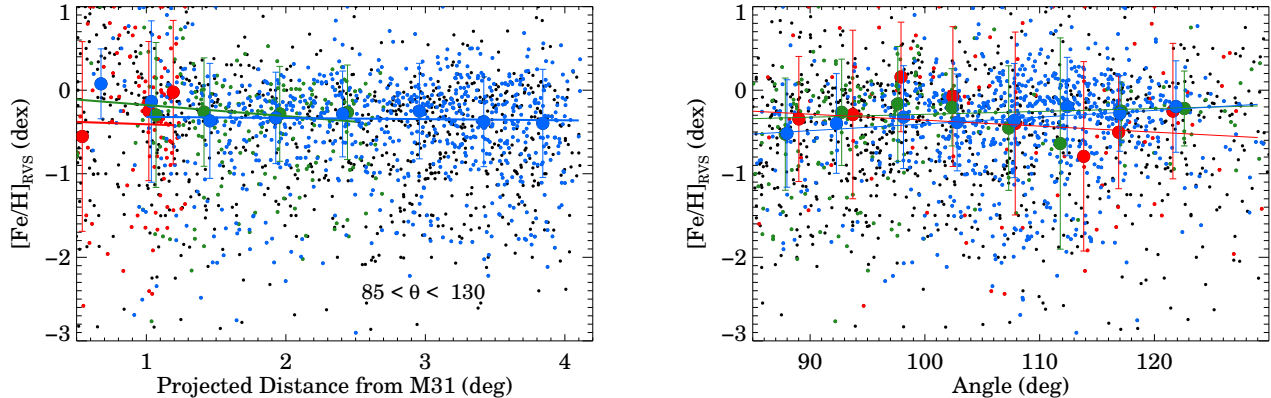
Figure 12. Variation of [Fe/H] as a function of position in the region of the GSS as a function of projected radial distance from M31 (left) and angle around M31 (right). The blue, green and red dots respectively represent stars associated with the three kinematic structures 1ab, 1bb, and 1cb shown in the left panel of Figure 9; the black dots represent the remaining stars in Zone 1. The large solid dots with error bars represent the median values and the 1σ scatter, respectively, in the [Fe/H] values in equal bins of projected distance or angle. The solid lines show least absolute deviation fits to each subset. There is no significant variation in the mean metallicity in either direction within the DESI sample.

metallicity: Conn et al. (2016) found that the metallicity in the GSS region increases from [Fe/H] ≈ -0.7 at $R_{\rm proj} \approx 1°$ to about -0.2 near $R_{\rm proj} \approx 2.8°$, and then decreases steadily to [Fe/H] ≈ -1 at $R_{\rm proj} \approx 5.9°$. The pencil-beam spectroscopic metallicity estimates by Escala et al. (2021) found a gradient of -0.25 dex/degree, even stronger than those reported by Conn et al. (2016). While the DESI measurements in Figure 12 show a high mean value of the metallicity, they also show large scatter with no statistically significant systematic trends. However, we caution that these results may be due to our biased selection of targets, and a more comprehensive study of the metallicity variations would require a more complete sampling of the low-metallicity portions of the RGB (by future observations) and a careful accounting of the selection function.

4. COMPARISON TO SIMULATIONS

4.1. *Comparison to Galaxy Formation Simulations in a cosmological context*

Simulations of galaxy formation in a cosmological context illustrate how mergers can generate complex, organized structure similar to that observed in M31. To illustrate this point, we show in Figure 13 an example of a system like M31 which experienced a fairly massive merger in the last few Gyr. This example is not meant to replicate M31 in any detail, but is provided only to illustrate how streams and shells emerge naturally in cosmological simulations. The example is taken from the TNG-50 simulation (Pillepich et al. 2018, 2019), which simulates a large cosmological volume (51.7 Mpc on a side) with high resolution (300 pc softening length for the collisionless particles), enabling an analysis of the detailed kinematics of merger debris.

To identify this system within the simulation, we began by selecting systems with properties similar to that of M31 (Ibata et al. 2014; D'Souza & Bell 2018, 2021), i.e., systems with stellar masses $5\times10^{10}\,M_\odot$ to $15\times10^{10}\,M_\odot$. We selected galaxies that have a prominent disk by requiring that more than 40% of stars are on orbits that have a circularity $\epsilon = J_z/J(E) > 0.7$, where J_z is the specific angular momentum of a particle around the angular momentum axis of the stellar body of a galaxy, and $J(E)$ is the maximum angular momentum of the 100 particles with the most similar total binding energies (see also Genel et al. 2015). In addition, we required that the galaxy have a total accreted stellar mass of at least $3 \times 10^9\,M_\odot$ and have had an encounter with a massive satellite (with stellar mass $M_{\rm sat} > 10^{10}\,M_\odot$) that fell into the system 2 Gyr to 8 Gyr ago. We then examined recent snapshots of these systems for visual analogs of M31's giant stream and shells. The best match is subhalo ID 482155, which has a present-day dark halo mass of $2.2\times10^{12}\,M_\odot$ and a present-day stellar mass of $1.2\times10^{11}\,M_\odot$, and is in the process of accreting a large satellite (stellar mass $10^{10}\,M_\odot$) that experienced first infall 6.7 Gyr ago. As the merger is still underway, the dissipating satellite retains a compact core of stellar mass $1.8 \times 10^9\,M_\odot$ located ≈ 30 kpc from the center of the primary galaxy (see Figure 13, left panel); the median metallicity of all the particles from this massive satellite is nearly solar, with [Fe/H] $= -0.07$. The satellite is no longer star-forming, but underwent star formation as recently as 2.5 Gyr ago.
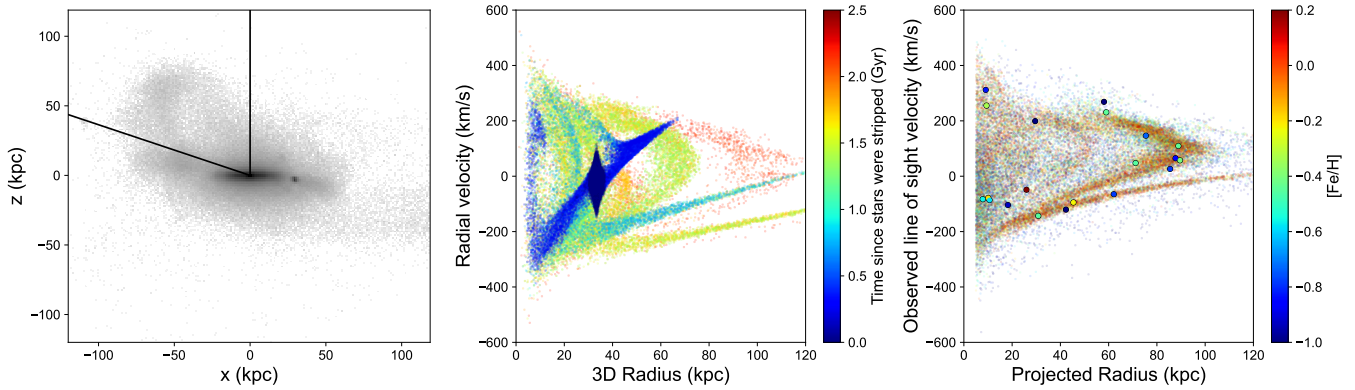
Figure 13. *Left:* Distribution of stellar particles in an M31 analog from the TNG-50 simulation. The system is matched in stellar mass to M31 and, like M31, has a prominent disk and large stellar halo, and experienced a recent encounter with a massive satellite (see the text for details). This particular analog shows a giant stream, numerous shells, and a compact core from the still-bound portion of the large accreted satellite at (x,z)≈(30,−2.5) kpc. *Center:* Particles from the merging satellite in 3D radius vs. radial velocity, color-coded by when they were stripped from the satellite. The distribution shows complex shell structure from a single large progenitor. *Right:* The distribution of accreted stellar particles (from all satellites) in the upper left wedge indicated in the left-hand panel, color-coded by metallicity. The larger solid points show 9 Gyr old to 12 Gyr old particles selected as possible (poor) proxies for globular clusters. In contrast to the globular cluster-like particles, which show relatively little kinematic substructure, the most metal rich stars display rich substructure, which results entirely from the recent large merger.

Fig. 13, which shows three different projections of this system, illustrates how the merger of a single progenitor galaxy can generate a stream, multiple shells, and nested wedges in phase space, similar to those seen in M31. The left panel shows the projected stellar mass density in greyscale with logarithmic scaling. The giant stream analog is clearly visible, as are shell structures and the compact core of the satellite (seen as the dark dot near x≈30, z≈−2.5). The center panel shows the overall kinematic structure of the stellar particles from the infalling satellite using the conventional (simulation) visualization of radial velocity (centered in the frame of the M31 analog) as a function of radius (in 3D rather than projected coordinates), in direct analogy to e.g., Fig. 10a from Fardal et al. (2007) or Pop et al. (2018). Particles are color-coded by the time when they were last part of the satellite's subhalo (prior to their tidal stripping), showing a clear progression in which the outermost tidal debris arises from earlier episodes of stripping (e.g., red and green points), and material near the still-bound core of the satellite is the most recently stripped (darker blue).

Finally, the right panel shows the line-of-sight velocity as a function of projected radius for stars in the angle wedge containing the giant stream analog, color-coded by metallicity. Although the contributions from all merged satellites are shown in this panel (not just that of the most recent merger as in the center panel), the earlier accreted satellites are all low mass and they merged long enough ago that they no longer contribute fine-scale kinematic structure (e.g., Beraldo e Silva et al. 2019). As a result, the most recent merger completely dominates the properties of the inner halo. Indeed, *all* of the substructure in this particular halo is metal rich, and arises from the stripping of this most massive satellite. We discuss this topic further in Section 6.

4.2. *Comparison to an N-Body Model*

The DESI observations can be compared in greater detail to simulations that have been customized to replicate the structure of M31. In order to understand whether a single encounter could account for much of kinematic structure observed in our data, we constructed a simple model informed by the results of previous studies. Previous modeling efforts in this field are described in greater detail in Section 6. We also publish all our good velocity measurements to aid future modeling attempts. It is our hope that these observations, insights from the cosmological models, and the comparisons presented here can inform future modelers in their efforts to reproduce more of the density and phase-space structure of M31's halo.

The model consists of a single component Plummer sphere (Plummer 1911) describing the progenitor of the GSS, which has a total mass of $\sim 2 \times 10^8 M_{\odot}$, a half-mass radius of 1 kpc, and is represented by 300,000 particles. The model does not distinguish between dark matter and stellar particles. M31 is represented by a static analytic potential that
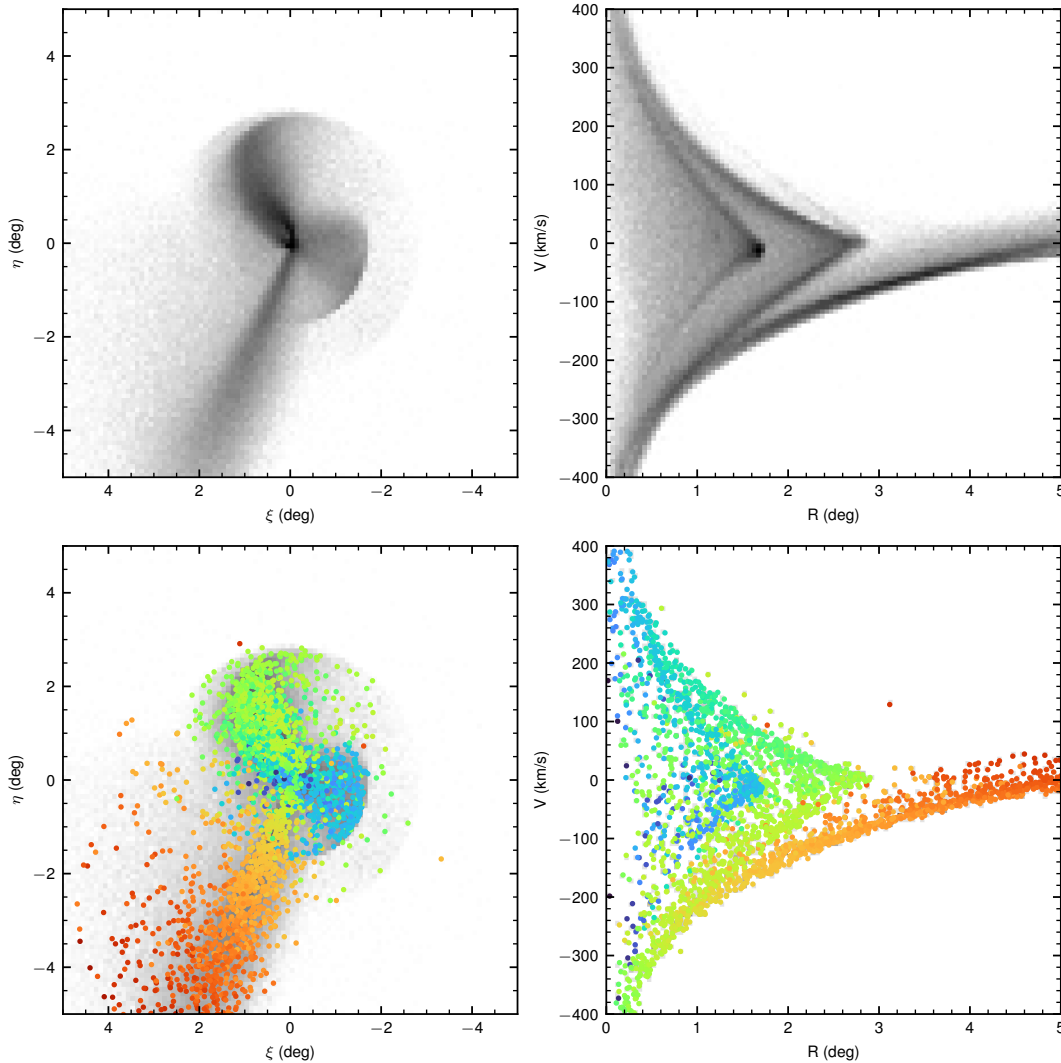
Figure 14. N-body model of the interaction between a progenitor and M31. Top panels show the spatial distribution (left) and projected position-velocity diagram (right) of particles 791 Myr after the start of the simulation (or 585 Myr after the pericentric passage of the GSS progenitor). In the bottom panels, a random 0.1% of the simulation particles are color-coded by their total energy (kinetic + potential) in the host potential. The progenitor is fully disrupted on the first encounter. As a result, the particles in the shell system are simply arranged by energy (Dong-Páez et al. 2022, as energy is directly related to orbital period), and the southern stream (orange points) and shells (green, cyan, and navy points) are cleanly separated in energy. The similarity to the M31 observations suggests that the observed structures could result from a single encounter, with the nested structures being subsequent wraps (i.e., different pericentric passages) of stars from the same progenitor.

consists of the disk, halo, and a bulge, where we use parameters similar to those employed in previous modeling efforts (Fardal et al. 2006; Kirihara et al. 2017). The bulge is a Hernquist bulge (Hernquist 1990) with a mass of $3.2 \times 10^{10} M_{\odot}$ and size $a = 0.5$ kpc. The dark matter halo is described by an NFW profile (Navarro et al. 1997) with $V_{\max} = 215 \, \mathrm{km \, s^{-1}}$ and a scale radius of $r = 7.63$ kpc. The disk is assumed to have an exponential scale length of $r_d = 5.4$ kpc, vertical height $h = 0.6$ kpc, and a total mass of $M_{\mathrm{disk}} = 3.7 \times 10^{10} M_{\odot}$; it is represented as a linear combination of 3 Miyamoto-Nagai disks, following the prescription of Smith et al. (2015). The progenitor falls in on an approximately radial orbit. Further details regarding the simulation are provided in Appendix B.

Figure 14 shows results 791 Myr after the start of the simulation. The initial pericentric passage of the GSS progenitor occurred at 188 Myr. While our simulation has not been tuned to match the data perfectly, it does provide a heuristic interpretive guide to the complex kinematic structures in M31. In the bottom panels of Figure 14, a random selection of 0.1% of particles are color-coded by their total energy (i.e., kinetic + potential), with the color range extending
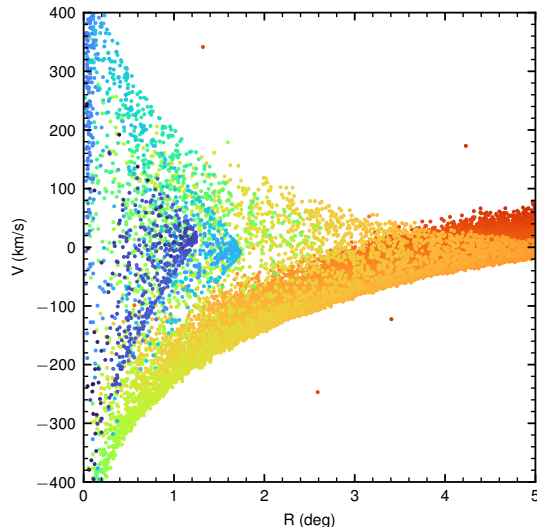
Figure 15. Velocity vs. projected distance of particles in the southeastern sector of the simulation at 770 Myr (a slightly earlier time than that shown in Figure 14). The navy coloured particles (those with the most negative energies) do not form a full chevron, only the bottom half of it, as the stars in this structure have not yet reached their apocenter. The resulting feature is reminiscent of feature 1bb in M31, despite not quite matching its range in projected distance.

from red representing particles with the least negative total energy, to blue representing the most negative (i.e., most tightly bound) particles.

Unlike the higher-mass merger in Section 4.1 that retains a bound remnant to the present day, this progenitor is fully disrupted on the first apocentric passage; thus the resulting set of shells can be understood as the debris from one disruption event, arranged according to energy (Dong-Páez et al. 2022). The GSS-like southern stream (orange-red points) and the nested shells (green, cyan, and navy points) are cleanly separated in energy. Specifically the stars with the least negative energy have not yet had a second pericentric passage after being stripped, while the particles with the most negative energies and therefore much shorter orbital period (the cyan points), have already had multiple pericentric passages after the initial stripping episode.

Comparing Figures 14 and 8, we see that the main part of the GSS (feature 1ab) is similar to the orange-red points in the simulation; and that the shells denoted by the structures 2a, 4b+5 and 1c+2b (i.e., the Northeast Shelf, Western Shelf, and Southeast Shelf) are similar to the simulation points shown in green, cyan, and navy, respectively, in Figure 14. Stars with the most negative energies (navy colored points), located in the southeastern sector of M31, are the stars from the leading part of the debris.

Figure 15 shows only the radial velocities of particles in the southeast sector, using the same energy color-mapping scheme as in Figure 14. Interestingly, the leading particles in position-velocity space do not occupy a full chevron, but instead primarily trace out a locus at negative velocities, because many of these stars have not yet experienced a turnaround at apocenter. The 1bb feature in M31 may have a similar origin. Similar to the situation shown in Figure 15, 1bb appears in the same sector as the GSS (equivalent to the orange points in the Figure), is blueshifted, and has no companion redshifted feature that would create a chevron-like pattern.

The results suggest that the multiple structures observed in M31 could arise from a single encounter, with the various nested structures produced by subsequent wraps (i.e., different pericentric passages) of stripped stars from the same progenitor. Importantly, in our simulation, the progenitor is fully disrupted in the encounter, so all of the shells that result are essentially a single set of stars wrapping around the galaxy. If the progenitor instead preserves some mass for a second pericentric encounter, as in the cosmological model discussed in Section 4.1, an additional set of shells would be created; these are unaccounted for in our current simulation. Simulating the shell system from a possible second pericentric encounter would be somewhat more challenging, as the dynamical friction of the progenitor likely would need to be taken into account. This second shell system is probably needed to explain some of the smaller chevrons observed in our data. Future observations that more densely sample the structures in the inner halo will provide a unique opportunity to constrain the mass and orbit of the progenitor.
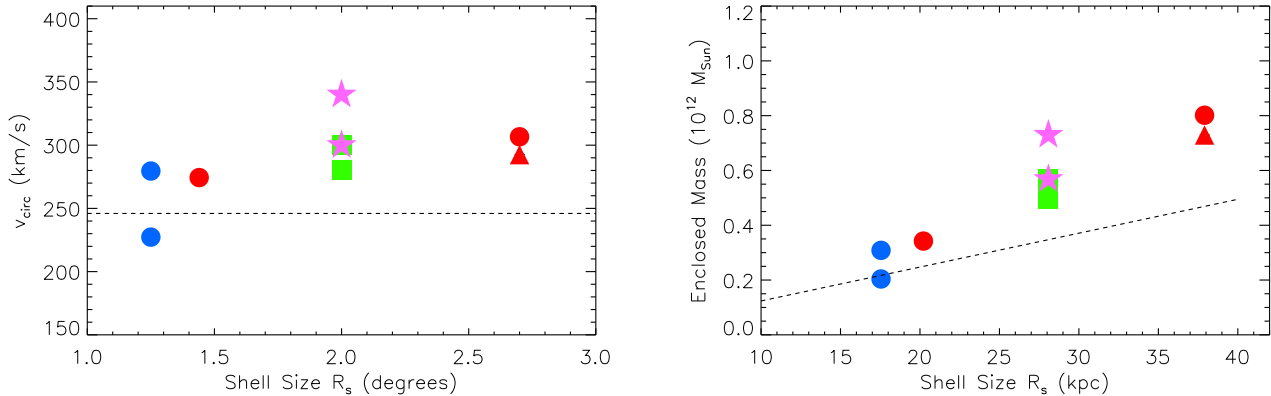
Figure 16. Circular velocities (left) and enclosed masses (right) inferred from the velocity gradients (dV_{los}/dr) of linear features in line-of-sight velocity and projected distance in Zone 1 (blue dots), 2 (red dots), 3(red triangles), 4(green squares), 5 (pink stars). Dashed lines show the typical circular velocity of the flat portion of the HI rotation curve of M31 (Chemin et al. 2009) and the corresponding enclosed mass for a flat rotation curve out to ~ 40 kpc.

5. CONSTRAINTS ON THE MASS OF M31

5.1. *Shell Kinematics*

The shell-shaped tidal signatures of galaxy mergers that we observe also offer the opportunity to measure the gravitational potential of the host galaxy, with nested shells probing the gravitational potential as a function of galactocentric distance (Merrifield & Kuijken 1998; Sanderson & Helmi 2013). Our current sample measures radial velocities for stars in multiple shells spanning a range of distances and thereby offers a rare opportunity to constrain the dynamical mass of the galaxy as a function of galactocentric distance using this technique.

As described by Merrifield & Kuijken (1998), for a shell oriented in the plane of the sky, the projected velocity of the shell has a distinctive triangular shape as a function of projected distance (a filled 'wedge' or empty 'chevron' shape), and the slope of the projected velocity near the outer edge of the shell can be used to infer the gravitational potential. That is, for a spherical shell of radius r_s with a projected velocity v_{los} that increases with decreasing projected distance R, the velocity gradient $dv_{los}/dR = -\Omega$, where Ω is the circular frequency at r_s. Sanderson & Helmi (2013) derived a related expression that includes the effect of the outward velocity of the shell (their eq. 23) and argued that the simpler Merrifield & Kuijken (1998) method will tend to overestimate the enclosed mass.

The multiple shell structures observed in M31 allow us to explore these ideas. To explore how well the simple Merrifield & Kuijken (1998) prescription recovers the expected gravitational potential of M31, we measured (by eye) the velocity gradient of the red- and blue-shifted edges of the wedges and chevrons seen in the Northeast Shell, the Western Shell, and in the region of the GSS. These features have approximate projected extents of $\sim 1.3°$ (Features 1cb/1cr and 2br), $\sim 2°$ (Features 2ar and 3ar), and $\sim 2.7°$ (Features 4bb/4br and 5b/5r), which correspond to projected distances of ~ 19 kpc, ~ 28 kpc and ~ 38 kpc.

The lines shown in the insets of Figures 6 and 7 show the regions used to estimate the velocity gradients. Slopes are better defined for features that are densely populated (e.g., 2ar). Feature crowding, the possibility that features overlap each other or are embedded in a distributed background halo, can make it difficult to define the slope of a feature (e.g., 2br resides within 2ar). Higher density spectroscopy of the M31 halo can potentially mitigate these challenges.

The measured slopes correspond to circular velocities of 230 km s^{-1} to 340 km s^{-1} at the shell radius (i.e., the apex of the wedge or chevron) and imply enclosed masses of $2 \times 10^{11} M_{\odot}$ to $8 \times 10^{11} M_{\odot}$ over this range of distances (Figure 16). The circular velocities are similar to, or larger than, the velocity of the H I rotation curve of M31 measured over the same range of radii (horizontal line in left panel of Figure 16). The rotation curve, which is roughly flat at ~ 250 km s^{-1} from 10 kpc to 40 kpc, implies an enclosed mass that is $4.7 \times 10^{11} M_{\odot}$ within 38 kpc (Chemin et al. 2009) and declines toward smaller radii as $1/r$ (dashed line, right panel).

In comparison, the circular velocity and enclosed mass derived from the properties of the smallest shell (radial extent $\sim 1.3°$) are close to the values inferred from the H I rotation curve at the same distance. The values for the larger

shells (radial extents of $2.0°$ and $2.7°$) are larger than the corresponding values from the H I rotation curve. These results are consistent with the findings of Sanderson & Helmi (2013), that the Merrifield & Kuijken (1998) prescription can correctly recover the enclosed mass in some cases, but that it often overestimates enclosed mass by a factor of 2 to 3. A similar result was reported by Escala et al. (2022) in their analysis of the kinematics of stars in a portion of the Northeast Shelf.

In summary, mass estimates from the observed velocity gradients of shells rely on the assumption of shells of stars oriented in the plane of the sky and do not account for complexities introduced by geometry, angular momentum, or the details of the interaction. Consequently, while the overall idea of using shells to estimate the mass of M31 is potentially useful, it is clear that more sophisticated modeling and more extensive spectroscopic samples will be necessary to reach an interesting level of accuracy.

5.2. *Kinematics of the GSS*

As a complementary approach, stellar streams like the GSS also probe the galactic potential and can plausibly be interpreted using a more detailed dynamical model that is driven by a few simple assumptions. The shells from a single pericentric passage represent a group of stars on a sequence of orbits ordered by energy (see a detailed exposition of shell formation in Dong-Páez et al. 2022). Stars with the most negative energies have the shortest orbital periods, while stars with less negative energies have longer orbital periods. Thus the shell system will have an energy gradient. Although the energy gradient makes the analysis of the shells more cumbersome, as we cannot rely on the constant energy assumption that approximately works for thin tidal streams (Koposov et al. 2010), we can still effectively use the assumption that the energy changes monotonically along the structure due to energy sorting in the shell. The strength of the energy gradient in the shell is itself limited by the total energy spread in it, which in turn is determined by the energy spread of stars at the pericentric passage of the progenitor i.e $\delta E \sim \frac{1}{2}(V_{\mathrm{peri}}+\sigma)^2 - (V_{\mathrm{peri}}-\sigma)^2 = V_{\mathrm{peri}}\sigma$, where σ is the velocity dispersion of the progenitor and V_{peri} is the velocity of the progenitor at the pericenter (see Dong-Páez et al. 2022, for more details). It turns out that these basic principles, together with a few assumptions about the GSS geometry, can help us model the radial velocity vs. distance behavior observed in the GSS and constrain the M31 gravitational potential.

To define the model we begin by defining a coordinate system x, y, z in which the z-direction is oriented along the line connecting the Sun and M31 pointing away from the Sun, the x-direction is aligned with the East, and the y-direction points North. Projected on the sky, the GSS forms an essentially linear structure, with position angle $\phi_{GSS} \sim 155°$. We assume that the GSS is also a linear structure in 3D, defined by the unit vector $\hat{\mathbf{k}} = [k_x, k_y, k_z]$ and that the line defined by this vector intersects the projected center of M31 (i.e., $x, y = (0,0)$) at a (small) distance z_{off} from the center of M31. We then assume that stars in the GSS move along this vector $\hat{\mathbf{k}}$. Thus the GSS stars are assumed to be on nearly radial orbits.

As discussed earlier, we expect an energy gradient along the GSS and therefore we assume that the total energy (potential and kinetic) of stars in the GSS can be approximated by a linear gradient along the stream (see, e.g., Appendix B and Figure 22), i.e., $E(R) = E_0 + \frac{dE}{dR}(R - R_0)$ where R is a projected distance along the stream and E_0 is the energy at R_0, the projected distance at the same point (i.e., the middle of the stream). We assume that the energy gradient is positive and limited by the maximum range of energies along the stream δE_{max} $0 < \frac{dE}{dR}(R_2 - R_1) < \delta E_{\mathrm{max}}$, where R_1 and R_2 are the projected distances that limit the observed portion of the GSS. The reason for the assumption of the positive energy gradient is that this is exactly what we expect for the trailing part of the shell. The GSS shell stars are currently falling back to M31 (from the first pericentric encounter of the GSS progenitor) and the most distant stars have the least negative energies (and therefore longest orbital periods). See for example the bottom left panel of Figure 14 showing the positive energy gradient in the GSS.

The adopted upper bound on the energy spread is $\delta E_{\mathrm{max}} = 30 \times 500$ $(\mathrm{km\,s^{-1}})^2$, the energy spread resulting from a progenitor with an initial pericentric velocity of 500 $\mathrm{km\,s^{-1}}$ and velocity dispersion of 30 $\mathrm{km\,s^{-1}}$. Because the GSS is only the very end of the shell system in M31, and the middle and leading part of the shell system are likely responsible for the Northeast Shelf and Western Shelf respectively, we expect that the actual energy spread for stars in the GSS is much smaller than δE_{max}. The final assumption is that energies $E(R)$ are always negative along the stream, i.e., all the GSS stars are bound.

While we make several assumptions here (e.g., that the energy gradient is linear as a function of projected radius and that the stars within the GSS are moving on primarily radial orbits), we have verified that in the fiducial N-body

model of the disruption of the GSS progenitor presented in Section 4.2 and Appendix B that these assumptions are satisfied.

The geometric assumptions that the stream is linear and the stars move along it tell us that the 3D velocity should be changing as a function of projected distance R along the stream as

$$\mathbf{V}(R) = a(R)\hat{\mathbf{k}} \tag{2}$$

where $a(R)$ is an unknown function. Since the (line-of-sight) radial velocity is simply a projection of the 3D velocity along the z-axis,

$$V_{\mathrm{los}}(R) = a(R)k_z. \tag{3}$$

Under the assumption of a linear change of energy with radius along the GSS we can write

$$\frac{V^2(R)}{2} + \Phi(\mathbf{X}) = E_0 + (R - R_0)\frac{dE}{dR}, \tag{4}$$

where $\mathbf{X}$ is the 3D position along the stream

$$\mathbf{X} = (Rk_x,\ Rk_y,\ z_{\mathrm{off}} + Rk_z/\sqrt{1 - k_z^2}) \tag{5}$$

corresponding to a projected distance R along the stream and $\Phi(\mathbf{X})$ is the gravitational potential.

Combining Eq. 2 and 4 allows us to write an expression for $a(R)$:

$$a(R) = \sqrt{2\left(E_0 + \left[\frac{dE}{dR}(R - R_0)\right] - \Phi(\mathbf{X})\right)} \tag{6}$$

which gives us the expression for $V_{\mathrm{los}}(R)$ through Eq. 3 if we know E_0, $\frac{dE}{dR}$, $\hat{\mathbf{k}}$, and the gravitational potential. Essentially we now can write the likelihood for the radial velocity as a function of projected distance $P(V_{\mathrm{los}}|R, \hat{\mathbf{k}}, \Phi(R), E_0, \frac{dE}{dR})$ that we can fit to the velocity track of the GSS.

While the number of parameters is potentially quite large, we can adopt informative priors on many of them. We have previously described our constraints on energy and energy gradients E_0 and $\frac{dE}{dR}$. Furthermore, the GSS orientation parametrized by $\hat{\mathbf{k}}$ is well constrained by its projected orientation on the sky and the measured distance gradient of $20\,\mathrm{kpc\,deg^{-1}}$ along its $6°$ extent (Conn et al. 2016). We therefore adopt a uniform prior for the distance gradient to be between $15\,\mathrm{kpc\,deg^{-1}}$ and $25\,\mathrm{kpc\,deg^{-1}}$. A simple algebraic equation for the distance gradient provides a prior on k_z. For the gravitational potential we adopt a typical bulge/disk/halo decomposition with the bulge and disk models to be Hernquist and Miyamoto-Nagai models respectively with fixed parameters from Kirihara et al. (2017). We assume a disk inclination angle of $77°$ and a position angle of the major axis of $38°$. The dark matter halo component is modeled as an NFW (Navarro et al. 1997), where the halo mass M_{halo} and scale length r_s are to be determined. We adopt a log-uniform prior on the mass $10^8\,M_\odot < M_{\mathrm{halo}} < 10^{14}\,M_\odot$ and scale length $1\,\mathrm{kpc} < r_s < 100\,\mathrm{kpc}$. This completes the definition of our model likelihood and parameter priors.

For the locus of the GSS, we used the result of the two-component fit described in Section 3.2. The radial velocity measurements in 9 positions together with their uncertainties along the GSS were then fit by the $V(R)$ model as described in Eq. 2 and 6. The posterior was sampled with the `dynesty` nested sampler. The model had 6 parameters in total: the halo mass and scale length, the distance gradient, energy and its gradient E_0 and dE/dR, and the offset of the stream from pointing directly at the M31 center z_{off}. The posterior on these parameters is shown in Figure 17. To avoid the typical mass-size degeneracy, we show the posterior for the mass inside 125 kpc rather than the total halo mass. Multiple parameters are unconstrained (such as the distance gradient, where we are purely driven by the prior), which is not very surprising given the limited data available. We also note that the offset of the GSS from pointing directly at the M31 center (z_{off}) is consistent with zero, confirming that the orbits are very close to radial. We also see that the energy gradient prefers significantly lower values than our threshold, which is reasonable, given that we expect the GSS to be only a small (trailing) part of the shell.

We find the halo mass within 125 kpc to be $\log_{10} M_{\mathrm{NFW}}(< 125\,\mathrm{kpc})/M_\odot = 11.80^{+0.12}_{-0.10}$ or if we include the disk and the bulge $\log_{10} M_{\mathrm{total}}(< 125\,\mathrm{kpc})/M_\odot = 11.84^{+0.12}_{-0.10}$. As the method we employed makes significant assumptions, we have also applied exactly the same fitting procedure to the sample of stars from the simulation presented in Section 4.2 and obtained the halo mass with the bias of $\log_{10} M_{\mathrm{halo,fit}} - \log_{10} M_{\mathrm{halo,true}} \approx 0.1$ which is within our uncertainty.
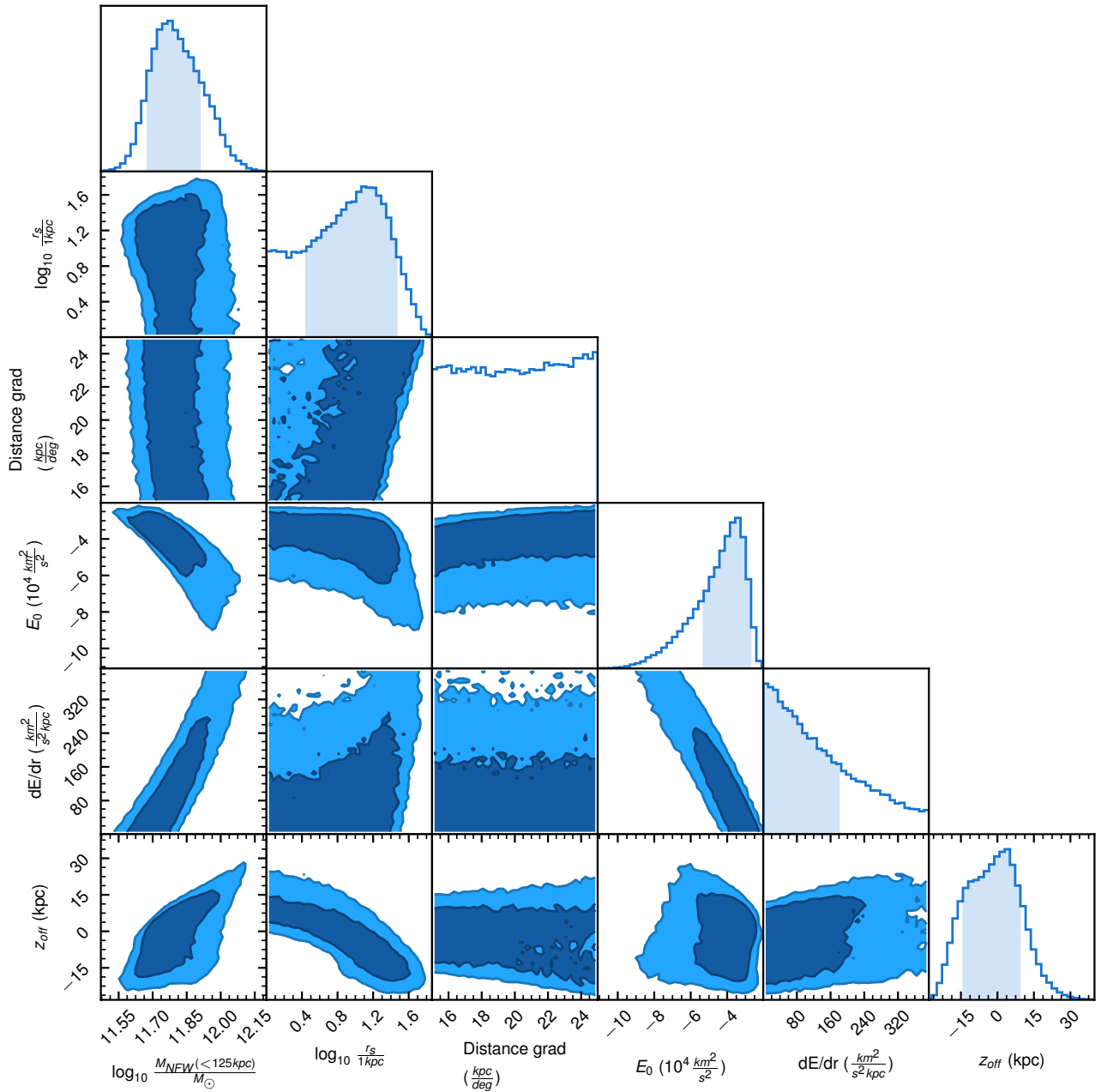
Figure 17. Corner plot showing the posterior probability distributions resulting from the simple dynamical mass estimates derived by modeling the GSS as a linear structure with a linear energy gradient along its extent (see the text in § 5.2 for details).

Our mass estimate of $\log_{10} M_{\mathrm{NFW}}(< 125\,\mathrm{kpc})/M_\odot = 11.80^{+0.12}_{-0.10}$ is consistent with estimates from the literature of the enclosed mass at this distance (e.g., graphical summary in Kafle et al. 2018). In particular, our result is similar to that of Ibata et al. (2004), who carried out the first kinematic study of the GSS, measuring the velocities of 184 stream stars and using the velocity gradient along the stream to estimate a halo mass of $M_{125} = 7.6 \pm 1.2 \times 10^{11} M_\odot$ for a logarithmic halo and $M_{125} = 6.4 \pm 1.3 \times 10^{11} M_\odot$ for an NFW halo.

6. DISCUSSION

As described in the previous sections, DESI spectroscopy reveals intricate, coherent spatial-velocity structure in the inner halo of M31, including nested chevrons and wedge-shaped structures (Figures 6, 7), with a spatial and kinematic clarity never-before observed in an extragalactic source (Section 3). The DESI results affirm earlier "pencil beam" spectroscopy carried out in restricted portions of the inner halo. The observed structures are consistent with the expected kinematic signatures of shells and streams produced in galaxy mergers (§ 4.1, 4.2) and suggest that most, if not all, of the structure observed in M31 arises from a single merger event (§ 4.2). We illustrated how the kinematics of the structure induced by the merger—the shells and the GSS—can dynamically probe the mass distribution of M31 as a function of galactocentric distance (§ 5.1, 5.2). In this section we situate our results in the context of prior work and turn to the question of the nature of the progenitor that produced the observed substructure.

6.1. *Comparison to Previous M31 Merger Models*

Many previous studies have explored and advanced a picture in which much of the inner halo substructures of M31 are tidal debris from a single companion galaxy that encountered M31 on a nearly radial orbit (e.g., Ibata et al. 2004; Font et al. 2006; Fardal et al. 2006, 2007, 2008, 2012, 2013; Mori & Rich 2008; Sadoun et al. 2014; Kirihara et al. 2017; Milošević et al. 2022). These simulations have explored a wide range of parameters, and found that a wide range of progenitor stellar masses can reproduce the observed morphologies. Several studies have suggested that the visible debris is the result of a minor merger ($\sim$ 1:10 to 1:5), with the stellar mass of the companion in the range 1–$5\times10^9\,M_\odot$ (e.g., Fardal et al. 2013; Kirihara et al. 2017; Sadoun et al. 2014). In contrast, a few studies have suggested that the observational data suggest a major merger (i.e., $\sim$1:4–5) with a progenitor of stellar mass $> 10^{10}\,M_\odot$ (D'Souza & Bell 2018; Hammer et al. 2018; Bhattacharya et al. 2019). D'Souza & Bell (2018) advocated for a major merger based on the mass, metallicity, and star formation history (SFH) of the halo. They also hypothesized that M32, M31's compact satellite, could be the core of the disrupting satellite based on metallicity and star-formation history. M32 is located within the debris field close to where the GSS meets the M31 disk and has a very different velocity from the GSS, indicating that M32 would be at a very different phase of its orbit than the GSS material. Other studies predict that the progenitor lies elsewhere in the debris or may be completely disrupted. Hammer et al. (2018) additionally note that the 2–4 Gy-old star-formation episode and significant thick disk of M31 might both be the product of the interaction with a massive progenitor. Recent studies of M31 halo stars also report higher [Fe/H], a stronger [Fe/H] gradient, higher mean [α/Fe], and a larger [α/Fe] spread than observed in the Milky Way halo, suggesting that much of the M31 inner halo region and GSS may result from the assimilation of a fairly massive galaxy with a complex star-formation history (Gilbert et al. 2019; Escala et al. 2020a,b, 2021). This major-merger picture is also consistent with the observed steep age-velocity dispersion relation, large asymmetric drift, and other chemical signatures observed in the disk populations (Dorman et al. 2015; Bhattacharya et al. 2019; Arnaboldi et al. 2022).

Although the morphology of the debris appears to be insensitive to the mass of the progenitor (e.g., Hammer et al. 2018; Boldrini et al. 2021), the simulations reveal that it is sensitive to the orbital parameters of the encounter. Dynamical models that attempt to account for both the observed spatial distribution of the debris and the radial velocities available to date generally infer an initial pericentric passage within a few kpc of the center of M31 within the last 1–2 Gyr. In many of the models tailored to M31 (including our own from § 4.2), a companion galaxy plunges into M31 and its stars are pulled out on the far side of M31 to form the GSS following the first pericenter passage. The DESI observations do not detect any outward moving stars following the first pericentric passage, but they do detect the infalling stream of stars on their way back toward M31 after their first apocentric passage. The Northeast Shelf is produced as the second wrap of the orbit, and the Western Shelf constitutes the third wrap (Fardal et al. 2007, 2008, 2012, 2013). The Southeast Shelf, tentatively identified by Gilbert et al. (2007), may constitute the fourth wrap, the leading edge of the tidal debris. In the models of Fardal et al. (2013) and Kirihara et al. (2017), the core of the progenitor, if it has survived tidal disruption, is predicted to reside somewhere in the Northeast Shelf.

All of the models are successful in accounting for the general spatial morphology of the GSS, Northeast Shelf, and Western Shelf, as well as spectroscopic observations of the GSS and the Western Shelf available to date. The anticlockwise-rotating thick-disk model of Kirihara et al. (2017) better reproduces the edge-brightening observed on the eastern side of the GSS. In addition, some models (e.g., Milošević et al. 2022; Kirihara et al. 2017) also reproduce the metallicity variations observed in the GSS by Conn et al. (2016). Previous studies have compared their simulations with the velocities of either small numbers of PNe or larger numbers of RGB stars measured with Keck/DEIMOS in pencil beams located at a few radial positions within the inner halo (e.g., Fardal et al. 2007, 2013).

In particular, the model of Fardal et al. (2007), which was designed to replicate the observed substructure in photometric imaging studies of M31, is remarkable in capturing many of the observed features in the DESI radial velocity data. Since these model data were not available to us, we made simple comparisons of our observations plotted in the same way as the simulations, comparisons which corroborate many of the features predicted by Fardal et al. (2007). In comparing to earlier data, Fardal et al. (2007) showed how 11 PNe from Merrett et al. (2003, 2006) (which have kinematics classified as "stream" or "stream?") trace out the predicted locus of the blue-shifted edge of the Northeast Shelf, the large wedge in the position-velocity diagram at $-500 \lesssim V_{los} \lesssim -100$ km s^{-1} (see the right panel of Figure 3 of Fardal et al. (2007)). The DESI observations overlap with the PNe and chart out the wedge-like structure more completely and in greater detail on both the red- and blue-shifted edges and show that the structure extends to slightly larger projected distances than predicted by the Fardal et al. (2007) model (see also Figure 11).

Earlier studies also compared the positions of PNe from Merrett et al. (2003, 2006) and stars along the minor axis of M31 with the simulation predictions in the Western Shelf region (e.g., Fardal et al. 2007, 2013). The DESI data clearly trace out the shell-like nature of the kinematic structure in the Western Shelf over a large spatial extent, also showing only minor deviations, especially at projected radii $> 1.5°$.

While much of the structure observed with DESI is roughly consistent with the dynamical models published to date, some features remain unaccounted for. Notably, the blueshifted feature 1bb in Zone 1 is not reproduced, as has been previously noted (e.g., van der Marel et al. 2012). The DESI data also reveal new features. For example, in the Zone 2 region of the Northeast Shelf, the DESI data show a second, smaller wedge extending out to 1.3° and highlighted in Figure 6, which may be the continuation of features 1cb and 1cr into Zone 2. These Zone 1 features were previously identified by Gilbert et al. (2007) from pencil-beam spectroscopy along the southeast minor axis of M31. Associated with the Southeast Shelf, the Zone 1 and Zone 2 features may correspond to the fourth wrap predicted by the model of Fardal et al. (2013). In contrast, the compact chevron in Zone 1 that is bounded by $|V_{los}| \lesssim 150$ km s^{-1} does appear to be present in one simulation shown in Fardal et al. (2013). Their Figure 6 shows a compact component in Zone 1 that extends to a similar distance from M31 as the observed structure. In the model, the component arises from Northeast Shelf stars on the near side of M31 that overlap the GSS. Finally, the 3br feature in Zone 3 is also not present in the models.

These initial DESI results represent a significant advance by covering large areas more uniformly and revealing the kinematic structures in unprecedented clarity. These data inform future modeling efforts to understand the merger history responsible for the complex inner halo substructure of M31.

6.2. *Clues to Nature of the Progenitor*

As simulations have demonstrated that the morphology of the debris is relatively insensitive to the mass of the progenitor (e.g., Boldrini et al. 2021), other information is needed to constrain the nature of the progenitor. Previous studies have attempted to infer the nature of the progenitor using the metallicity (a wide range in metallicity, reaching more than 1/3 solar in the inner parts of the debris; Gilbert et al. 2014; Ibata et al. 2014) and star formation history (showing star formation until around 2-3 Gyr ago; Brown et al. 2006) implied by measurements of the inner stellar halo and substructures (D'Souza & Bell 2018). [Fe/H] and [α/Fe] measurements of individual halo stars have also been used to argue that much of the M31 inner halo region and the GSS in particular may result from the assimilation of a fairly massive galaxy with a complex star-formation history (Gilbert et al. 2019; Escala et al. 2020a,b, 2021). Here we contribute to this topic by commenting on (1) the metallicity of the stellar debris, (2) the number of dwarf galaxies and globular clusters potentially associated with the progenitor, and (3) whether there is any evidence for a surviving progenitor galaxy.

Since our target selection introduces a bias towards metal-rich RGB stars (§ 3.4), we cannot use the current DESI data to reliably measure the metallicity distribution of the accreted stars. However, we do find that significant numbers of metal rich stars are present across all regions surveyed, suggesting that the progenitor responsible for these structures is relatively high mass, high enough to have stars up to solar metallicity. Future DESI observations that target stars more metal poor than those studied here can better characterize the metallicity distribution of the progenitor.

Given that the progenitor was probably massive (i.e., $> 10^9 M_\odot$), it is possible that the merger event will have delivered star clusters and dwarf galaxies to M31. Figures 18 and 19 show the distribution of dwarf galaxies and old (> 2 Gyr) star clusters with measured ages and velocities from the literature compared to the stars measured with DESI. The dwarf galaxy measurements are from the compilation of McConnachie (2012) and the star cluster

measurements are primarily from LAMOST spectroscopic surveys (Chen et al. 2015, 2016; Wang et al. 2021) and the Hectospec surveys (e.g., Caldwell & Romanowsky 2016).
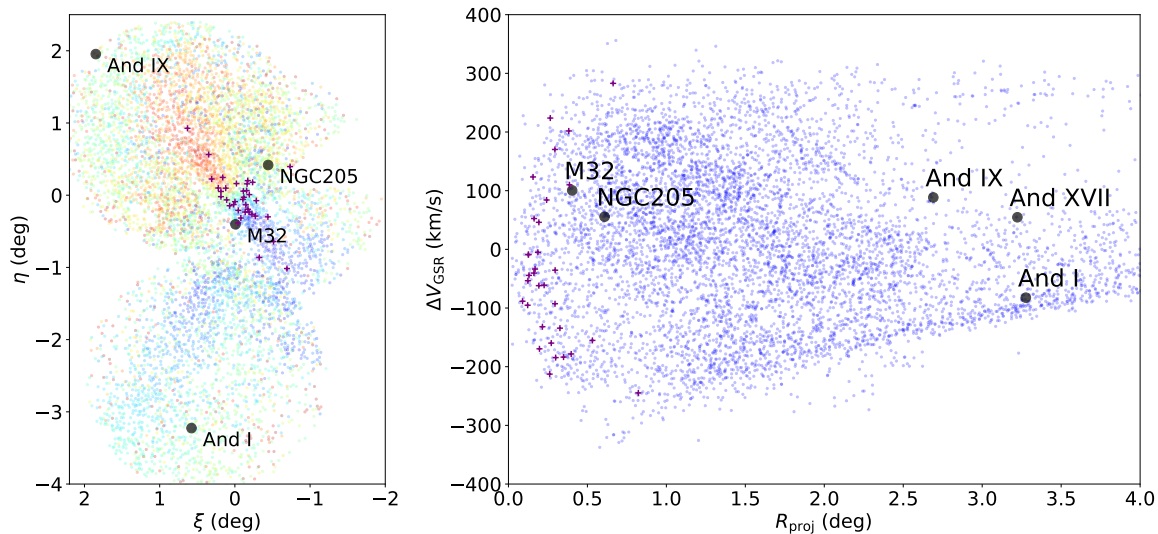
Figure 18. The distribution of the closest dwarf galaxy companions to M31 on the position-velocity diagram resulting from the DESI observations. The positions and velocities of the dwarf galaxies are taken from the updated (2021 January) version of the compilation by McConnachie (2012). The purple plus signs represent emission line sources (i.e., a combination of HII regions and PNe) among the DESI targets.

The dwarf galaxy Andromeda I closely overlaps the GSS (Figure 18), as does at least one globular cluster at a distance of 3.5° (Figure 19), suggesting a possible physical association. The association of this globular cluster, LAMOST-1, with the GSS has been previously noted by Chen et al. (2015, 2016). LAMOST-1's metallicity ([Fe/H] =−0.4) and age (9.2 Gyr) are consistent with an association with the GSS progenitor. In Zones 2 through Zone 5, the distribution of globular clusters is similar to that of the stars in the inner halo. In particular, they populate the interior of the wedge in Zone 2 ($\theta = 130°$–$230°$) and the small wedge in Zones 3+4 ($\theta = 230°$–$315°$). Thus, interestingly, many of the clusters are potentially associated with the wedge structures within 2° of M31, while relatively few clusters overlap the GSS.

These results are roughly consistent with expectations from merger simulations. For example, considering the representative galaxy merger in the Illustris TNG-50 simulation (Fig. 13, larger solid points in the right-hand panel), one could very crudely subsample particles from the dominant merger companion that are 'old' (9-12 Gyr ago), mirroring the epoch of globular cluster formation in the Milky Way. These early-forming star particles tend to be more centrally concentrated and kinematically hotter than the bulk of the progenitor stars, and are not as clearly confined to kinematically cold substructures. While more detailed model predictions that follow globular cluster formation in galaxies and their expected distribution among the tidal debris are clearly needed to fully interpret the observations and obtain robust constraints on the nature of the progenitor, this exercise tentatively suggests that it may be challenging to accurately attribute globular clusters to the progenitor solely on the basis of their clustering into kinematic substructures. Future studies might explore the metallicities and orbits of M31 globular clusters to infer their association with the progenitor galaxy (e.g., Mackey et al. 2019a,b).

Finally, with its ability to map out stellar velocity structure over large areas, DESI offers the opportunity to locate the remnant core of the progenitor galaxy. Fardal et al. (2013) predicted that if the progenitor survives, stars from the core of the progenitor will populate a fairly compact structure in phase space located at a projected distance of $1° \lesssim R_{proj} \lesssim 2°$ and a line-of-sight velocity of ≈ 0 to -200 km s^{-1} (i.e., in Zone 2 and blue-shifted relative to the M31 systemic velocity). Kirihara et al. (2017) predicted that the stripped bulge of the progenitor lies in the eastern shell and in front of the disk of M31, compact in phase space and at a location of $(\xi, \eta, V_{los}) \approx (1.1°, 0.5°, -200$ km s$^{-1})$.

No such structures are detected in the DESI data, although this may yet be due to the sparseness of our current sampling. We do find that the velocities in Zone 2 show a preferential *redshift*, rather than the blueshift predicted by Fardal et al. (2013), and they show evidence of multiple shells rather than a component that is compact in phase space.
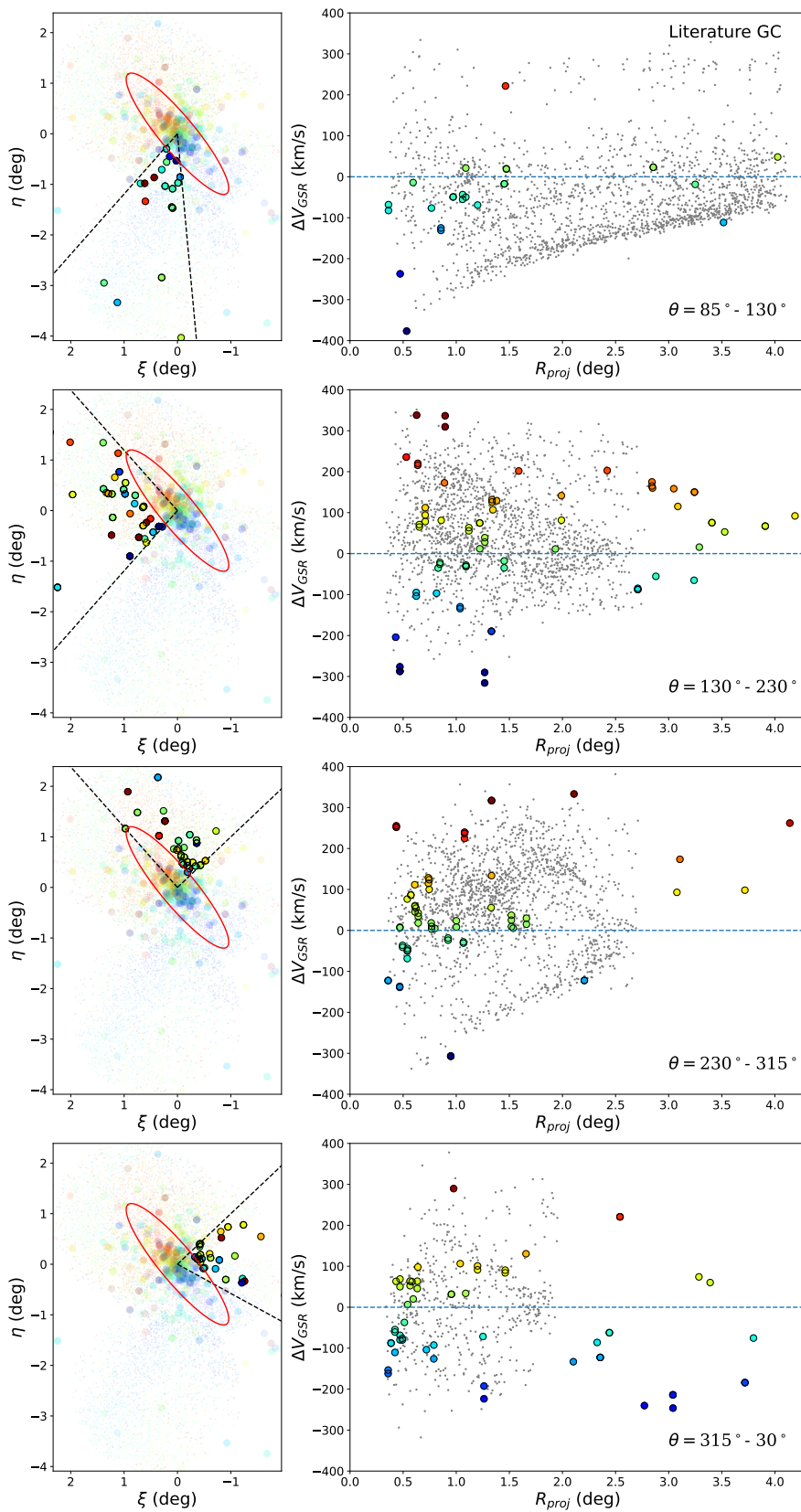
Figure 19. The distribution of old star clusters with ages > 2 Gyr (large colored circles) overlaid on M31 stars (smaller points).

Future DESI observations could place stronger constraints on (or possibly identify) a surviving progenitor galaxy. More densely sampled spectroscopy will permit quantitative assessment of the possibility that M32 (D'Souza & Bell 2018) or another existing galaxy is the progenitor, or perhaps identify a remnant or disrupting core in the inner halo of M31.

M31 and the Milky Way show a remarkable parallel, in that the inner halos of both galaxies are dominated by debris from a single accretion event. The Milky Way's inner halo is dominated by the *Gaia*-Sausage-Enceladus structure, a radial accretion event of mass $> 10^{10}$ $M_\odot$ nearly 8-11 Gyr ago (e.g., Belokurov et al. 2018; Helmi et al. 2018). The inner halo of M31 is also dominated by the single radial accretion event that produced the GSS and the intricate kinematic structures studied here, but which began only 1-2 Gyr ago. If the M31 shell system progenitor is indeed as massive as suggested based on its total stellar luminosity and stellar metallicities, M31 may provide a glimpse of what the Milky Way looked like several Gyr ago. Future spectroscopic surveys of the M31 inner halo will be able to explore this exciting possibility in greater detail.

7. SUMMARY AND CONCLUSIONS

We have obtained spectra, in three DESI pointings, of 11,554 targets in the direction of M31. Using these observations, we have measured accurate radial velocities of 10,414 stellar sources, of which 7,527 are members of the M31 system. These include radial velocities for 43 HII regions and Planetary Nebulae, and 136 M31 clusters. We have also identified 184 QSOs and 683 galaxies behind M31, which can provide unique probes of the gas associated with the GSS progenitor and other circumgalactic and interstellar material associated with M31.

While most of the earlier spectroscopy of individual stars in M31 had been carried out with 6.5-m to 10-m class telescopes, a few hours of spectroscopy with DESI has added significantly to our knowledge of the stellar kinematics of the M31 halo. These data represent a >3-fold increase in the number of known M31 stars in the region outside the M31 disk, and provide a much more uniform sampling of the inner halo than any previous spectroscopic study. The rapid advance is due to (1) DESI's wide field of view, high multiplex, and high observing efficiency; (2) the use of selection criteria that efficiently select M31 stars with limited contribution from foreground Milky Way stars; (3) the strong molecular bands in the late-type spectra of the M31 sample, which enables reasonable radial velocity accuracy (< 10 km s^{-1}) on faint stars ($z = 21.5$ AB mag); and (4) the good match of DESI's fiber density to the stellar target density of M31.

The DESI spectra reveal intricate coherent kinematic structure in the positions and velocities of individual stars in the inner halo of M31: streams, wedges, and chevrons that provide evidence of a recent merger, i.e., a galactic migration event. While hints of these structures have been glimpsed in earlier spectroscopic studies of M31, this is the first time wedges and chevrons have been *mapped* with such detail and clarity in a galaxy beyond the Milky Way. We find evidence for multiple coherent structures in the vicinity of the GSS and clear kinematic evidence for shell structures in the Western Shelf and Northeast Shelf regions. In particular, we identify 750 stars in the largest kinematic component (feature 1ab) of the GSS and measure a narrow velocity dispersion of 10.80 ± 0.75 km s^{-1}. The DESI data also reveal new structures not predicted by existing merger simulations. The kinematic structures seen in the stellar distribution of M31 halo stars are echoed in the position-velocity distribution of known M31 PNe.

Dynamical models from the literature that were constructed to explain the spatial morphology of the GSS and other inner halo features, as well as the models presented here, predict position-velocity structures that are remarkably similar to those observed. The results suggest that much of the substructure in the inner halo of M31 is produced by a single merger event with a companion galaxy a few Gyr ago. Taken together, the richness of the observed structure demonstrates that large spectroscopic samples can place valuable constraints on the recent merger history of M31 and that such samples are within the grasp of the Mayall/DESI system.

We find significant numbers of metal-rich stars across all of the detected substructures, suggesting that the progenitor galaxy (or galaxies) had an extended star formation history, one perhaps more representative of more massive galaxies. Known populations of stellar clusters in the halo of M31 appear to be more closely associated with the inner wedge structures (within 2° of M31) than the spatially extended GSS. The difference seems plausible if the clusters are predominantly older systems that originated in a kinematically hotter component in the progenitor galaxy.

The shell structures and the GSS also offer an opportunity to constrain the gravitational potential of M31 as a function of galactocentric distance. Using the simple prescription of Merrifield & Kuijken (1998), we obtained from the velocity gradients of the nested shell structures galaxy mass estimates ranging from $2 \times 10^{11} M_\odot$ to $8 \times 10^{11} M_\odot$ at projected distances between 17 and 38 kpc. These values exceed the enclosed mass estimates inferred from the H I rotation curve at distances of ~ 20 kpc to ~ 40 kpc, but nevertheless are within a factor of 2 of those values. A more

detailed dynamical model fit to the GSS velocities implies a dark matter mass of $6.0^{+2.1}_{-1.2} \times 10^{11} M_\odot$ within 125 kpc, in good agreement with estimates from the literature (e.g., Ibata et al. 2004).

M31 is remarkably similar to the Milky Way in that the inner halos of both galaxies are dominated by stars from a single accretion event. Indeed, a recent study of the kinematics of Milky Way stars near the Sun reports chevron-shaped kinematic substructures (Belokurov et al. 2022) that are reminiscent of those reported here. If the progenitor of the M31 shell system studied here is $\gtrsim 10^{10} M_\odot$, M31 may provide a close analog to what our own galaxy looked like several Gyr ago. More extensive DESI studies of M31 can explore this possibility by: (1) better characterizing kinematic substructures (shells, etc.) with higher sampling density; (2) extending our study of the metal-rich halo population to a characterization of the metal-poor population; (3) identifying the dwarf galaxies and globular clusters potentially associated with the progenitor; and (4) searching for evidence for a surviving progenitor galaxy.

Although here we identified shells by eye—which was appropriate given the limited data available—with higher-density sampling, we can measure the shells more accurately. By combining these more precise measurements with a detailed dynamical model customized to M31, we can place better constraints on the orbit of the progenitor and the mass and shape of the gravitational potential of M31. Characterizing the metal-poor population will allow us to better determine the metallicity of the progenitor and constrain its star formation history and total mass, as well as explore the more virialized (dynamically older) halo of M31. Extending over a large fraction of the galaxy's volume, the delicate chevrons we observe are also sensitive to the gravitational perturbations from substructure within the M31 halo, such as satellites and dark matter subhaloes. More refined mapping of the chevrons may be able to provide constraints on the number of such substructures. Finally, future work can also examine the structure and kinematics of the disk and the nature of the circumgalactic and interstellar media probed by the background QSOs and galaxies.

The observations presented here, obtained in just three DESI pointings with effective exposure times of ≤ 90 min, demonstrate the remarkable ability of DESI, on the Mayall 4-m telescope, to efficiently map out the large-scale kinematic structure of M31. Given DESI's efficiency, we can extend these studies to a larger volume and probe the outer halo of M31 and its interaction with its galactic neighbors (M33 and others). Photometric imaging studies of this region show streams and other structures. A future targeted survey could cover a significant fraction of M31's stellar halo with about 25 tiles. Such a survey would potentially increase the number of M31 halo stars by over an order of magnitude and reveal its structure and immigration history in unprecedented detail.

REFERENCES

Alexander, D. M., Davis, T. M., Chaussidon, E., et al. 2022, arXiv e-prints, arXiv:2208.08517. https://arxiv.org/abs/2208.08517

Arnaboldi, M., Bhattacharya, S., Gerhard, O., et al. 2022, A&A, 666, A109, doi: 10.1051/0004-6361/202244258

Astropy Collaboration, Robitaille, T. P., Tollerud, E. J., et al. 2013, A&A, 558, A33, doi: 10.1051/0004-6361/201322068

Astropy Collaboration, Price-Whelan, A. M., Sipőcz, B. M., et al. 2018, AJ, 156, 123, doi: 10.3847/1538-3881/aabc4f

Bailey, S. 2012, PASP, 124, 1015, doi: 10.1086/668105

Bailey, S. 2022, in preparation

Barmby, P., Ashby, M. L. N., Bianchi, L., et al. 2006, ApJL, 650, L45, doi: 10.1086/508626

Beaumont, C., Goodman, A., & Greenfield, P. 2015, in Astronomical Society of the Pacific Conference Series, Vol. 495, Astronomical Data Analysis Software an Systems XXIV (ADASS XXIV), ed. A. R. Taylor & E. Rosolowsky, 101

Bell, E. F., Zucker, D. B., Belokurov, V., et al. 2008, ApJ, 680, 295, doi: 10.1086/588032

Belokurov, V., Erkal, D., Evans, N. W., Koposov, S. E., & Deason, A. J. 2018, MNRAS, 478, 611, doi: 10.1093/mnras/sty982

Belokurov, V., Vasiliev, E., Deason, A. J., et al. 2022, arXiv e-prints, arXiv:2208.11135. https://arxiv.org/abs/2208.11135

Beraldo e Silva, L., de Siqueira Pedra, W., & Valluri, M. 2019, ApJ, 872, 20, doi: 10.3847/1538-4357/aaf8a7

Bhattacharya, S., Arnaboldi, M., Caldwell, N., et al. 2019, A&A, 631, A56, doi: 10.1051/0004-6361/201935898

Boldrini, P., Mohayaee, R., & Silk, J. 2021, ApJ, 919, 86, doi: 10.3847/1538-4357/ac12d3

Bonaca, A., Conroy, C., Cargile, P. A., et al. 2020, ApJL, 897, L18, doi: 10.3847/2041-8213/ab9caa

Breiman, L. 2001, Machine Learning, 45, 5, doi: 10.1023/A:1010933404324

Bressan, A., Marigo, P., Girardi, L., et al. 2012, MNRAS, 427, 127, doi: 10.1111/j.1365-2966.2012.21948.x

Brown, T. M., Smith, E., Ferguson, H. C., et al. 2006, ApJ, 652, 323, doi: 10.1086/508015

Bullock, J. S., & Johnston, K. V. 2005, ApJ, 635, 931, doi: 10.1086/497422

Bullock, J. S., Kravtsov, A. V., & Weinberg, D. H. 2001, ApJ, 548, 33, doi: 10.1086/318681

Caldwell, N., & Romanowsky, A. J. 2016, ApJ, 824, 42, doi: 10.3847/0004-637X/824/1/42

Chemin, L., Carignan, C., & Foster, T. 2009, ApJ, 705, 1395, doi: 10.1088/0004-637X/705/2/1395

Chen, B., Liu, X., Xiang, M., et al. 2016, AJ, 152, 45, doi: 10.3847/0004-6256/152/2/45

Chen, B.-Q., Liu, X.-W., Xiang, M.-S., et al. 2015, Research in Astronomy and Astrophysics, 15, 1392, doi: 10.1088/1674-4527/15/8/020

Conn, A. R., McMonigal, B., Bate, N. F., et al. 2016, MNRAS, 458, 3282, doi: 10.1093/mnras/stw513

Cooper, A. P., Cole, S., Frenk, C. S., et al. 2010, MNRAS, 406, 744, doi: 10.1111/j.1365-2966.2010.16740.x

Cooper, A. P., Koposov, S. E., Allende Prieto, C., et al. 2022, arXiv e-prints, arXiv:2208.08514. https://arxiv.org/abs/2208.08514

de Vaucouleurs, G., de Vaucouleurs, A., Corwin, Herold G., J., et al. 1991, Third Reference Catalogue of Bright Galaxies (Springer-Verlag: New York)

Dehnen, W. 2000, ApJL, 536, L39, doi: 10.1086/312724

—. 2014, gyrfalcON: N-body code, Astrophysics Source Code Library, record ascl:1402.031. http://ascl.net/1402.031

DESI Collaboration, Aghamousa, A., Aguilar, J., et al. 2016a, arXiv e-prints, arXiv:1611.00037. https://arxiv.org/abs/1611.00037

—. 2016b, arXiv e-prints, arXiv:1611.00036. https://arxiv.org/abs/1611.00036

DESI Collaboration, Abareshi, B., Aguilar, J., et al. 2022, arXiv e-prints, arXiv:2205.10939. https://arxiv.org/abs/2205.10939

Dey, A., Schlegel, D. J., Lang, D., et al. 2019, AJ, 157, 168, doi: 10.3847/1538-3881/ab089d

Dong-Páez, C. A., Vasiliev, E., & Evans, N. W. 2022, MNRAS, 510, 230, doi: 10.1093/mnras/stab3361

Dorman, C. E., Guhathakurta, P., Fardal, M. A., et al. 2012, ApJ, 752, 147, doi: 10.1088/0004-637X/752/2/147

Dorman, C. E., Guhathakurta, P., Seth, A. C., et al. 2015, ApJ, 803, 24, doi: 10.1088/0004-637X/803/1/24

D'Souza, R., & Bell, E. F. 2018, Nature Astronomy, 2, 737, doi: 10.1038/s41550-018-0533-x

—. 2021, MNRAS, 504, 5270, doi: 10.1093/mnras/stab1283

Escala, I., Gilbert, K. M., Fardal, M., et al. 2022, AJ, 164, 20, doi: 10.3847/1538-3881/ac7146

Escala, I., Gilbert, K. M., Kirby, E. N., et al. 2020a, ApJ, 889, 177, doi: 10.3847/1538-4357/ab6659

Escala, I., Gilbert, K. M., Wojno, J., Kirby, E. N., & Guhathakurta, P. 2021, AJ, 162, 45, doi: 10.3847/1538-3881/abfec4

Escala, I., Kirby, E. N., Gilbert, K. M., Cunningham, E. C., & Wojno, J. 2019, ApJ, 878, 42, doi: 10.3847/1538-4357/ab1eac

Escala, I., Kirby, E. N., Gilbert, K. M., et al. 2020b, ApJ, 902, 51, doi: 10.3847/1538-4357/abb474

Faber, S. M., Phillips, A. C., Kibrick, R. I., et al. 2003, in Society of Photo-Optical Instrumentation Engineers (SPIE) Conference Series, Vol. 4841, Instrument Design and Performance for Optical/Infrared Ground-based Telescopes, ed. M. Iye & A. F. M. Moorwood, 1657–1669, doi: 10.1117/12.460346

Fardal, M. A., Babul, A., Geehan, J. J., & Guhathakurta, P. 2006, MNRAS, 366, 1012, doi: 10.1111/j.1365-2966.2005.09864.x

Fardal, M. A., Babul, A., Guhathakurta, P., Gilbert, K. M., & Dodge, C. 2008, ApJL, 682, L33, doi: 10.1086/590386

Fardal, M. A., Guhathakurta, P., Babul, A., & McConnachie, A. W. 2007, MNRAS, 380, 15, doi: 10.1111/j.1365-2966.2007.11929.x

Fardal, M. A., Guhathakurta, P., Gilbert, K. M., et al. 2012, MNRAS, 423, 3134, doi: 10.1111/j.1365-2966.2012.21094.x

Fardal, M. A., Weinberg, M. D., Babul, A., et al. 2013, MNRAS, 434, 2779, doi: 10.1093/mnras/stt1121

Ferguson, A. M. N., & Mackey, A. D. 2016, in Astrophysics and Space Science Library, Vol. 420, Tidal Streams in the Local Group and Beyond, ed. H. J. Newberg & J. L. Carlin, 191, doi: 10.1007/978-3-319-19336-6_8

Font, A. S., Johnston, K. V., Guhathakurta, P., Majewski, S. R., & Rich, R. M. 2006, AJ, 131, 1436, doi: 10.1086/499564

Gaia Collaboration, Prusti, T., de Bruijne, J. H. J., et al. 2016a, A&A, 595, A1, doi: 10.1051/0004-6361/201629272

—. 2016b, A&A, 595, A1, doi: 10.1051/0004-6361/201629272

Gaia Collaboration, Brown, A. G. A., Vallenari, A., et al. 2018, A&A, 616, A1, doi: 10.1051/0004-6361/201833051

Gallart, C., Bernard, E. J., Brook, C. B., et al. 2019, Nature Astronomy, 3, 932, doi: 10.1038/s41550-019-0829-5

Galleti, S., Bellazzini, M., Federici, L., Buzzoni, A., & Fusi Pecci, F. 2007, A&A, 471, 127, doi: 10.1051/0004-6361:20077788

Galleti, S., Federici, L., Bellazzini, M., et al. 2014, VizieR Online Data Catalog, V/143

Genel, S., Fall, S. M., Hernquist, L., et al. 2015, ApJL, 804, L40, doi: 10.1088/2041-8205/804/2/L40

Gilbert, K. M., Font, A. S., Johnston, K. V., & Guhathakurta, P. 2009a, ApJ, 701, 776, doi: 10.1088/0004-637X/701/1/776

Gilbert, K. M., Kirby, E. N., Escala, I., et al. 2019, ApJ, 883, 128, doi: 10.3847/1538-4357/ab3807

Gilbert, K. M., Wojno, J., Kirby, E. N., et al. 2020, AJ, 160, 41, doi: 10.3847/1538-3881/ab9602

Gilbert, K. M., Fardal, M., Kalirai, J. S., et al. 2007, ApJ, 668, 245, doi: 10.1086/521094

Gilbert, K. M., Guhathakurta, P., Kollipara, P., et al. 2009b, ApJ, 705, 1275, doi: 10.1088/0004-637X/705/2/1275

Gilbert, K. M., Kalirai, J. S., Guhathakurta, P., et al. 2014, ApJ, 796, 76, doi: 10.1088/0004-637X/796/2/76

Guhathakurta, P., Rich, R. M., Reitzel, D. B., et al. 2006, AJ, 131, 2497, doi: 10.1086/499562

Guy, J., Bailey, S., Kremin, A., et al. 2022, arXiv e-prints, arXiv:2209.14482. https://arxiv.org/abs/2209.14482

Hammer, F., Yang, Y. B., Wang, J. L., et al. 2018, MNRAS, 475, 2754, doi: 10.1093/mnras/stx3343

Helmi, A., Babusiaux, C., Koppelman, H. H., et al. 2018, Nature, 563, 85, doi: 10.1038/s41586-018-0625-x

Hernquist, L. 1990, ApJ, 356, 359, doi: 10.1086/168845

Hinton, S. R. 2016, The Journal of Open Source Software, 1, 00045, doi: 10.21105/joss.00045

Huo, Z.-Y., Liu, X.-W., Yuan, H.-B., et al. 2010, Research in Astronomy and Astrophysics, 10, 612, doi: 10.1088/1674-4527/10/7/002

Huo, Z.-Y., Liu, X.-W., Xiang, M.-S., et al. 2013, AJ, 145, 159, doi: 10.1088/0004-6256/145/6/159

—. 2015, Research in Astronomy and Astrophysics, 15, 1438, doi: 10.1088/1674-4527/15/8/023

Husser, T. O., Wende-von Berg, S., Dreizler, S., et al. 2013, A&A, 553, A6, doi: 10.1051/0004-6361/201219058

Ibata, R., Chapman, S., Ferguson, A. M. N., et al. 2004, MNRAS, 351, 117, doi: 10.1111/j.1365-2966.2004.07759.x

Ibata, R., Irwin, M., Lewis, G., Ferguson, A. M. N., & Tanvir, N. 2001, Nature, 412, 49. https://arxiv.org/abs/astro-ph/0107090

Ibata, R., Martin, N. F., Irwin, M., et al. 2007, ApJ, 671, 1591, doi: 10.1086/522574

Ibata, R. A., Gilmore, G., & Irwin, M. J. 1994, Nature, 370, 194, doi: 10.1038/370194a0

Ibata, R. A., Lewis, G. F., McConnachie, A. W., et al. 2014, ApJ, 780, 128, doi: 10.1088/0004-637X/780/2/128

Kafle, P. R., Sharma, S., Lewis, G. F., Robotham, A. S. G., & Driver, S. P. 2018, MNRAS, 475, 4043, doi: 10.1093/mnras/sty082

Kalirai, J. S., Guhathakurta, P., Gilbert, K. M., et al. 2006a, ApJ, 641, 268, doi: 10.1086/498700

Kalirai, J. S., Gilbert, K. M., Guhathakurta, P., et al. 2006b, ApJ, 648, 389, doi: 10.1086/505697

Kirby, E. N., Gilbert, K. M., Escala, I., et al. 2020, AJ, 159, 46, doi: 10.3847/1538-3881/ab5f0f

Kirihara, T., Miki, Y., Mori, M., Kawaguchi, T., & Rich, R. M. 2017, MNRAS, 464, 3509, doi: 10.1093/mnras/stw2563

Koch, A., Danforth, C. W., Rich, R. M., Ibata, R., & Keeney, B. A. 2015, ApJ, 807, 153, doi: 10.1088/0004-637X/807/2/153

Koposov, S. 2022, segasai/sqlutilpy: sqlutilpy v0.19.0, 0.19.0, Zenodo, doi: 10.5281/zenodo.6867957

Koposov, S., & Bartunov, O. 2006, in Astronomical Society of the Pacific Conference Series, Vol. 351, Astronomical Data Analysis Software and Systems XV, ed. C. Gabriel, C. Arviset, D. Ponz, & S. Enrique, 735

Koposov, S., Speagle, J., Barbary, K., et al. 2022, joshspeagle/dynesty: v2.0.1, v2.0.1, Zenodo, doi: 10.5281/zenodo.7215695

Koposov, S. E. 2019, RVSpecFit: Radial velocity and stellar atmospheric parameter fitting, Astrophysics Source Code Library, record ascl:1907.013. http://ascl.net/1907.013

Koposov, S. E., Rix, H.-W., & Hogg, D. W. 2010, ApJ, 712, 260, doi: 10.1088/0004-637X/712/1/260

Koposov, S. E., Gilmore, G., Walker, M. G., et al. 2011, ApJ, 736, 146, doi: 10.1088/0004-637X/736/2/146

Kruijssen, J. M. D., Pfeffer, J. L., Chevance, M., et al. 2020, MNRAS, 498, 2472, doi: 10.1093/mnras/staa2452

Lan, T.-W., Tojeiro, R., Armengaud, E., et al. 2022, arXiv e-prints, arXiv:2208.08516. https://arxiv.org/abs/2208.08516

Lang, D. 2014, AJ, 147, 108, doi: 10.1088/0004-6256/147/5/108

Lewis, A. R., Dolphin, A. E., Dalcanton, J. J., et al. 2015, ApJ, 805, 183, doi: 10.1088/0004-637X/805/2/183

Mackey, A. D., Ferguson, A. M. N., Huxor, A. P., et al. 2019a, MNRAS, 484, 1756, doi: 10.1093/mnras/stz072

Mackey, D., Lewis, G. F., Brewer, B. J., et al. 2019b, Nature, 574, 69, doi: 10.1038/s41586-019-1597-1

Marigo, P., Bressan, A., Nanni, A., Girardi, L., & Pumo, M. L. 2013, MNRAS, 434, 488, doi: 10.1093/mnras/stt1034

Marocco, F., Eisenhardt, P. R. M., Fowler, J. W., et al. 2021, ApJS, 253, 8, doi: 10.3847/1538-4365/abd805

Martínez-Delgado, D., Gabany, R. J., Crawford, K., et al. 2010, AJ, 140, 962, doi: 10.1088/0004-6256/140/4/962

Massey, P., Neugent, K. F., & Levesque, E. M. 2019, AJ, 157, 227, doi: 10.3847/1538-3881/ab1aa1

Matheson, T., Stubens, C., Wolf, N., et al. 2021, AJ, 161, 107, doi: 10.3847/1538-3881/abd703

McConnachie, A. W. 2012, AJ, 144, 4, doi: 10.1088/0004-6256/144/1/4

McConnachie, A. W., Irwin, M. J., Ferguson, A. M. N., et al. 2005, MNRAS, 356, 979, doi: 10.1111/j.1365-2966.2004.08514.x

McConnachie, A. W., Irwin, M. J., Ibata, R. A., et al. 2009, Nature, 461, 66, doi: 10.1038/nature08327

McConnachie, A. W., Ibata, R., Martin, N., et al. 2018, ApJ, 868, 55, doi: 10.3847/1538-4357/aae8e7

Meisner, A. M., Lang, D., Schlafly, E. F., & Schlegel, D. J. 2019, PASP, 131, 124504, doi: 10.1088/1538-3873/ab3df4

Meisner, A. M., Lang, D., & Schlegel, D. J. 2017a, AJ, 154, 161, doi: 10.3847/1538-3881/aa894e

—. 2017b, AJ, 153, 38, doi: 10.3847/1538-3881/153/1/38

Merrett, H. R., Kuijken, K., Merrifield, M. R., et al. 2003, MNRAS, 346, L62, doi: 10.1111/j.1365-2966.2003.07367.x

Merrett, H. R., Merrifield, M. R., Douglas, N. G., et al. 2006, MNRAS, 369, 120, doi: 10.1111/j.1365-2966.2006.10268.x

Merrifield, M. R., & Kuijken, K. 1998, MNRAS, 297, 1292, doi: 10.1046/j.1365-8711.1998.01625.x

Milošević, S., Mićić, M., & Lewis, G. F. 2022, MNRAS, 511, 2868, doi: 10.1093/mnras/stac249

Mori, M., & Rich, R. M. 2008, ApJL, 674, L77, doi: 10.1086/529140

Myers, A. D., Moustakas, J., Bailey, S., et al. 2022, arXiv e-prints, arXiv:2208.08518. https://arxiv.org/abs/2208.08518

Naidu, R. P., Conroy, C., Bonaca, A., et al. 2020, ApJ, 901, 48, doi: 10.3847/1538-4357/abaef4

Navarro, J. F., Frenk, C. S., & White, S. D. M. 1997, ApJ, 490, 493, doi: 10.1086/304888

Pillepich, A., Springel, V., Nelson, D., et al. 2018, MNRAS, 473, 4077, doi: 10.1093/mnras/stx2656

Pillepich, A., Nelson, D., Springel, V., et al. 2019, MNRAS, 490, 3196, doi: 10.1093/mnras/stz2338

Plummer, H. C. 1911, MNRAS, 71, 460, doi: 10.1093/mnras/71.5.460

Pop, A.-R., Pillepich, A., Amorisco, N. C., & Hernquist, L. 2018, MNRAS, 480, 1715, doi: 10.1093/mnras/sty1932

Price-Whelan, A., Sipőcz, B., Lenz, D., et al. 2020, adrn/gala: v1.3, v1.3, Zenodo, doi: 10.5281/zenodo.4159870

Price-Whelan, A. M. 2017, The Journal of Open Source Software, 2, doi: 10.21105/joss.00388

Robitaille, T., Beaumont, C., Qian, P., Borkin, M., & Goodman, A. 2019, glueviz v0.15.2: multidimensional data exploration, 0.15.2, Zenodo, Zenodo, doi: 10.5281/zenodo.3385920

Ruiz-Lara, T., Gallart, C., Bernard, E. J., & Cassisi, S. 2020, Nature Astronomy, 4, 965, doi: 10.1038/s41550-020-1097-0

Sadoun, R., Mohayaee, R., & Colin, J. 2014, MNRAS, 442, 160, doi: 10.1093/mnras/stu850

Sanders, N. E., Caldwell, N., McDowell, J., & Harding, P. 2012, ApJ, 758, 133, doi: 10.1088/0004-637X/758/2/133

Sanderson, R. E., & Helmi, A. 2013, MNRAS, 435, 378, doi: 10.1093/mnras/stt1307

Schlafly, E. F., Meisner, A. M., & Green, G. M. 2019, ApJS, 240, 30, doi: 10.3847/1538-4365/aafbea

Schlafly, E. F., et al. 2022, in prep.

Schlaufman, K. C., Rockosi, C. M., Lee, Y. S., et al. 2012, ApJ, 749, 77, doi: 10.1088/0004-637X/749/1/77

Smith, R., Flynn, C., Candlish, G. N., Fellhauer, M., & Gibson, B. K. 2015, MNRAS, 448, 2934, doi: 10.1093/mnras/stv228

Speagle, J. S. 2020, MNRAS, 493, 3132, doi: 10.1093/mnras/staa278

Stern, D., Assef, R. J., Benford, D. J., et al. 2012, ApJ, 753, 30, doi: 10.1088/0004-637X/753/1/30

Tanaka, M., Chiba, M., Komiyama, Y., et al. 2010, ApJ, 708, 1168, doi: 10.1088/0004-637X/708/2/1168

Teuben, P. 1995, in Astronomical Society of the Pacific Conference Series, Vol. 77, Astronomical Data Analysis Software and Systems IV, ed. R. A. Shaw, H. E. Payne, & J. J. E. Hayes, 398

van der Marel, R. P., Fardal, M., Besla, G., et al. 2012, ApJ, 753, 8, doi: 10.1088/0004-637X/753/1/8

van der Marel, R. P., Fardal, M. A., Sohn, S. T., et al. 2019, ApJ, 872, 24, doi: 10.3847/1538-4357/ab001b

Walterbos, R. A. M., & Kennicutt, R. C., J. 1987, A&AS, 69, 311

Wang, S., Chen, B., & Ma, J. 2021, A&A, 645, A115, doi: 10.1051/0004-6361/202039531

Wenger, M., Ochsenbein, F., Egret, D., et al. 2000, A&AS, 143, 9, doi: 10.1051/aas:2000332

Xiang, M., & Rix, H.-W. 2022, Nature, 603, 599, doi: 10.1038/s41586-022-04496-5

Yuan, H.-B., Liu, X.-W., Huo, Z.-Y., et al. 2010, Research in Astronomy and Astrophysics, 10, 599, doi: 10.1088/1674-4527/10/7/001

APPENDIX

A. QUASARS AND GALAXIES BEHIND M31
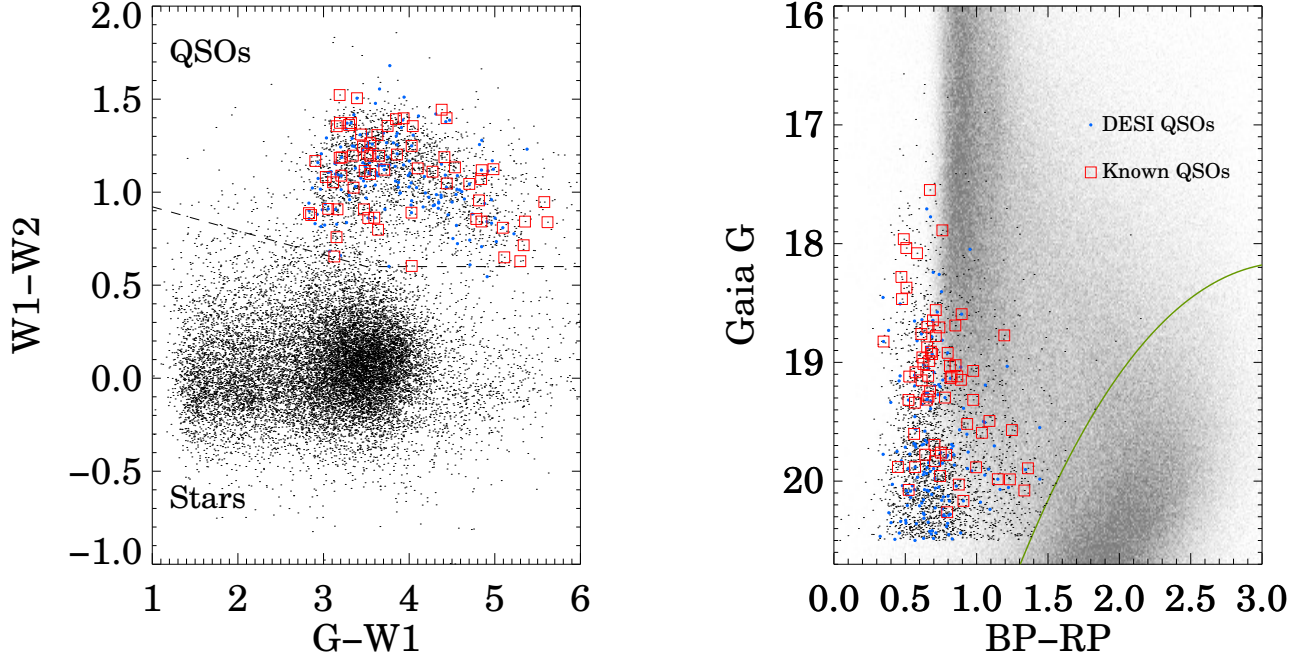
Figure 20. The selection of the DESI QSO targets. The left panel shows the criteria used (dashed line) to select QSO candidates. The known QSOs from Massey et al. (2019) and Huo et al. (2010, 2013, 2015) are shown as red squares and the QSOs confirmed by DESI spectroscopy are shown as filled blue dots. The right panel shows the *Gaia G* vs $B_p - R_p$ diagram as a greyscale for all *Gaia* stars within $5°$ of M31. The solid line shows the criterion used to exclude M31 sources.

QSO candidates were selected using a combination of the *Gaia* DR2 (Gaia Collaboration et al. 2016b, 2018) and the deep combined imaging data from the unWISE catalogs (Lang 2014; Meisner et al. 2017a,b, 2019; Schlafly et al. 2019) using the following criteria:

- $\pi - \sigma(\pi) \leq 0.1$

- $|\mu_\alpha - 2\sigma(\mu_\alpha)| \leq 0.1$ and $|\mu_\delta - 2\sigma(\mu_\delta)| \leq 0.1$

- ($G < 19$ and AEN$< 10^{0.5}$) or ($G \geq 19$ and AEN$< 10^{0.5+0.2(G-19)}$)

- $(W1 - W2) > 0.5$

- $(W1 - W2) > (1.0 - 0.125(G - W1))$

- $G \leq 26.46 - 5.991(BP - RP) + 1.313(BP - RP)^2 - 0.07856(BP - RP)^3$

where π, μ_α, μ_δ $\sigma(\pi)$, $\sigma(\mu_\alpha)$, $\sigma(\mu_\delta)$ are the parallax, proper motion, and associated uncertainties from the *Gaia* DR2 catalog; G, BP, RP are the *Gaia* DR2 mean photometric magnitudes; $W1$, $W2$ are the *WISE* channel 1 and 2 magnitudes from the unWISE catalogs; and AEN is the Astrometric Excess Noise parameter from the *Gaia* DR2 catalog.

The first three criteria are used to distinguish QSOs from Milky Way stars on the basis of parallaxes and proper motions consistent with zero in the *Gaia* DR2 catalog; these are generalized versions of the criteria used by van der

Marel et al. (2019) to select stars in M31 from the *Gaia* catalog. The AEN criterion is the same used by the DESI program to separate point sources from extended sources (i.e., galaxies) for *Gaia* DR2[6]. The $(W1-W2) > 0.5$ criterion is a more relaxed version of the *WISE* AGN selection discussed in Stern et al. (2012). The *Gaia - WISE* criteria were determined based on identifying the known spectroscopically confirmed QSOs (from Massey et al. 2019; Huo et al. 2010, 2013, 2015) in $G-W1-W2$ color-color space. Finally, the *Gaia* $G-BP-RP$ color criterion is an attempt to avoid stars from the M31 RGB in the QSO selection (see Figure 20).
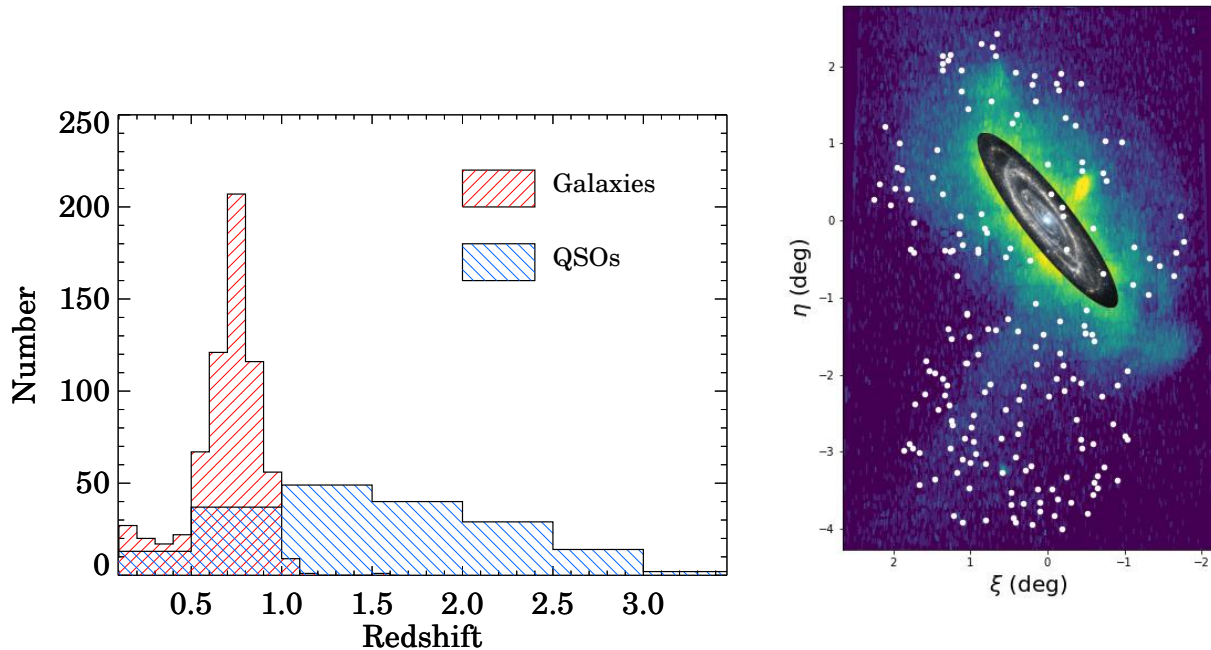
Figure 21. *Left:* Redshift distribution of the spectroscopically confirmed QSOs (blue hashed histogram) and galaxies (red hashed histogram). *Right:* The sky distribution of the spectroscopically-confirmed QSOs.

183 QSO candidates were targeted successfully (i.e., without fiber positioning errors) on the three DESI tiles discussed in this paper, 172 of which were spectroscopically confirmed as QSOs. The remaining 11 includes 8 stars and 3 galaxies. This represents a ≈94% success rate in the QSO selection criteria. In addition, 12 of our M31 stellar candidates turned out to be QSOs, and 683 were background galaxies. The spectroscopically confirmed QSOs and galaxies are presented in Tables 5 and 6 respectively. Figure 21 shows the redshift distribution of the extragalactic sources and the sky distribution of the QSOs.

These targets are useful probes of the interstellar and circumgalactic media of M31, and in particular provide a way of investigating any gas that may be associated with the various kinematic structures traced by the stellar debris (e.g., Koch et al. 2015).

B. N BODY SIMULATION DETAILS

For the simulations described in Section 4.2, we use a coordinate system that is aligned with the disk of M31, such that x_{M31} and y_{M31} are along the projected major and minor axes of the galaxy. The x_{M31} axis is oriented approximately towards the northeast in the plane of sky; the y_{M31} points out of the plane of the sky towards us but in a southeast

---

[6] See https://github.com/desihub/desitarget/blob/2.5.0/py/desitarget/gaiamatch.py#L207-L210

NOTE—Table 5 is published in its entirety in the machine-readable format. A portion is shown here for guidance regarding its form and content.

Table 5. QSOs Behind M31[a]

ID	RA (°)	Dec (°)	Redshift	G_{Gaia}	g_{PAndAS}	i_{PAndAS}	Alternate Name
1	10.0373918	40.1050291	2.196	19.88	19.68	19.46	Gaia DR3 369102106371697792
2	10.3592920	40.8907780	1.159	19.96	19.87	19.27	Gaia DR3 381161584267072896
3	10.0770974	39.8989696	0.284	19.76	19.90	19.54	Gaia DR3 368710061756016896
4	10.4851362	39.9701449	1.834	19.50	19.84	19.42	Gaia DR3 369044622529595520
5	10.0417886	39.7983967	0.675	20.06	NaN	NaN	Gaia DR3 368707720998989184
6	11.2855672	37.7439449	1.934	19.90	20.38	20.00	Gaia DR3 367495681227400192
7	10.8090715	37.6107886	2.489	19.61	19.98	19.86	Gaia DR3 367443454424848768
8	11.0832708	37.6063001	2.533	19.04	19.48	19.19	Gaia DR3 367490218028868352
9	11.2844517	37.5931928	1.287	20.28	20.74	20.23	Gaia DR3 367492142174203904
10	10.8512314	37.7872685	2.199	18.98	NaN	NaN	Gaia DR3 367543651717272064

[a] See Online Version for complete Table. The columns are: (1) a running index; (2,3) J2000 RA and Dec in decimal degrees; (4) Redshift; (5) *Gaia* *G*-band magnitude from Gaia DR3 (NaN if not available); (6,7) the PAndAS *g* and *i* magnitude (NaN if not available); (8) *Gaia* DR3 identifier.

NOTE—Table 6 is published in its entirety in the machine-readable format. A portion is shown here for guidance regarding its form and content.

Table 6. Galaxies Behind M31[a]

ID	RA (°)	Dec (°)	Redshift	g_{PAndAS}	i_{PAndAS}	Alternate Name
1	10.2211266	40.0121625	0.283	NaN	NaN	GC7461,SK090C ,SK090C
2	9.7017682	40.0505458	0.135	NaN	NaN	GC7429,SK058C ,SK058C
3	10.3558474	40.5148375	0.236	NaN	NaN	GC7191,SK078B ,SK078B
4	9.8651259	39.8292622	0.749	24.41	21.92	PANDAS 95102
5	10.6379474	40.0817180	0.212	NaN	NaN	GC7481,SK110C ,SK110C
6	10.8841125	37.6855167	0.560	23.81	21.52	PSUPP 20989
7	11.0291593	37.6711566	0.676	24.29	21.83	PANDAS 90320
8	11.0145968	37.7888733	0.765	24.67	22.08	PANDAS 90419
9	11.0623134	37.7701455	0.674	24.99	21.89	PANDAS 90457
10	11.1578093	37.8240122	0.801	24.54	22.03	PANDAS 90472

[a] See Online Version for complete Table. The columns are: (1) a running index; (2,3) J2000 RA and Dec in decimal degrees; (4) Redshift; (5,6) the PAndAS *g* and *i* magnitude (NaN if not available); (7) Alternate name, where available.

direction; and the z_{M31} axis is perpendicular to the M31 disk plane, pointing in a northwesterly direction and tilted out of the plane of the sky slightly towards us. The transformation between the M31 aligned coordinate system and a sky-oriented coordinate system in which x is pointing east, y is pointing north, and z is pointing away from us along the line of sight can be done with the matrix M (constructed assuming the position angle of the M31 line of nodes of

37° and and inclination of 77°):

$$M = \begin{pmatrix} 0.60181502 & -0.1796539 & -0.77816653 \\ 0.79863551 & 0.13537892 & 0.58639054 \\ 0. & -0.97437006 & 0.22495105 \end{pmatrix}$$

We start the simulation with the progenitor at $X_{M31} = (-5.44, 22.5, 35.25)$ kpc with velocity $V_{M31} = (19.66, -28.79, -64.68)$ km s^{-1} (in the coordinate system aligned with the disk), where the initial coordinates and velocities are taken from (Kirihara et al. 2017) and rotated using the matrix M.

We run the model for 977 Myr using the gyrfalcON integrator (Dehnen 2000, 2014) from the NEMO software package (Teuben 1995) using the following command:

```
mkplum - 300000 r_s=1 seed=1 mass=9000 | snapshift rshift=-5.44,22.5,35.25
vshift=19.66,-28.79,-64.68  in=- out=- | gyrfalcON - out.snp
accname=nfw,miyamoto,miyamoto,miyamoto,hernquist
accpars='0,7.63,215;10.68,.72,3.07e5;22.99,.72,-2e5;3.49,0.72,.329e5;0,1.39e5,.6'
tstop=1 kmax=18 eps=0.1 step=0.001
```

Some 1000 snapshots of the simulation made are provided on zenodo at https://doi.org/10.5281/zenodo.6977494. After running the simulations, we convert the outputs back into the space of observables, i.e., the coordinate system aligned with the sky by applying the inverse rotation matrix and assuming that M31 is at a distance of 750 kpc. We also compute the energies of each particle using the gala package (Price-Whelan 2017).

Figure 22 shows the resulting energy as a function of projected distance for the particles in the simulation associated with the structure which matches M31's Giant Stellar Stream. In the range between 1° and 4°, where we fit for the GSS in § 5.2, the total energy is approximately linear with radius.

Table 7. GSS radial velocity measurements

R	V_{GSR} - $V_{GSR,M31}$	σ_V
deg	km/s	km/s
1.00	-269.23	7.01
1.35	-225.67	4.20
1.70	-197.83	2.86
2.05	-169.69	2.78
2.40	-148.52	2.57
2.75	-132.03	2.49
3.10	-109.78	2.17
3.45	-92.01	2.29
3.80	-71.10	3.67

C. DESI M31 MEASUREMENT CATALOG

The measurements resulting from our analysis of the DESI spectroscopic observations are available as a FITS data table (DESI_M31_MEASUREMENT_CATALOG.fits). Table 8 contains a description of the columns in the FITS data table. The data table and other information are also available online **at https://doi.org/10.5281/zenodo.6977494.**

Table 8. Data Model for the M31 Data FITS File

Column Name	Data Type	Units	Column Description
TARGETID	LONG64	-	DESI target identification
RA	DOUBLE	deg	Right Ascention (J2000) in decimal degrees
DEC	DOUBLE	deg	Declination (J2000) in decimal degrees
DUPLICATE	LONG64	-	DESI TARGETID of the duplicate entry for this source if one exists; 0 otherwise
PRIMARY	INT	-	1 if this is the primary entry; 0 otherwise; only for duplicate entries
VRAD_BEST	DOUBLE	$\mathrm{km\,s^{-1}}$	"Best" heliocentric radial velocity in $\mathrm{km\,s^{-1}}$
VRAD_BEST_ERR	DOUBLE	$\mathrm{km\,s^{-1}}$	Uncertainty on "best" heliocentric radial velocity in $\mathrm{km\,s^{-1}}$
VRAD	DOUBLE	$\mathrm{km\,s^{-1}}$	Heliocentric radial velocity from DESI's RV Pipeline in $\mathrm{km\,s^{-1}}$
VRAD_ERR	DOUBLE	$\mathrm{km\,s^{-1}}$	Uncertainty on heliocentric radial velocity from DESI's RV Pipeline in $\mathrm{km\,s^{-1}}$
VRAD_SKEW	DOUBLE	$\mathrm{km\,s^{-1}}$	Skew on the heliocentric radial velocity from DESI's RV Pipeline in $\mathrm{km\,s^{-1}}$
VRAD_KURT	DOUBLE	$\mathrm{km\,s^{-1}}$	Kurtosis on the heliocentric radial velocity from DESI's RV Pipeline in $\mathrm{km\,s^{-1}}$
LOGG	DOUBLE	$\log(\mathrm{cm\,s^{-2}})$	Logarithm of the acceleration due to gravity from DESI's RV Pipeline in $\log(\mathrm{cm\,s^{-2}})$
TEFF	DOUBLE	K	Effective temperature from DESI's RV Pipeline in degrees Kelvin
FEH	DOUBLE	dex	[Fe/H] in units of solar metallicity
LOGG_ERR	DOUBLE	$\log(\mathrm{cm\,s^{-2}})$	Uncertainty on $\log(g)$
TEFF_ERR	DOUBLE	K	Uncertainty on Teff (K)
FEH_ERR	DOUBLE	dex	Uncertainty on [Fe/H] (dex)
CLASS	STRING	-	Selection class(es) for the target
DESIGNATION	STRING	-	Alternate designation of the target
SPECTYPE	STRING	-	Spectroscopic type: STAR, GALAXY or QSO; blank if unknown
GDR3_ID	LONG64	-	Gaia DR3 unique identification number
TILEID	STRING	-	DESI Tiles contributing to the spectrum
SN_B	FLOAT	-	Signal-to-noise ratio in the blue arm of the DESI spectrograph
SN_R	FLOAT	-	Signal-to-noise ratio in the red arm of the DESI spectrograph
SN_Z	FLOAT	-	Signal-to-noise ratio in the near-infrared arm of the DESI spectrograph
VRAD_REDROCK	DOUBLE	$\mathrm{km\,s^{-1}}$	Heliocentric radial velocity from the DESI Redrock pipeline in $\mathrm{km\,s^{-1}}$
VRAD_REDROCK_ERR	DOUBLE	$\mathrm{km\,s^{-1}}$	Uncertainty on the heliocentric radial velocity from the DESI Redrock pipeline in $\mathrm{km\,s^{-1}}$
REDROCK_ZWARN	LONG64	-	Warning flags for Redrock pipeline reductions (0=good)
RVS_WARN	INT	-	Warning flags for the RVS pipeline reductions (0=good)
VRAD_VI	DOUBLE	$\mathrm{km\,s^{-1}}$	Heliocentric radial velocity from the Visual Inspection in $\mathrm{km\,s^{-1}}$
VI_QUALITY	INT	-	Quality flag from the Visual Inspection (≥ 3 is good; ≤ 2 is bad; <0 is not inspected)
VI_SPECTYPE	STRING	-	Spectral type from the Visual Inspection
M31DIST	DOUBLE	deg	Projected radial distance from the center of M31[a] in degrees
GAIA_G	FLOAT	mag	Gaia G magnitude from the Gaia DR3 catalog
PANDAS_G	FLOAT	mag	PAndAS g-band magnitude from the PAndAS catalog
PANDAS_I	FLOAT	mag	PAndAS i-band magnitude from the PAndAS catalog
PRED_Z	FLOAT	mag	Predicted Legacy Surveys z-band magnitude
XI	DOUBLE	deg	Standard ξ coordinate in frame centered on M31[a] in degrees
ETA	DOUBLE	deg	Standard η coordinate in frame centered on M31[a] in degrees
THETA	DOUBLE	deg	Polar angle centered on M31 and measured clockwise from the west (as in Figures 6,7,11, and 12)

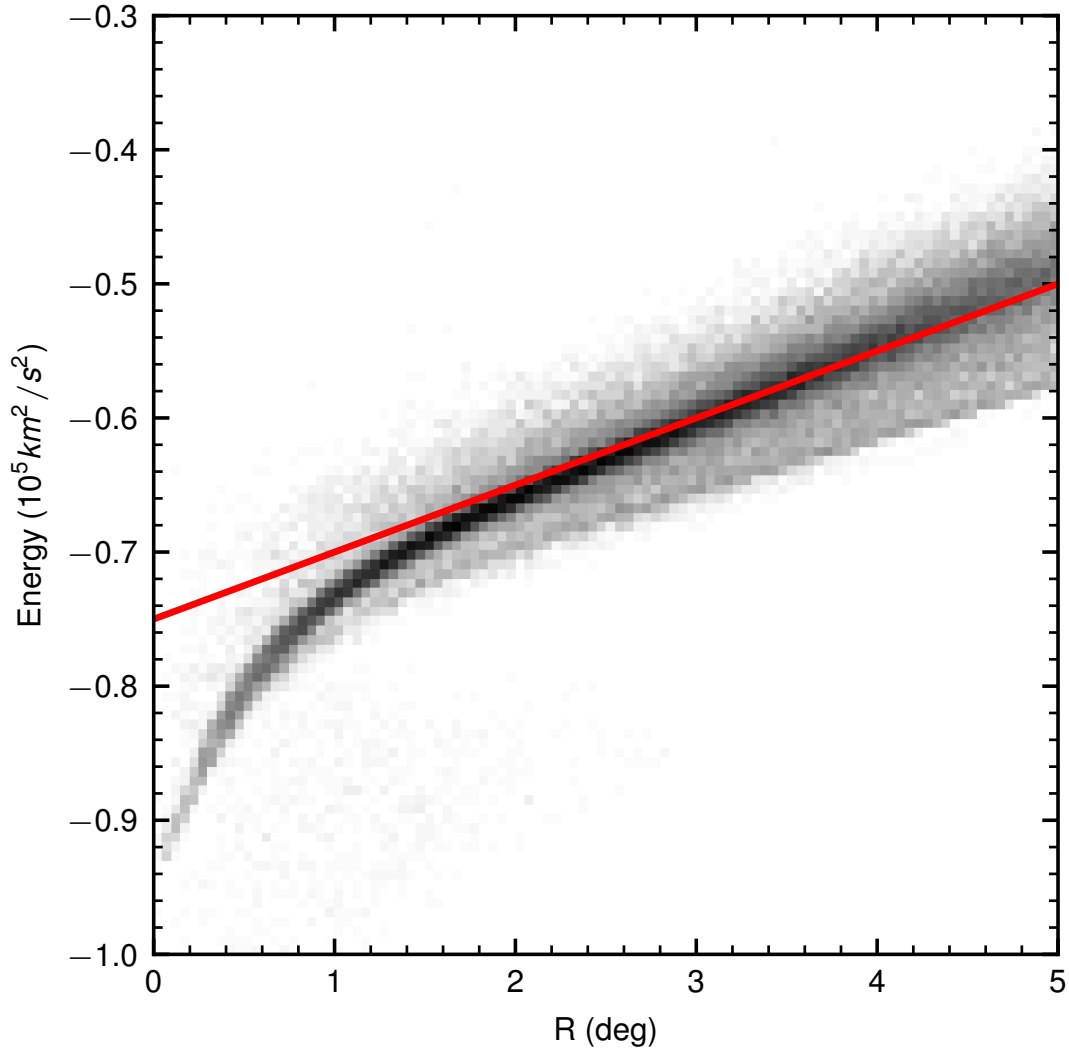The center of M31 is assumed to lie at RA=10.68470833° and DEC=41.26875°.

Figure 22. Total energy vs. projected galactocentric radius for the simulation discussed in Appendix B and § 4. The solid red line represents a slope of $\approx -380 \ (\mathrm{km\,s^{-1}})^2 \, \mathrm{kpc^{-1}}$. This shows that a linear relationship between energy and projected radius is reasonable approximation for projected radii $> 1.5°$.